# Development of non-destructive tritium measurement techniques and evaluation of migration and distribution of tritium in large fusion device

**Suneui Lee**

**University of Toyama**

Doctor of Philosophy

March 2023

# Abstract

Nuclear fusion is a promising carbon-free energy generation method. Deuterium (D) and tritium (T), the hydrogen isotopes, will be the fuels because DT reaction, $^{2}D + {}^{3}T \rightarrow {}^{4}He$ (3.5 MeV) + n (14.1 MeV), reaches higher reaction rate at lower temperature than other fusion reactions. Tritium is radioactive isotope of hydrogen and decays to helium-3 with emission of low energy β-rays: $^{3}T \rightarrow {}^{3}He + e^{-} + \bar{\nu}_e$ + 18.6 keV. The fuels are accumulated in the reactor walls by the plasma-wall interactions (PWIs) and the reactor components containing tritium are the potential radioactive hazard. In order to assess the safety of the fusion reactor, accurate analysis of fuel retention in the wall material is important. In this thesis, the new tritium detection methods were developed by combining the several tritium detection techniques to perform non-destructive, quantitative tritium retention analysis. The tritium distributions in the world largest fusion device in operation, Joint European Torus (JET), were evaluated using the developed methods. The important proposals to ITER and the future fusion reactors are given based on the post-mortem analyses of tritium distributions in JET plasma-facing tiles.

In Chapter 1, the current status of fusion energy development was overviewed. To demonstrate energy gain by fusion reactions, ITER is being constructed. The wall materials of JET in the UK were refurbished from full carbon wall to ITER-like wall (ILW): beryllium (Be) main chamber limiter, and tungsten (W) or W-coated carbon-fiber-composite (W-CFC) divertor plates to investigate possible PWIs in ITER. These plasma-facing tiles of JET had been exposed to DD plasma. Tritium was generated by DD fusion reactions [$^{2}D + {}^{2}D \rightarrow {}^{3}T$ (1.01 MeV) + $^{1}H$ (3.02 MeV)]. The research on deuterium retention were reviewed in this chapter. Also, the importance of investigation of tritium inventory which lead to developing of new non-destructive tritium detection technique is explained.

Chapter 2 describes the interactions of β-rays and X-rays with matters. In this study, 2-dimensional distributions of tritium β-rays intensity were measured using imaging plate (IP) technique. However, as the range of tritium β-rays is ~ 3 μm and ~ 0.3 μm in beryllium and tungsten, respectively, IP techniques gives information about tritium in the surface and sub-surface of the sample. On the other hand, X-rays generated by β-rays in matters have far longer escape depth than β-rays. Hence, the depth profiles of tritium were evaluated using β-ray induced X-ray spectrometry (BIXS) to obtain 3-dimensitonal view of tritium distributions. Physics behind

these measurement methods was explained.

Chapter 3 gives details about the plasma-facing tiles examined in this study. The Be tiles used in the main chamber had grooved structure for better durability against heat load from plasma. The W-CFC tiles were bulk tiles. On the other hand, W lamellae tiles were stack of pure W plates where gaps between the plates were found. The tritium retention on the plasma-facing surfaces and that inside the grooves and gaps were examined with IP and BIXS measurements. The principles and experimental setup for these measurements were also described. The X-ray spectra obtained from the BIXS were analyzed with Monte Carlo simulation by considering X-ray generation and attenuation in the samples. The chemical compositions on the tile surfaces and binding states of elements were evaluated with X-ray photoelectron spectroscopy (XPS) to investigate the mechanisms underlying tritium retention. The details of XPS measurements were also given in this chapter.

The tritium distributions in the main chamber Be limiters were described in Chapter 4. On the plasma-facing surfaces (PFSs) of the tiles, tritium was enriched at the erosion-dominant zone, though deuterium is reported to be concentrated at the deposition-dominant zone. The BIXS measurements showed tritium penetrated to the depth of ~ 6 μm. These results suggested implantation of 1.01 MeV tritons is the dominant tritium retention mechanism in the PFSs. In contrast, tritium retention in the grooves was dominated by co-deposition of tritium thermalized in plasma with deuterium, beryllium, oxygen, carbon and other impurities. Near the entrance of grooves (< 3 mm from the entrance), tritium retention was high and showed no systematic correlation with location in the chamber and chemical composition of deposition layers. Nevertheless, beyond 3 mm, tritium concentration increased with increasing content of carbon in the deposition layers.

Chapter 5 gives tritium retention in the divertor region. Co-deposition of thermalized tritium with beryllium, oxygen, carbon was dominant retention mechanism in the inner W-CFC divertor tiles. The deposition layers with high carbon content showed high tritium concentration. Tritium was implanted into outer W-CFC divertor tiles and implantation depth was ~ 1.5 μm. The PFSs of W lamellae tiles where strike points located showed low tritium content due to thermal desorption of tritium from the tile. On the other hand, the tritium-containing co-deposition layers composed of beryllium, oxygen, carbon were formed on the surfaces in the gaps.

Chapter 6 summarizes tritium behaviour in JET with ITER-like wall under deuterium

discharges. The migration of tritium was discussed in relation to the interaction between plasma and the Be limiters, transportation of beryllium sputtered from the Be limiter tiles and impurities pertain in the reactor. Key issues expected to dominate tritium inventory in ITER are also described. The approaches to reduce tritium co-deposition in the future fusion reactors are proposed based on post-mortem analyses performed in this study.

Finally, the main accomplishments of this study are summarized in Chapter 7.

# Acknowledgements

The content of this thesis is personal view of the author and does not necessarily reflect view of the individuals and organizations mentioned in the thesis. The analysis of specimens from JET was performed under the Broader Approach Agreement between Japan and the EU.

The author would like to deeply thank to supervisor, Professor Yuji Hatano, for his priceless support and advice during my study in Japan. His insight and knowledge always inspired me, a student who aimed to be a scientist. I also appreciate Professor Takayuki Abe for his dedication to providing me valuable suggestions about the Ph. D. thesis. I deeply thanks to Professor Masanori Hara about his advice to the Ph. D. thesis, especially guidance on performing simulation using the Monte Carlo method. I also appreciate Professor Kiyoshi Tsuge for his comments and feedbacks which were invaluable to improve the thesis.

I appreciate co-workers of the Broader Approach in Japan and the EU. I thanks to Professor Atsushi Ito about his time and efforts he spent to calculate simulation code.

Thanks to my family for their support. I would be impossible to continue my life in abroad without their encouragement.

# Contents

**Abstract** ..... I
**Acknowledgements** ..... V
**Contents** ..... VII

**Chapter 1. Introduction** ..... 1
1.1. Hydrogen isotopes ..... 1
1.2. Nuclear fusion reaction ..... 2
1.3. Limiter and divertor of tokamak ..... 5
1.4. ITER ..... 6
1.5. JET ITER-like wall project ..... 8
1.6. Deuterium retention in JET-ILW tokamak ..... 11
1.7. Necessity of development of tritium detection technique ..... 13
1.8. Purpose of this study ..... 14
References ..... 16

**Chapter 2. Interaction of radiations with matter** ..... 21
2.1. Interaction of β-rays with matter ..... 21
2.1.1. Coulomb interactions ..... 22
2.1.2. Emission of electromagnetic radiation ..... 22
2.1.3. Stopping power ..... 24
2.1.4. Range of charged particles ..... 24
2.2. Interaction of X-rays with matter ..... 25
2.2.1. Thomson scattering ..... 25
2.2.2. Photoelectric effect ..... 26
2.2.3. Compton scattering ..... 26
2.2.4. Pair production ..... 27
2.2.5. Photon attenuation coefficient ..... 27
References ..... 29

**Chapter 3. Experimental procedures** ..... 31
3.1. Tiles used in JET-ILW ..... 31
3.1.1. Beryllium limiter tiles ..... 31
3.1.2. Tungsten divertor tiles ..... 33

3.2. Analysis methods ..... 35
3.2.1. Imaging plate (IP) technique ..... 35
3.2.2. Beta-ray induced X-ray spectrometry (BIXS) ..... 39
3.2.3. Monte Carlo simulation and Geant4 ..... 41
3.2.4. X-ray photoelectron spectroscopy (XPS) ..... 43
References ..... 45

**Chapter 4. Tritium distribution in main chamber limiter** ..... 47
4.1. Plasma-facing surfaces ..... 47
4.2. Surfaces in the castellation grooves ..... 51
4.3. T inventory in the JET-ILW main chamber ..... 60
4.4. Summary ..... 64
References ..... 66

**Chapter 5. Tritium distribution in divertor region** ..... 69
5.1. W-coated carbon-fiber-composite (CFC) tiles ..... 69
5.2. Bulk tungsten lamellae tiles ..... 78
5.3. Summary ..... 83
References ..... 84

**Chapter 6. Tritium behaviour in fusion device with Be/W walls** ..... 87
6.1. Summary of tritium distributions in JET with ITER-like wall after deuterium discharges ..... 87
6.2. Methods to reduce tritium inventory ..... 89
References ..... 92

**Chapter 7. Conclusions** ..... 95

List of publications ..... 97

# Chapter 1. Introduction

## 1.1. Hydrogen isotopes

Hydrogen has three natural isotopes hydrogen (H), deuterium (D) and tritium (T). The atomic structures of the isotopes are described in Fig. 1.1. Deuterium is a stable isotope with one proton and one neutron. Tritium is a radioactive isotope with one proton and two neutrons and it decays to helium-3 by beta-decay.

Beta-decay is a phenomenon that an electron, a β-particle, is emitted with an antineutrino ($\bar{\nu}_e$) due to change of a neutron (n) into a proton (p) in nucleus,

$$\mathrm{n} \rightarrow \mathrm{p} + \mathrm{e}^- + \bar{\nu}_e . \tag{1.1}$$

Therefore, the beta-decay of T can be presented as following equation.

$$^3\mathrm{T} \rightarrow {}^3\mathrm{He} + \mathrm{e}^- + \bar{\nu}_e + Q. \tag{1.2}$$

The energy released from the beta-decay [1], the $Q$ value, is given by

$$Q = [M(A,Z) - Zm_e] - [M(A,Z+1) - (Z+1)m_e + m_e]$$

$$= M(A,Z) - M(A,Z+1) . \tag{1.3}$$

$M(A,Z)$ is atomic mass of an atom with atomic number $Z$ and mass number $A$. $m_e$ is mass of an electron.

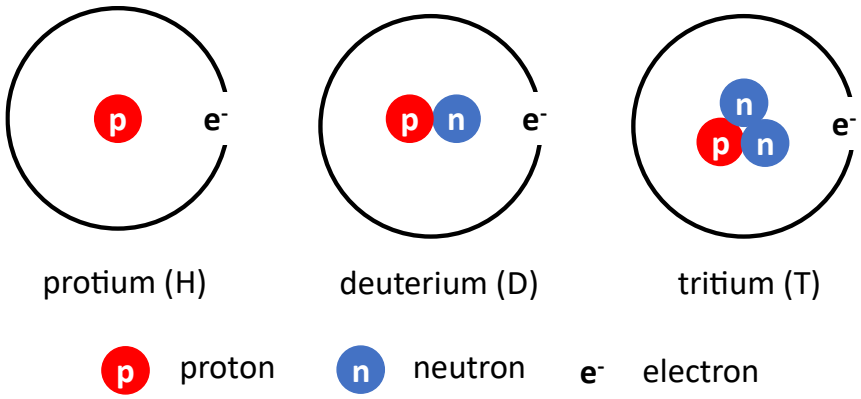


Fig. 1.1. Isotopes of hydrogen.

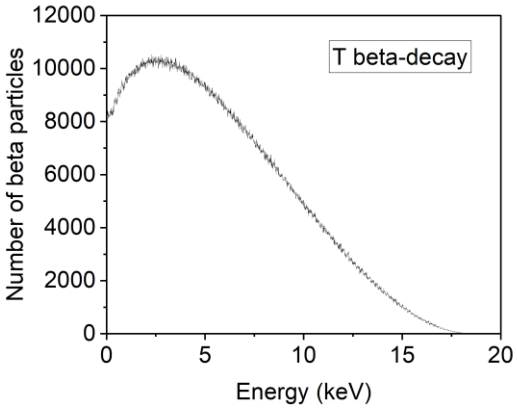


Fig. 1.2. Energy spectrum of beta particles from tritium.

The value of $Q$ is calculated to be 18.6 keV [2], and it is distributed to β-particle and antineutrino, as

$$E_\beta + E_v = Q. \tag{1.4}$$

Therefore, energy spectrum of β-particles is continuous. Fig. 1.2 is energy spectrum of beta particles from T calculated from Monte Carlo simulation tool Geant4. β-rays from T have the maximum energy of 18.6 keV and their mean energy is 5.7 keV.

The radioactivity of radioisotope decreases exponentially with time, following the equation given below;

$$N(t) = N_0 e^{-\lambda t}. \tag{1.5}$$

$N(t)$ is the radioactivity after time $t$ passed and $N_0$ is initial radioactivity. $\lambda$ is decay constant of the radionuclide. Half-life is necessary time that radioactivity becomes half of the initial stage. Therefore, the half-life $t_{1/2}$ can be obtained as

$$N(t_{1/2}) = N_0/2 = N_0 exp(-\lambda t_{1/2}) , \tag{1.6}$$

$$t_{1/2} = \ln 2/\lambda . \tag{1.7}$$

The half-life of T is 12.32 years [2].

## 1.2. Nuclear fusion reaction

Development of carbon-free new energy production method is essential due to increasing risk of global

warming. In order to reduce emission of greenhouse gases, 196 countries made an international treaty at Paris in 2015, The Paris Agreement [3]. Japan plans to reduce net greenhouse gas emission to zero in 2050 [4] and to generate 20 – 22 % of total electricity by nuclear energy in FY 2030 [5].

A fusion reactor generates energy with nuclear fusion reactions. Nuclear fusion reactions are the reactions that two or more light nucleus combined against Coulomb force and become a heavier nucleus. The mass difference between reactants and products is emitted as a kinetic energy of products according to Einstein's equation,

$$E=\Delta mc^2, \tag{1.8}$$

where $\Delta m$ is mass difference and $c$ is speed of light. There are several fusion reactions between light atoms and ions:

$$^2\mathrm{D} + {}^3\mathrm{T} \rightarrow {}^4\mathrm{He}\ (3.5\ \mathrm{MeV}) + \mathrm{n}\ (14.1\ \mathrm{MeV}), \tag{1.9}$$

$$^2\mathrm{D} + {}^2\mathrm{D} \rightarrow {}^3\mathrm{T}\ (1.01\ \mathrm{MeV}) + \mathrm{p}\ (3.02\ \mathrm{MeV}), \tag{1.10}$$

$$^2\mathrm{D} + {}^2\mathrm{D} \rightarrow {}^3\mathrm{He}\ (0.82\ \mathrm{MeV}) + \mathrm{n}\ (2.45\ \mathrm{MeV}), \text{ and} \tag{1.11}$$

$$^2\mathrm{D} + {}^3\mathrm{He} \rightarrow {}^4\mathrm{He}\ (3.5\ \mathrm{MeV}) + \mathrm{p}\ (14.7\ \mathrm{MeV}). \tag{1.12}$$

Fig. 1.3 from [6] shows reaction rates of light-ion fusion reactions. Fusion reaction between D and T has the highest reaction rate at temperature below 400 keV. Therefore, DT reaction becomes the promising fusion reaction for a future fusion reactor.

According to Lawson [7], the energy released per unit time and volume by fusion reaction $P_\mathrm{R}$ is given as

$$P_\mathrm{R} = n_1 n_2 \overline{v\sigma}(T) E_\mathrm{R}, \tag{1.13}$$

where $n_1$ and $n_2$ are the number densities of the nuclei, $\overline{v\sigma}(T)$ is the product of the relative velocities of the nuclei and the reaction cross section averaged over the Maxwellian velocity distribution at thermodynamic temperature $T$. $E_\mathrm{R}$ is the energy released by a single reaction.

The energy can be lost by radiation and the energy loss by radiation [8] is

$$P_B = 1.4 \times 10^{-34}\, n^2 T^{1/2}\ [\mathrm{W/cm^3}]. \tag{1.14}$$

In the equation, $n$ is the number density and $T$ is thermodynamic temperature.

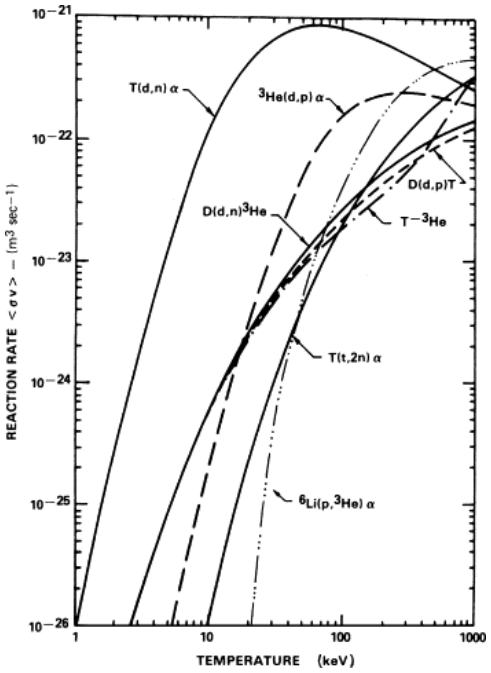


Fig. 1.3. Reaction rates of light-ion fusion reactions [6].

For the self-sustaining reactions, 'critical temperature' should be reached. The critical temperature is the temperature at which energy released by fusion reactions is equal to energy loss by radiation [7]. The critical temperature of DT reaction is $3\times10^8$ degrees K [7].

The high temperature has to be maintained for the reactions to be initiated. The confinement time $\tau_E$, the length of time that particles confined in the plasma, is defined as

$$\tau_E = W/P_{loss}. \tag{1.15}$$

In the equation, $W$ is energy per unit volume and $P_{loss}$ is rate of energy loss per unit volume. Under 50D-50T reaction condition, $W$ is given as

$$W = 3nT_{eV}, \tag{1.16}$$

where $n$ is particle density and $T_{eV}$ is temperature in eV.

The energy gain from fusion reactions should be larger than energy loss. Therefore,

$$fE_{ch} \geq P_{loss}, \tag{1.17}$$

where $f$ is reactions per volume per time and $E_{ch}$ is energy of charged products which is used to heat

up the plasma. In DT reactions, $^4$He with 3.5 MeV will be applied for plasma heating and $E_{ch}$ is 3.5 MeV. As a consequence,

$$n\tau_E \geq 1.5\times10^{20}\ \mathrm{s/m^3}. \tag{1.18}$$

This condition has to be qualified for DT reaction.

The amount of natural T is small and T breeding is necessary to produce T used as fuel. Neutrons from DT reactions will be used for T breeding via reaction with lithium,

$$^6\mathrm{Li} + \mathrm{n} \rightarrow {}^4\mathrm{He} + \mathrm{T}, \text{ and} \tag{1.19}$$

$$^7\mathrm{Li} + \mathrm{n} \rightarrow {}^4\mathrm{He} + \mathrm{T} + \mathrm{n}. \tag{1.20}$$

## 1.3. Limiter and divertor of tokamak

Fig. 1.4 is cross-section of the tokamak with (a) confined plasma and (b) divertor plasma. Limiters define the edge of plasma to avoid contact between plasma and the first wall. However, continuous operation is disrupted because impurities are accumulated to plasma. Therefore, concept of divertor was proposed and introduced to exhaust impurities inside the plasma.

By changing currents of poloidal field coil, the magnetic field is shifted to divertor configuration with open field lines as shown in Fig. 1.4 (b). The impurity particles escape from the core plasma and move along the magnetic field line and reach divertor region. The positions on the divertor tiles where

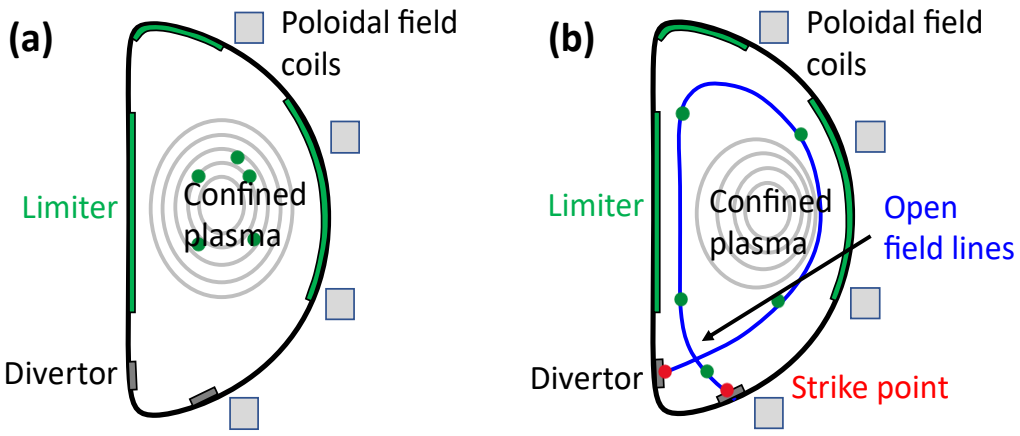


Fig. 1.4. Cross-sections of the tokamak with (a) confined plasma and (b) divertor plasma.

impurities are approached are strike points. Thus, high heat flux is localized to the strike points. The strike point sweeping is proposed to mitigate damage of the divertor tiles by expanding the distributed area of the strike points [9].

Carbon was used as the wall materials of tokamaks in the early stage of development of nuclear fusion reactor for several reasons. First, C has high thermal conductivity which is necessary for heat transport. Second, C sublimates at high temperature (3642 °C), and C walls are resistant to heat flux from the plasma. Also, low atomic number of C mitigates plasma radiation loss. However, the major drawback of the C as a material for fusion reactor walls was high hydrogen isotopes retention caused by formation of hydrogen isotopes-containing deposition layers. The high chemical sputtering yield of C and C-H bonding influenced the fuel inventory in the C first wall tokamak [10].

## 1.4. ITER

ITER is a magnetic confinement fusion reactor being constructed under international collaboration. The aim of ITER is to demonstrate energy gain by DT fusion reactions. ITER will start its DT operation in 2035 and duration of discharges is planned to be 400 s with fusion energy gain factor $Q_{fus} > 10$ and 3600 s with $Q_{fus} = 5$ [11]. Fig. 1.5 is its cross-section diagram and magnified image of vacuum vessel [12]. The T content in ITER with different wall conditions was estimated and Fig. 1.6 is the assessed T inventory [13]. T content in ITER with C-wall was above safety limit as thick fuel-containing

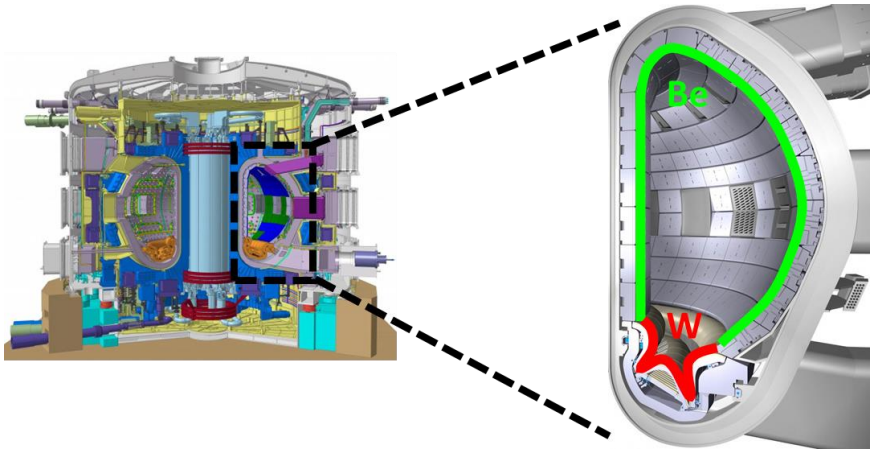


Fig. 1.5. Cross-section of ITER tokamak and magnified image of vacuum vessel [12]. The first wall of ITER tokamak is beryllium and the divertor tiles are tungsten.

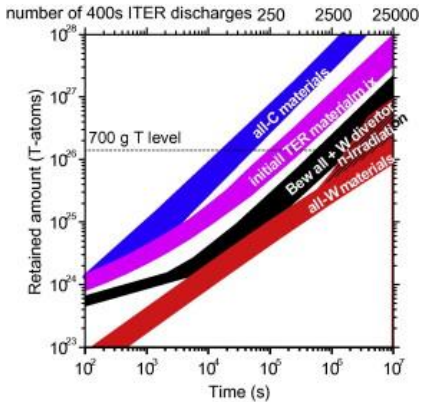


Fig. 1.6. Estimated T inventory in ITER with several different wall composition [13].

deposition layers were formed [13]. On the other hand, reactor with wall of mixture of beryllium (Be) and tungsten (W) was determined to retain fewer T than C-wall reactor by an order of magnitude. The magnified image in Fig. 1.5 shows the main chamber walls of ITER will be composed of Be, and W tiles will be installed in divertor region.

Be can reduce impurity in plasma as an oxygen getter and W is suitable for divertor tiles material because of its high melting point (3422 °C) and high thermal conductivity. Fig. 1.7 (a) is the ITER Be first wall panels [14] and (b) prototype of Be first wall [15]. Fig. 1.8 (a) is 3-dimensional view of the ITER divertor [16]. The ITER divertor requires 54 cassettes and each cassette includes inner vertical target, outer vertical target, dome and cassette body. Fig. 1.8 (b) is the prototype of inner vertical target

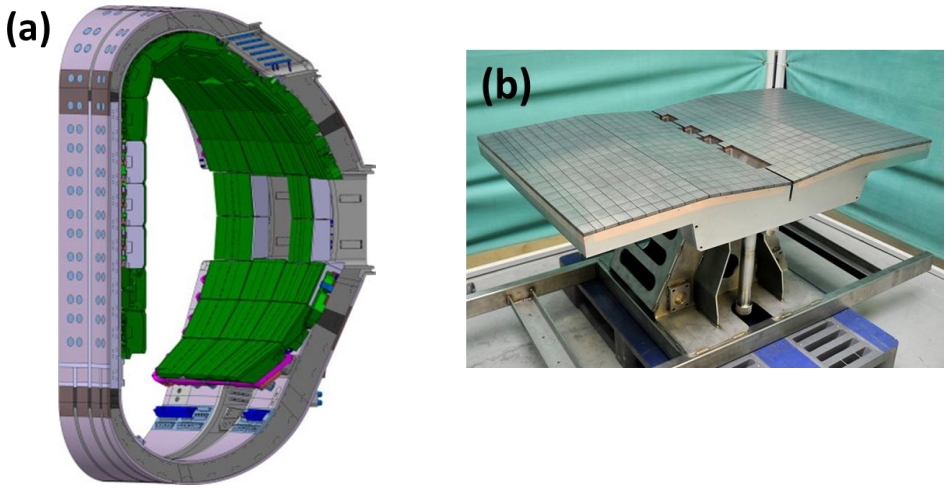


Fig. 1.7. (a) ITER first wall panels [14] and (b) prototype of Be first wall [15].

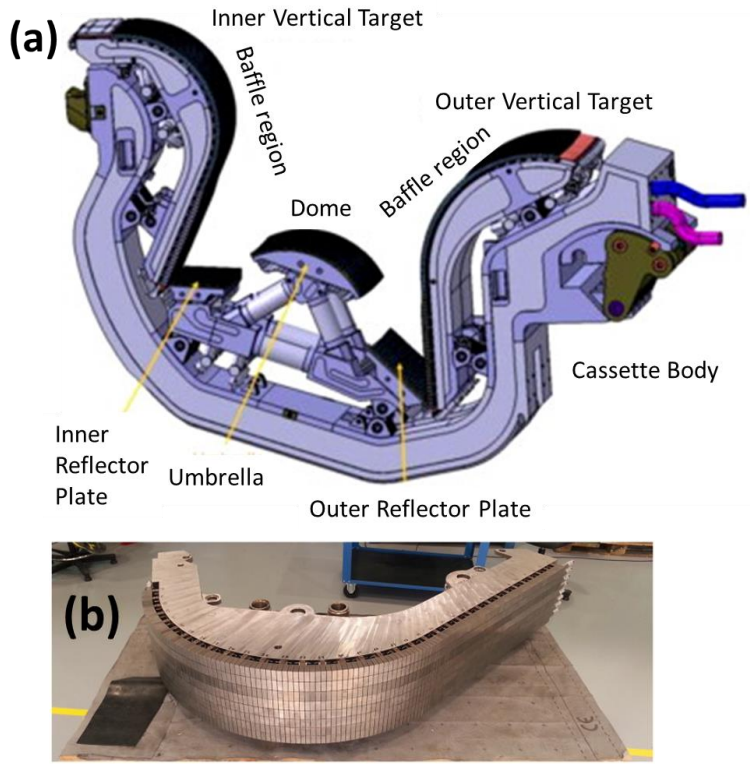


Fig. 1.8. (a) 3-dimensional view of the ITER divertor edited from [16] and (b) prototype of inner vertical target [17].

[17]. As shown in Figs. 1.7 and 1.8, the first wall tiles and divertor tiles are going to be castellated to improve durability against heat loads from plasma [18]. The total movable T inventory of ITER vacuum vessel should be less than 700 g [19] to obtain operation permission.

## 1.5. JET ITER-like wall project

To examine feasible plasma-wall interactions (PWIs) in future ITER, plasma-facing materials (PFMs) of Joint European Torus (JET) in UK replaced full carbon wall (JET-C) with ITER-like wall (JET-ILW) with Be main chamber limiters and W divertor tiles [20 – 22]. Fig. 1.9 shows the JET tokamak with JET-C (left) and JET-ILW (right) [20]. Be limiter tiles in the main chamber are bulk Be and W tiles in the divertor region are W coated carbon-fiber-composite (CFC) tiles or bulk W lamellae. The position of each type of tile is described in the right-hand side of Fig. 1.9.

After the exchange of the PFMs, JET-ILW campaign was conducted for three times in 2011-2016 with D fuelling. The first campaign was ILW1 in 2011-2012, second campaign ILW2 was in 2013-2014 and the third campaign ILW3 was carried out in 2015-2016. The operation parameters in these

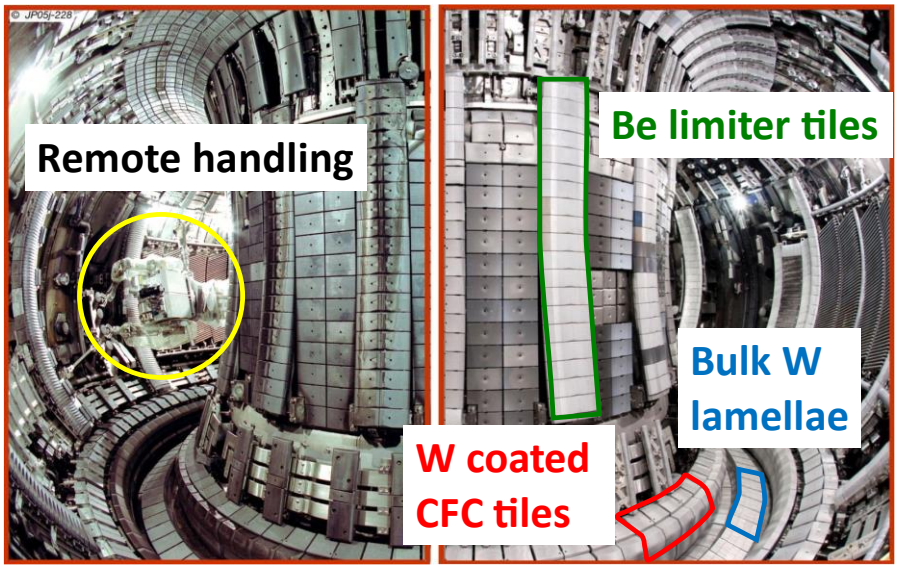


Fig. 1.9. JET tokamak with full carbon wall (left) to ITER-like wall with Be limiter tiles and W coated carbon-fiber-composite (CFC) divertor tiles and bulk W divertor tiles. The position of Be limiter tiles in the main chamber are indicated in green color. W-CFC tiles and bulk W lamellae tiles in the divertor region are shown in red and blue colors, respectively. Edited from [20].

ILW campaigns are summarized in Table. 1.1. As the table shows, ILW3 was performed for the longest time with highest input energy. The largest amount of T was produced in ILW3. Duration of each discharge was shorter than 20 s and it is shorter than planned duration of ITER.

Fig. 1.10 is a schematic image of JET-ILW tokamak cross-section [23] and magnified image of divertor region [24]. The location of Be limiter tiles is indicated in green. There are three types of Be limiter tiles according to their position: inner wall guard limiter (IWGL), outer poloidal limiter (OPL) and upper dump plate (DP). The divertor tiles are shown in red. The big numbers in the magnified image of divertor region are tile numbers. The small numbers are S-coordinate which indicates the distance from Tile 0 in mm scale. Tile 0, 1, 3, 4, 6, 7, 8 are W-coated carbon-fiber-composite tiles and Tile 5 is bulk W lamellae tile. Tile 0, 1, 3, 4 are inner divertors and 6, 7, 8 are outer divertors.

The PWI studies determined the erosion of first wall material by the plasma, sputtering of Be limiter tile. Part of Be sputtered from the limiter tiles re-deposited on the limiter tiles. The other parts are confined in plasma, transported to divertor region and deposited on the divertor tiles. During this process, D introduced as fuels co-deposited with sputtered materials and impurities. D were deposited not only on the PFS [25 – 27], but also on the surfaces inside the gaps [26, 28] of the divertors.

In the limiter plasma configurations, impact energy of D ions to limiter tile is in the range of 35 – 200 eV [20]. Brezinsek et al. [20] determined the physical sputtering yield of Be and C by D as a

Table 1.1. Operation parameters of ILW campaigns.

| Parameter | ILW1 (2011-12) | ILW2 (2013-14) | ILW3 (2015-16) | Total |
|---|---|---|---|---|
| **Total number of shots*** | 3668 | 4149 | 4420 | 12237 |
| **Total plasma time (h)** | 20.38 | 19.8 | 23.33 | 63.51 |
| **Limiter plasma (h)** | 7.76 | 6.04 | 4.86 | 18.66 |
| **Divertor plasma (h)** | 12.62 | 13.76 | 18.47 | 44.85 |
| **Input energy (GJ)** | 145 | 201 | 245 | 496 |
| **Fuel** | $D_2$ | Mostly $D_2$, Last 300 shots in $H_2$ | $D_2$ | |
| **Produced T (GBq)** | 14 | 35 | 38 | |
| * Total number including events of non-sustained breakdown. | | | | |

function of D ion energy. In D ion impact energy range from 35 to 200 eV, physical sputtering yield of Be is higher than C. However, due to low threshold energy of C chemical sputtering, chemical sputtering of C by low energy particles is possible. As a consequence, the C first wall of JET-C sputtered by plasma, and eroded C was redistributed on shadowed region of divertor tiles.

The continuous erosion of C generated a large amount of volatile hydrocarbon molecules containing hydrogen isotopes [29]. Therefore, long term fuel retention in JET-C was higher than that of JET-ILW by an order of magnitude [30]. In previous MkII-SRP operations in 2001–2004 with C wall, the amount of retained D was 4 % of injected D [31]. On the other hand, 0.19 % of introduced D was retained during ILW3 campaign [32]. The change of PFM significantly reduced fuel retention inside the tokamak.

Fig. 1.11 is the photo of JET-ILW (a) Be limiter tile IWGL and (b) W-CFC divertor Tile 1. The Be limiter tiles of JET-ILW were castellated as the design of ITER Be first wall. The width of castellation grooves is ~ 0.4 mm [33]. There are the surfaces inside the castellation grooves. In JET-ILW Be limiter

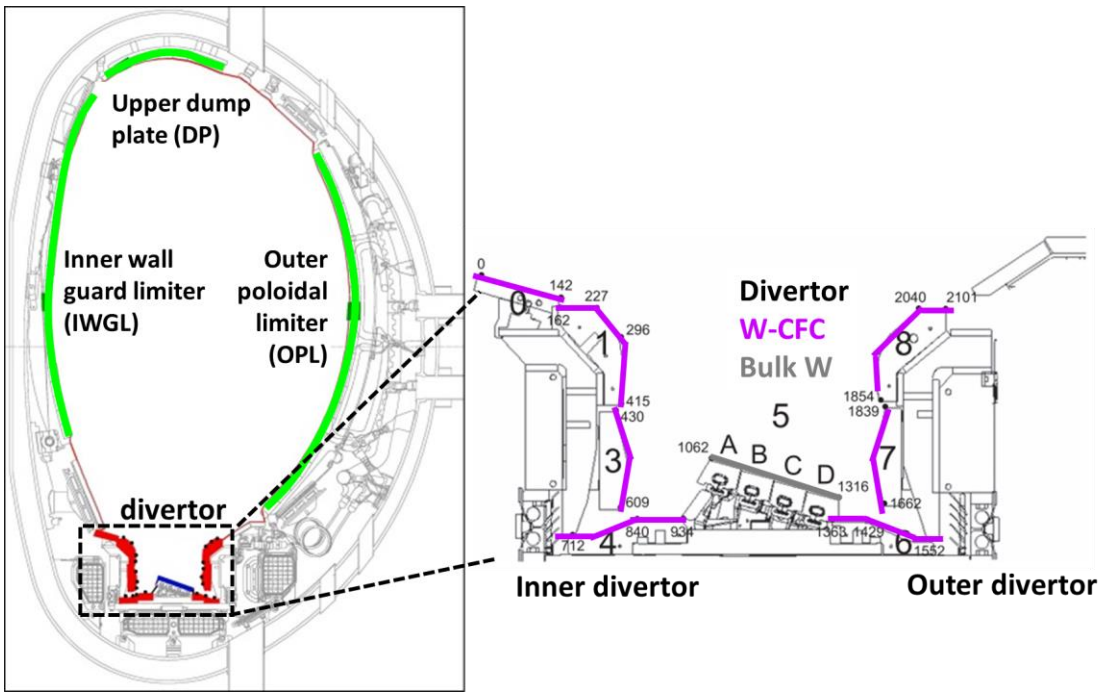


Fig. 1.10. Cross-section of JET-ILW tokamak [23] and magnified image of divertor region [24]. In the left image, the Be limiter tiles and W divertor tiles are indicated in green color and red color, respectively. There are three types of Be limiter tiles according to their positions: inner wall guard limiter (IWGL), outer poloidal limiter (OPL) and upper dump plate (DP). The big numbers in the magnified image of divertor region is tile number. The small numbers are S-coordinates which indicates the distance from the Tile 0 in mm scale.

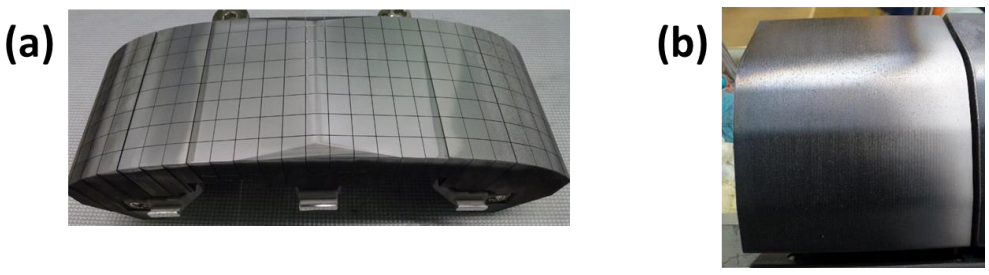


Fig. 1.11. Photo of JET-ILW (a) Be limiter tile IWGL and (b) W-CFC divertor Tile 1.

tiles, the area of PFS and the surfaces inside the castellation grooves is 24.5 $m^2$ and 88 $m^2$, respectively [33]. On the other hand, JET-ILW W-CFC divertor tiles were bulk without any gaps in a single tile.

## 1.6. Deuterium retention in JET-ILW tokamak

An accurate evaluation of T retention in plasma-facing components (PFCs) is important to assess

potential hazard of radioactive T. Therefore, distribution and migrations of D during ILW campaigns were investigated under assumption that D behaviors resemble T behaviors inside the tokamak. The D retentions and distributions were reported by several researchers [23, 24, 33 – 52].

Studies about D behaviors inside the JET-ILW determined that dominant retention mechanism of D is co-deposition with eroded materials. Materials eroded from the limiter tiles re-deposited at the edges of the tiles or transported to divertor region and deposited on the inner divertor tiles. 60 % of retained D was detected in the divertor regions and the divertor tiles contained larger amount of D than the limiter tiles [52].

In Be limiter tiles, D was enriched in the deposition layer formed on PFSs [34 – 36]. D was also deposited on the surfaces inside the castellation gaps [33]. D retained in the surfaces inside castellation grooves of the Be limiter tiles accounted for 50 % of total D in the main chamber [32, 33].

After implantation of 1 keV D ions to clean and oxidized single crystal Be, D was started to release at 440 K [53]. The desorption rate of D retained in Be tiles used in JET-ILW had peak in the range of 800 – 900 K and surface contamination by deposit increased the D desorption temperature [37]. In addition, more than 90 % of D retained in the specimens from the center of IWGL PFS and OPL PFS remained even after 15 h of bake-out at 240 °C [39]. The maximum release rate of D was observed in the range of 450 – 600 °C [37]. The center of IWGL and OPL was under severe PWIs which induce erosion of the tile surface. Therefore, D accumulated at the erosion zone was trapped in plasma-induced defects and cannot be released by thermal heating [39].

On the other hand, particles eroded from the tile center were re-deposited in the both side edges of IWGL and OPL [35, 36, 40, 52]. The specimen from the edge of IWGL, deposition dominant zone showed decrease in D retention after baking [39]. The direct interaction with plasma did not occur at the edges of tile because of its recessed position and D was retained in traps with low activation energy for detrapping [39]. DP tiles contained similar amount of D to IWGL and OPL [36]. However, the PFS of DP tiles were partly melted due to high tile temperature induced by disruptions [41].

The retention of D in the divertor tiles were also investigated [24, 34, 39, 42 – 48] and it showed similar tendency: D distribution on the tile surfaces agreed to the distribution of deposition layer [24, 44 – 46]. Thick deposition layers were formed on the PFSs of inner divertor tiles and D concentration was high [24, 44 – 46]. Small amount of D was found on outer divertor tiles where tile PFSs were eroded [24, 44 – 46]. Heinola et al. [39] reported that the time necessary to release retained D from divertor tile increased as the thickness of deposition increased, i. e., after annealing of 15 h at 350 °C,

only 10 % of accumulated D was removed from the tile with 40 μm deposition layer while 70 % of D was desorbed from the tile where 3 μm-thick deposition was formed. According to thermal desorption spectroscopy (TDS), the releasing rate of D from the JET-ILW divertor tile specimens reached maximum in temperature higher than 500 °C, in general [42, 43, 48]. The concentration of D was low in the deposition with small C content [24, 48]. Therefore, accumulation rate of D decreased with the exchange of JET-C to JET-ILW [49, 50] and C impurities gradually decreased from campaign to campaign in JET-ILW [44].

### 1.7. Necessity of development of tritium detection technique

There are several techniques which were utilized to measure T retention in plasma-facing tiles, as summarized in Table 1.2. Each method has its own strength and drawbacks.

The quantitative analysis of radioactivity of T is possible with combustion method and acid

Table 1.2. Summary of T detection methods.

| | Total inventory | Non-destructive | Surface distribution | Depth profiling | T detection limit |
|---|---|---|---|---|---|
| Pyrolysis, Full combustion method | ○ | × | × | × | ~ Bq |
| Acid dissolution method | ○ | × | × | ○ | ~ Bq |
| Thermal desorption spectroscopy (TDS) | ○ | × | × | × | ~ Bq |
| PIN diode β-ray counting | × | ○ | × | × | ~ kBq/cm$^2$ |
| β-ray sensitive imaging plate | × | ○ | ○ | × | ~ kBq/cm$^2$ |
| β-ray induced X-ray spectrometry | × | ○ | × | ○ | ~ kBq/cm$^2$ |
| X-ray sensitive imaging plate | × | ○ | ○ | △ | ~ 10 kBq/ cm$^2$ |
| Calorimeter | ○ | ○ | × | × | ~ GBq |

dissolution method. The combustion method was applied to examine T depth profiles in carbon-fiber-composite divertor tile from JET-C [54, 55]. Also, T depth profiles of JET-ILW Be limiter tiles [56 – 59] were evaluated with acid dissolution method.

To understand the mechanisms underlying non-uniform T distributions, the correlation of T distributions with chemical composition and microstructures must be clarified. Hence, the analyses of the specimen with multiple techniques are necessary. A non-destructive T detection technique allows to get multiple types of information by combining with other analysis techniques. However, the pyrolysis and the dissolution method are destructive and additional analyses are impossible. Calorimeter is non-destructive method but the radioactivity of the T containing materials should be in order of GBq. In addition, information of T distribution cannot be obtained. In order to overcome those drawbacks, development of new non-destructive T detection method is necessary.

T distribution in MK II SRP divertor tiles used in JET-C during 2001-2004 was studied by imaging plate (IP) technique [27]. IP detects β-rays emitted from T and 2-dimensional distribution of T can be determined by the IP technique. The size of one pixel is 25 μm and it is sufficiently high to obtain 2D images of T distributions on PFSs. The exposure of IP sheets to β-rays can be simply performed by contacting IP sheet to the tritiated specimen surface. In addition, no electronic device is necessary during exposure process. IP can give information about T accumulated within the range of T β-rays. The IP results indicated that D distribution in MK II divertor tile was inhomogeneous even in a single tile [27].

Beta-ray induced X-ray spectrometry (BIXS) [60, 61] detects X-rays induced by reactions between T β-rays and materials. It is non-destructive method, but distribution of T cannot be observed. On the other hand, the X-ray spectra of T-containing samples acquired with BIXS demonstrated the change in shape of the spectra due to diffusion of T from sub-surface to the bulk [61]. It indicated the possibility of T depth profiling with BIXS technique.

### 1.8. Purpose of this study

An accurate determination of T inventory inside the JET-ILW tokamak is important (i) to understand T retention mechanisms in a fusion machine with Be and W walls, (ii) to estimate T inventory in ITER for licensing for operation, and (iii) to minimize T retention for efficient use of T as fuel in future fusion devices. Instead of T, retention of D was analyzed under assumption that behaviors of T are

similar to those of D. However, there are some advantages in T measurements. First, passive measurements with high sensitivity are possible by β-ray detection. Second, distribution of 1.01 MeV T generated by DD reactions and implanted to walls can provide information on confinement of high energy ions in plasma.

In this study, non-destructive T measurement techniques were developed by applying imaging plate (IP) technique, β-ray induced X-ray spectrometry (BIXS) and Monte Carlo simulation. T distributions in the limiter tiles and the divertor tiles used in JET-ILW were evaluated by the developed technique. The tiles exposed to the plasma during ILW1, ILW3 or all three campaigns (ILW1-3) were analyzed to investigate the influence of tokamak operation parameters to T behaviors. T retention of each tile was examined and compared to determine the difference of fuel accumulation mechanism according to the tile positions in the vacuum vessel. The retention mechanism was investigated with X-ray photoelectron spectroscopy (XPS) by determining chemical composition of deposition layer. Also, elucidated retention mechanism of T was compared to that of D. The suggestions to ITER and future fusion reactors to reduce fuel inventory are proposed according to observations from this study.

References


[1] Hooshang Nikjoo, Shuzo Uehara, Dimitris Emfietzoglou, Interaction of radiation with matter, Taylor and Francis (2012) 64

[2] F. T. Porter, Beta decay energy of tritium, Phys. Rev. 115 (1959) 450-453, https://doi.org/10.1103/PhysRev.115.450

[3] United Nations Convention on Climate Change (2015) Adoption of the Paris Agreement, 21st Conference of the Parties, Paris.

[4] https://www.meti.go.jp/english/policy/energy_environment/global_warming/roadmap/

[5] https://unfccc.int/sites/default/files/resource/Japan_MA2019_presentation.pdf.

[6] M.R. Gordinier et al., Encyclopedia of Physical Science and Technology (Third Edition), 2003

[7] J. D. Lawson, Some Criteria for a Power Producing Thermonuclear Reactor, Proc. Phys. Soc. B 70 (1957) 6, https://doi.org/10.1088/0370-1301/70/1/303

[8] L. Spitzer, The Physics of Fully Ionized Gases (New York : Interscience Publishers), 1956

[9] S. A. Silburn et al., Mitigation of divertor heat loads by strike point sweeping in high power JET discharges, Phys. Scr. T170 (2017) 014040, https://doi.org/10.1088/1402-4896/aa8db1

[10] G. F. Matthews, Material migration in divertor tokamaks, J. Nucl. Mater. 337-339 (2005) 1-9, https://doi.org/10.1016/j.jnucmat.2004.10.075

[11] D. Wunderlich et al., NNBI for ITER: status of long pulses in deuterium at the test facilities BATMAN Upgrade and ELISE, Nucl. Fusion 61 (2021) 096023, https://doi.org/10.1088/1741-4326/ac1758

[12] https://www.iter.org

[13] J. Roth et al., Recent analysis of key plasma wall interactions issues for ITER, J. Nucl. Mater 15 (2019) 1-9, https://doi.org/10.1016/j.jnucmat.2009.01.037

[14] R. Mitteau et al., The design of the ITER first wall panels, Fusion Eng. Des., 88 (2013) 6-8, https://doi.org/10.1016/j.fusengdes.2013.05.030

[15] https://www.iter.org/newsline/-/3568

[16] M. Merola et al., Overview and status of ITER internal components, Fusion Eng. Des. 89 (2014) 890-895, https://doi.org/10.1016/j.fusengdes.2014.01.055

[17] P. Gavila et al., Status of the ITER Divertor IVT procurement, Fusion Eng. Des. 160 (2020) 111973, https://doi.org/10.1016/j.fusengdes.2020.111973

[18] A. Litnovsky et al., Optimization of tungsten castellated structures for the ITER divertor, J. Nucl. Mater 463 (2015) 174-179, https://doi.org/10.1016/j.jnucmat.2014.11.009

[19] International Atomic Energy Agency, Summary of the ITER Final Design Report, ITER EDA Documentation Series No. 22, IAEA, Vienna (2001).

[20] S. Brezinsek, JET-EFDA contributors, Plasma-surface interaction in the Be/W environment: Conclusions drawn from the JET-ILW for ITER. J. Nucl. Mater. 463 (2015) 11-21, https://doi.org/10.1016/j.jnucmat.2014.12.007

[21] V. Philipps et al., Overview of the JET ITER-like Wall Project, Fusion Eng. Des. 85 (2010) 1581-1586, https://doi.org/10.1016/j.fusengdes.2010.04.048

[22] G. F. Matthews et al., JET ITER-like wall - overview and experimental programme, Phys. Scr. T145 (2011) 014001, https://doi.org/10.1088/0031-8949/2011/T145/014001

[23] A. Widdowson et al., Material migration patterns and overview of first surface analysis of the JET ITER-like wall, Phys. Scr. T159 (2014) 014010, https://doi.org/10.1088/0031-8949/2014/T159/014010

[24] M. Mayer et al., Erosion and deposition in the JET divertor during the second ITER-like wall campaign, Phys. Scr. T170 (2017) 014058, https://doi.org/10.1088/1402-4896/aa8ff9

[25] J. P. Coad et al., Erosion/deposition issues at JET, J. Nucl. Mater. 290-293 (2001) 224-230, https://doi.org/10.1016/S0022-3115(00)00479-7

[26] J. P. Coad et al., Material migration and fuel retention studies during the JET carbon divertor campaigns, Fus. Eng. Des. 138 (2019) 78-108, https://doi.org/10.1016/j.fusengdes.2018.10.002

[27] T. Tanabe et al., Tritium distribution measurement of JET Mk II SRP divertor tiles, J. Nucl. Mater. 363-365 (2007) 960-965, https://doi.org/10.1016/j.jnucmat.2007.01.191

[28] M. J. Rubel et al., Overview of co-deposition and fuel inventory in castellated divertor structures at JET, J. Nucl. Mater 367-370 (2007) 1432-1437, https://doi.org/10.1016/j.jnucmat.2007.04.007

[29] T. Loarer, Fuel retention in tokamaks, J. Nucl. Mater. 390-391 (2009) 20-28, https://doi.org/10.1016/j.jnucmat.2009.01.039

[30] T. Loarer et al., Comparison of long term fuel retention in JET between carbon and the ITER-like wall, J. Nucl. Mater. 438 (2013) S108-S133, https://doi.org/10.1016/j.jnucmat.2013.01.017

[31] J. Likonen et al., Post-mortem measurements of fuel retention at JET with MKII-SRP divertor, J. Nucl. Mater. 390-391 (2009) 631-634, https://doi.org/10.1016/j.jnucmat.2009.01.176

[32] A. Widdowson et al., Evaluation of tritium retention in plasma facing components during JET tritium operations, Phys. Scr. 96 (2021) 124075, https://doi.org/10.1088/1402-4896/ac3b30

[33] M. Rubel et al., Fuel inventory and deposition in castellated structures in JET-ILW, Nucl. Fusion 57 (2017) 066027, https://doi.org/10.1088/1741-4326/aa6864

[34] K. Heinola et al., Long-term fuel retention in JET ITER-like wall, Phys. Scr. T167 (2016) 014075, https://doi.org/10.1088/0031-8949/T167/1/014075

[35] K. Heinola et al., Fuel retention in JET ITER-Like Wall from post-mortem analysis, J. Nucl. Mater 463 (2015) 961-965, https://doi.org/10.1016/j.jnucmat.2014.12.098

[36] A. Widdowson et al., Fuel inventory and material migration of JET main chamber plasma facing components compared over three operational periods, Phys. Scr. T171 (2020) 014051, https://doi.org/10.1088/1402-4896/ab5350

[37] A. Baron-Wiechec et al., Thermal desorption spectrometry of beryllium plasma facing tiles exposed in the JET tokamak, Fusion Eng. Des., 133 (2018) 135-141, https://doi.org/10.1016/j.fusengdes.2018.05.075

[38] A. Widdowson et al., Overview of fuel inventory in JET with the ITER-like wall, Nucl. Fusion 57 (2017) 086045, https://doi.org/10.1088/1741-4326/aa7475

[39] K. Heinola et al., Long-term fuel retention and release in JET ITER-Like Wall at ITER-relevant baking temperatures, Nucl. Fusion 57 (2017) 086024, https://doi.org/10.1088/1741-4326/aa747e

[40] A. Baron-Wiechec et al., Global erosion and deposition patterns in JET with the ITER-like wall, J. Nucl. Mater. 463 (2015) 157-161, https://doi.org/10.1016/j.jnucmat.2015.01.038

[41] I. Jepu et al., Beryllium melting and erosion on the upper dump plates in JET during three ILW campaigns, Nucl. Fusion 59 (2019) 086009, https://doi.org/10.1088/1741-4326/ab2076

[42] J. Likonen et al., Investigation of deuterium trapping and release in the JET ITER-like wall divertor using TDS and TMAP, Nucl. Mater. Energy 19 (2019) 166-178, https://doi.org/10.1016/j.nme.2019.02.031

[43] J. Likonen et al., Investigation of deuterium trapping and release in the JET divertor during

the third ILW campaign using TDS, Nucl. Mater. Energy 19 (2019) 200-206, https://doi.org/10.1016/j.nme.2019.03.012

[44] S. Krat et al., Comparison of erosion and deposition in JET divertor during the first three ITER-like wall campaigns, Phys. Scr. T171 (2020) 014059, https://doi.org/10.1088/1402-4896/ab5c11

[45] K. Heinola et al., Experience on divertor fuel retention after two ITER-Like Wall campaigns, Phys. Scr. T170 (2017) 014063, https://doi.org/10.1088/1402-4896/aa9283

[46] M. Mayer et al., Erosion and deposition in the JET divertor during the first ILW campaign, Phys. Scr. T167 (2016) 014051, https://doi.org/10.1088/0031-8949/T167/1/014051

[47] C. Ruset et al., Deuterium and beryllium depth profiles into the W-coated JET divertor tiles after ITER-like wall campaigns, Nucl. Mater. Energy 30 (2022) 101151, https://doi.org/10.1016/j.nme.2022.101151

[48] Y. Oya et al., Comparison of hydrogen isotope retention in divertor tiles of JET with the ITER-like wall following campaigns in 2011-2012 and 2015-2016, Fusion Sci. Technol. 76 (2020) 439-445, https://doi.org/10.1080/15361055.2020.1716455

[49] F. Romenelli and JET EFDA contributors, Overview of the JET results with the ITER-like wall, Nucl. Fusion 53 (2013) 104002, https://doi.org/10.1088/0029-5515/53/10/104002

[50] G. F. Matthews et al., Plasma operation with an all metal first-wall: Comparison of an ITER-like wall with a carbon wall in JET, J. Nucl. Mater 438 (2013) S2-S10, https://doi.org/10.1016/j.jnucmat.2013.01.282

[51] A. Lahtinen et al., Deuterium retention on the tungsten-coated divertor tiles of JET ITER-like wall in 2015-2016 campaign, Fusion Eng. Des. 146 (2019) 1979-1982, https://doi.org/10.1016/j.fusengdes.2019.03.081

[52] S. Brezinsek et al., Beryllium migration in JET ITER-like wall plasmas, Nucl. Fusion 55 (2015) 063021, https://doi.org/10.1088/0029-5515/55/6/063021

[53] M. Reinelt et al., Retention mechanisms and binding states of deuterium implanted into beryllium, New J. Phys. 11 (2009) 043023, https://doi.org/10.1088/1367-2630/11/4/043023

[54] R.-D. Penzhorn et al., Tritium profiles in tiles from the first wall of fusion machines and techniques for their detritiation, J. Nucl. Mater. 279 (2000) 139-152, https://doi.org/10.1016/S0022-3115(00)00018-0

[55] R.-D. Penzhorn et al., Tritium depth profiles in graphite and carbon fibre composite materials

exposed to tokamak plasmas, J. Nucl. Mater. 288 (2001) 170-178, https://doi.org/10.1016/S0022-3115(00)00705-4

[56] E. Pajuste et al., Tritium retention in plasma facing materials of JET ITER-Like-Wall retrieved from the vacuum vessel in 2012 (ILW1), 2014 (ILW2) and 2016 (ILW3), Nucl. Mater. Energy 27 (2021) 101001, https://doi.org/10.1016/j.nme.2021.101001

[57] E. Pajuste et al., Tritium in plasma-facing components of JET with the ITER-Like-Wall, Phys. Scr. 96 (2021) 124050, https://doi.org/10.1088/1402-4896/ac29db

[58] E. Pajuste et al., Structure, tritium depth profile and desorption from 'plasma-facing' beryllium materials of ITER-Like-Wall at JET, Nucl. Mater. Energy 12 (2017) 642-647, https://doi.org/10.1016/j.nme.2017.03.017

[59] E. Pajuste et al., Comparison on the structure of the plasma-facing surface and tritium accumulation in beryllium tiles from JET ILW campaigns 2011-2012 and 2013-2014, Nucl. Mater. Energy 19 (2019) 131-136, https://doi.org/10.1016/j.nme.2019.02.011

[60] M. Matsuyama et al., Tritium assay in materials by the bremsstrahlung counting method, Fusion Eng. Des. 39-40 (1998) 929-936, https://doi.org/10.1016/S0920-3796(98)00232-4

[61] M. Matsuyama et. al., In situ observation of tritium interactions with Pd and Zr by β-ray Induced X-Ray Spectrometry, Fusion Eng. Des. 49-50 (2000) 885-891, https://doi.org/10.1016/S0920-3796(00)00326-4

# Chapter 2. Interaction of radiations with matter

## 2.1. Interaction of β-rays with matter

According to Katz and Penfold [1], relation between practical range $R$ and β-rays energy $E_\beta$ in MeV is

$$R(\text{mg/cm}^2) = 412E_\beta^{1.265-0.0954\ln E_\beta} \quad (E_\beta < 2.5 \text{ MeV}), \tag{2.1}$$

$$R(\text{mg/cm}^2) = 530\,E_\beta - 106 \qquad (E_\beta > 2.5 \text{ MeV}). \tag{2.2}$$

The maximum energy of T β-rays is 0.0186 MeV and Eq. (2.1) was applied to calculate their practical range. The practical range of T β-rays in mg/cm$^2$ is 0.586 mg/cm$^2$. The escape depth is inversely proportional to density of the materials β-rays traversing, as shown in Fig. 2.1. The density of dry air of standard temperature (0 °C) and pressure (100 kPa) is 1.2754 kg/m$^3$. Under this condition, range of T β-rays in dry air is only 4.7 mm.

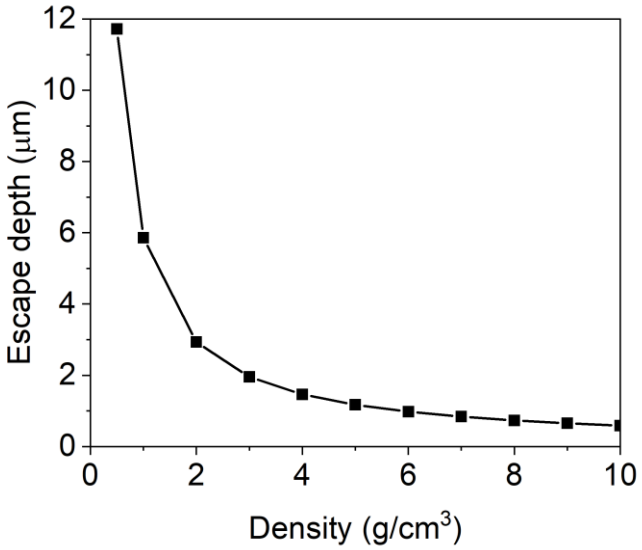


Fig. 2.1. Escape depth of T β-rays according to density of materials T traversing.

### 2.1.1. Coulomb interactions

When electrons traveling through matter, they lose energy by the interactions with atomic electrons or nucleus [2, 3]. The coulomb force between two particles is given as

$$F = k\frac{q_1 q_2}{r^2} \quad , \tag{2.3}$$

where $k$ is Coulomb's constant, $q_1$ and $q_2$ are charge of two particles and $r$ is the distance between the particles. The interaction between electrons and materials results in ionization or excitation of the atom.

Ionization occurs when the energy transferred to the atomic electron is high enough to break its bonding with nucleus [3]. The kinetic energy $E_{e^-}$ of the freed electron is

$E_{e^-}$ = (energy transferred from the charged particle to the electron) – (ionization potential).

If the energy of the electron escaped from the atom is high, the freed electron can also ionize or excite the other atoms. When the emitted electrons have enough energy to induce further ionization or excitation, they are called as δ-rays.

Excitation produces excited atom when the atomic electron received energy enough to move from low ($E_{b1}$) to high ($E_{b2}$) energy state [3]. After time of the order of $10^{-8}$ to $10^{-10}$ seconds, the excited electron stabilized and energy is emitted as X-rays with energy ($E_{b2} - E_{b1}$).

### 2.1.2. Emission of electromagnetic radiation

The charged particles are accelerated or decelerated by the interaction with materials and electromagnetic radiation is emitted as a result of energy loss [3]. This radiation is called as bremsstrahlung. Fig. 2.2 shows generation process of bremsstrahlung. Due to coulomb interaction between β-particle and atomic nucleus, β-particle is decelerated and loses its kinetic energy. The lost kinetic energy is emitted as bremsstrahlung with continuous spectrum. The energy of bremsstrahlung is equal to or lower than kinetic energy of a β-particle.

When a charged particle with charge $ze$ and mass $M$ is traveling the material with atomic number $Z$, the coulomb force $F$ is

$$F \sim \frac{zeZe}{r^2} \quad , \tag{2.4}$$

where $r$ is the distance between the particles. The acceleration of the particle is

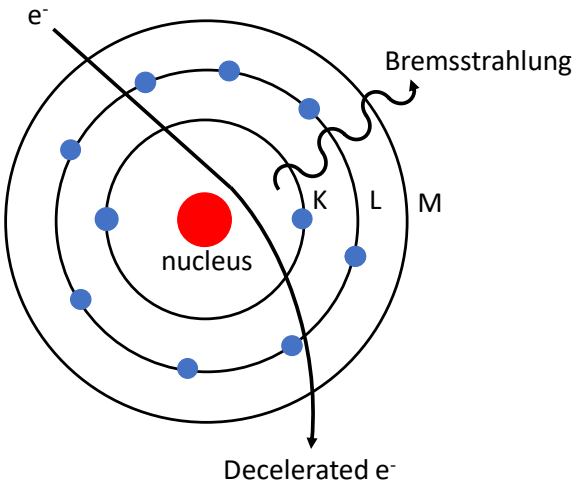


Fig. 2.2. Generation mechanism of bremsstrahlung.

$$a = F/M \sim \frac{zeZe}{M} \quad . \tag{2.5}$$

Therefore, the intensity of bremsstrahlung $I_B$ is

$$I_B \propto a^2 \sim \left(\frac{zeZe}{M}\right)^2 \sim \frac{z^2Z^2}{M^2} \quad . \tag{3} \tag{2.6}$$

The Eq. (2.6) indicates that (i) intensity of the bremsstrahlung is high when the charged particles interact with high $Z$ materials and (ii) the lighter particles generate more intense bremsstrahlung than heavier particles.

In addition to bremsstrahlung, characteristic X-rays are also generated as shown in Fig. 2.3. β-ray particle collides to electron of an atom and atomic electron is ejected. Then another electron in the outer shell fills the vacancy of target atoms inner shell. The energy difference between inner and outer shells is generated as a characteristic X-ray. Therefore, the energy of characteristic X-ray is discrete. Because the energy difference between two shells is unique for each atom, information about chemical composition of target material can be acquired.

The energy of a photon which travels with the speed of light $c$ with wavelength $\lambda_{ph}$ is

$$E_{ph} = h\nu = h\frac{c}{\lambda_{ph}} \quad . \tag{2.7}$$

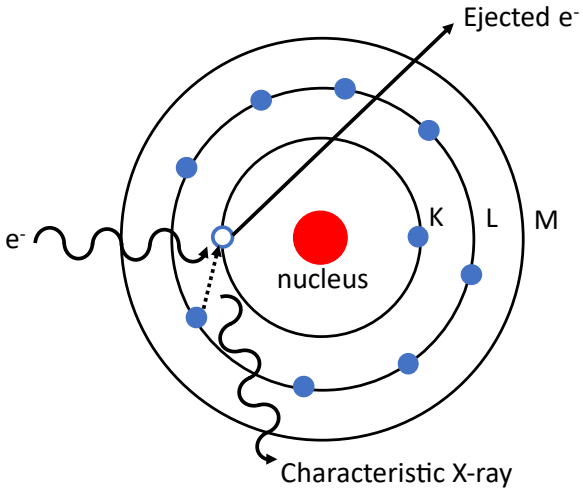


Fig. 2.3. Generation mechanism of characteristic X-ray.

2.1.3. Stopping power

The electrons travelling through materials lose their energy as a result of coulomb interactions. The averaged energy loss of electron per unit travelled distance is

$$\frac{\mathrm{d}E_\mathrm{e}}{\mathrm{d}x}\ (\mathrm{MeV/m}) = 4\pi r_\mathrm{e}^2 z^2 \frac{m_\mathrm{e}c^2}{\beta^2} NZ\left\{\ln\left(\frac{\beta\gamma\sqrt{\gamma-1}}{I_\mathrm{ex}}mc^2\right) + \frac{1}{2\gamma^2}\left[\frac{(\gamma\text{-}1)^2}{8} + 1 - (\gamma^2+2\gamma\text{-}1)\ln 2\right]\right\}, \quad [3]\ (2.8)$$

where $r_\mathrm{e}$ is $2.818 \times 10^{-15}$ m which is the classical electron radius and $m_\mathrm{e}c^2$ is the rest mass energy of the electron. $\gamma = \frac{1}{\sqrt{1-\beta^2}}$ and $\beta = v/c$ where $c$ is speed of light in vacuum. $N$ and $Z$ is the number of atoms per cubic meter (atoms/m$^3$) and atomic number of the medium material, respectively. $z$ is the charge of the electron and $I_\mathrm{ex}$ is the mean excitation potential of the material.

At low kinetic energy, stopping power is

$$\frac{dE_\mathrm{e}}{dx} \sim 4\pi r_\mathrm{e}^2 \frac{m_\mathrm{e}c^2}{\beta^2} NZ\ln\left(\frac{m_\mathrm{e}c^2\beta^2}{I_\mathrm{ex}}\sqrt{\frac{2.7182}{8}}\right) \qquad \beta << 1\,. \qquad [3]\ (2.9)$$

2.1.4. Range of charged particles

Charged particles move through materials while losing their kinetic energy by interactions with the atomic electrons and nuclei. Pathlength is the total distance the particles travelled in the medium and range $R$ is the mean distance from start to end of the pathlength [3]. Electrons are largely scattered due

to their small mass; therefore, range is shorter than pathlength. The range is given as unit m or kg/m$^2$ which is independent to state of the material. The relation between two units is

$$R\ (\mathrm{kg/m^2}) = R\ (\mathrm{m}) \times \rho\ (\mathrm{kg/m^3})\ , \tag{2.10}$$

where $\rho$ is the density of the medium material. Range is given as

$$R\ (\mathrm{kg/m^2}) = a_1\left(\frac{\ln[1+a_2(\gamma\text{-}1)]}{a_2} - \frac{a_3(\gamma\text{-}1)}{1+a_4(\gamma\text{-}1)^{a_5}}\right)\ . \tag{2.11}$$

[3]

$$a_1 = \frac{2.335A}{Z^{1.209}}$$

$$a_2 = 1.78 \times 10^{-4}\ Z$$

$$a_3 = 0.9891 - (3.01 \times 10^{-4}Z)$$

$$a_4 = 1.468 - (1.180 \times 10^{-2}Z)$$

$$a_5 = \frac{1.232}{Z^{0.109}}$$

$A$ is atomic weight and $Z$, $\gamma$, and $\beta$ were defined in subsection 2.1.3.

## 2.2. Interaction of X-rays with matter

X-rays interact with atoms in matter when they move inside the matter. The interacted X-rays are scattered or absorbed by the matter. Energy of X-rays are deposited to materials in these processes. In this section, interactions between photons and materials are introduced.

### 2.2.1. Thomson scattering

Thomson scattering is the phenomena that electromagnetic field of photon is scattered by the interaction with free electron [2]. The energy of incident photon does not change and only its path is scattered. Thomson scattering occurs when energy of incident photon is much smaller than the mass energy of the particle.

2.2.2. Photoelectric effect

The photoelectric effect is the interaction between a photon and an electron of the target material [2, 3]. As a consequence of the photoelectric effect, the photon disappeared and an electron is ejected from a target atom. The ejected electron is called as photoelectron. The kinetic energy of photoelectron $E_{pe}$ is

$$E_{pe} = h\nu - E_{\mathrm{b}}\,, \tag{2.12}$$

where $h\nu$ is energy of the photon and $E_{\mathrm{b}}$ is binding energy of the electron.

2.2.3. Compton scattering

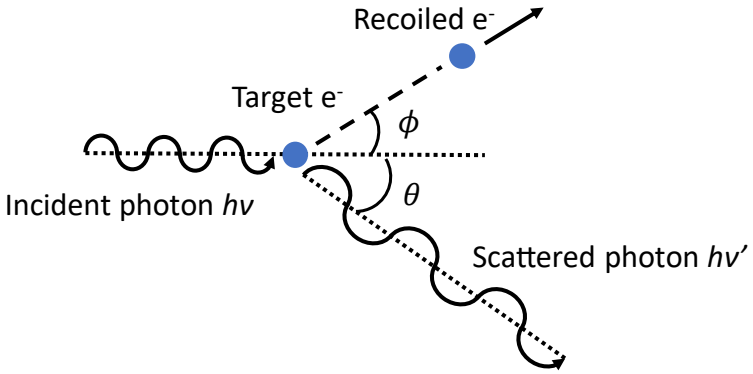


Fig. 2.4. Process of the Compton scattering.

Compton scattering is an interaction between a photon and a free electron [2, 3]. Fig. 2.4 shows process of the Compton scattering. After Compton scattering, the photon changed its direction and part of its energy is transferred to the electron. The Compton scattering induces scattering of the photon by an angle $\theta$ and reduction of the photon energy from $h\nu$ to $h\nu'$. The energy of scattered photon is

$$h\nu' = \frac{h\nu}{1+\frac{h\nu}{m_{\mathrm{e}}c^2}(1-\cos\theta)}\,. \tag{2.13}$$ [3]

From the law of conservation of energy, kinetic energy of recoiled electron becomes

$$E_{e\text{-}} = h\nu - h\nu' = h\nu\,\frac{1-\cos\theta}{1-\cos\theta + m_{\mathrm{e}}c^2/h\nu}\,, \tag{2.14}$$ [3]

when it is assumed that the electron was stationary before the collision. The energy of electron is maximum $E_{max}$ when $\theta$ is 180º.

$$E_{max} = \frac{2h\nu}{2+m_e c^2/h\nu} \quad . \qquad [3] \ (2.15)$$

2.2.4. Pair production

Pair production is interaction between a photon and a nucleus [2, 3]. After pair production, the photon disappears and an electron-positron pair produced. Therefore, the energy of photon should be at least twice of the electron rest mass, 1.022 MeV ($h\nu \geq 2m_e c^2$) in order to pair production occurs. The excess energy of photon is converted to kinetic energy of positron and electron. The energy of the photon $h\nu$ is

$$h\nu = 2m_e c^2 + E_{e^-} + E_{e^+} \, . \qquad (2.16)$$

In the Eq. (2.16), $E_{e^-}$ and $E_{e^+}$ are kinetic energy of electron and position, respectively. The energy spectrum of the electron and positron is continuous if a large number of photons are irradiated to a matter.

2.2.5. Photon attenuation coefficient

A linear attenuation coefficient $\mu$ ($m^{-1}$) is the probability of photon interactions during their penetration through materials. The value $\mu$ is inversely proportional to the density $\rho$ of the material in which photon transverses. Therefore, the mass attenuation coefficient $\mu/\rho$ is defined as

$$\mu/\rho \ (m^2/kg) = \mu \ (m^{-1})/\rho \ (kg/m^3) \, . \qquad (2.17)$$

The intensity of photons is exponentially attenuated through its path inside the target. Fig. 2.5 schematically shows decrease of number of photons from initial $I(0)$ to $I(x)$ after passing through the absorber with thickness $x$. $I(x)$ is the number of photons that escaping from the absorber and it is given by

$$I(x) = I(0)e^{-\mu x} \, . \qquad (2.18)$$

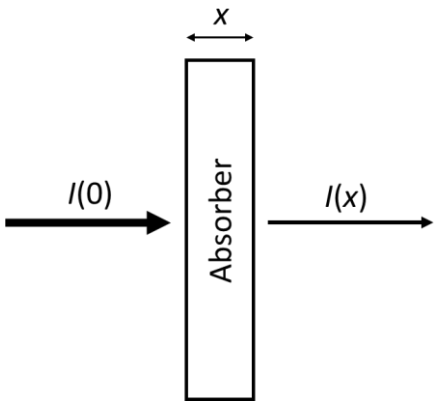


Fig. 2.5. Photons with intensity $I(0)$ attenuated to $I(x)$ by the target with thickness $x$.

The linear attenuation coefficient decreased with increasing photon energy.

The sum of photon attenuation possibilities via photoelectric effect, Compton effect and pair production is called total linear attenuation coefficient $\mu_t$. It is the total possibility of interactions between the photon and the target per unit distance. The total linear attenuation coefficient is

$$\mu_t = \tau + \sigma + \kappa \,. \tag{2.19}$$

$\tau$, $\sigma$ *and* $\kappa$ indicate attenuation coefficient for photoelectric effect, Compton effect and pair production, respectively. Fig. 2.6 is the relative importance of photon interactions with matter according to the photon energy [4]. Photoelectric effect is dominant in low energy region and Compton scattering becomes dominant around few hundred keV energy range. In high energy region above 1.022 MeV, probability of pair production increases as the energy exceeds threshold energy of the pair production.

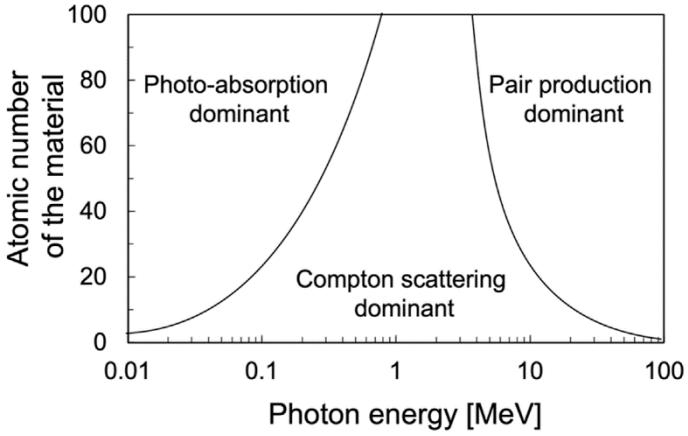


Fig. 2.6. The relative importance of photon interactions with matter [4].

References

[1] L. Katz and A. S. Penfold, Range-Energy Relations for Electrons and the Determination of Beta-Ray End-Point Energies by Absorption, Reviews of Modern Physics 24 (1952) 28-44, https://doi.org/10.1103/RevModPhys.24.28

[2] Hooshang Nikjoo, Shuzo Uehara, Dimitris Emfietzoglou, Interaction of radiation with matter, Taylor and Francis (2012) 64

[3] Nicholas Tsoulfanidis, Measurement and detection of radiation, Second edition, Taylor&Francis (1995)

[4] R. K. Parajuli et al., Development and Applications of Compton Camera—A Review, Sensors 22 (2022) 7374, https://doi.org/10.3390/s22197374

# Chapter 3. Experimental procedures

## 3.1. Tiles used in JET-ILW

### 3.1.1. Beryllium limiter tiles

Beryllium (Be) was selected as a PFM because of its relatively high melting point (1287 °C) and role as an oxygen getter to reduce plasma impurities. There are mainly three types of Be limiter tiles according to their location in the main chamber: inner wall guard limiter (IWGL), outer poloidal limiter (OPL) and upper dump plate (DP). Among the poloidal sets of IWGL, OPL and DP described in Fig. 1.10, selected tiles were extracted by remote handling and analyzed. The positions of extracted IWGL, OPL and DP, investigated in this study are shown in Fig. 3.1. IWGL (2XR10, 2XR11) and OPL (4D14, 4D15) were from mid-plane of the main chamber and DP (2BC2) was from top of high field side of the tokamak. The tiles retrieved after ILW1 or ILW3 were indicated with thick green and the tiles used during all three campaigns (ILW1-3) were shown in light green. The tiles exposed to plasma throughout ILW1 to ILW3 (ILW1-3) were poloidally neighbouring the ILW1 or ILW3 tiles. In order to evaluate erosion of Be limiter tiles, marker tiles were installed in IWGL, OPL and DP. In the Be marker tiles, Ni film with thickness 2–3 μm was sandwiched between bulk Be substrate and 7–10

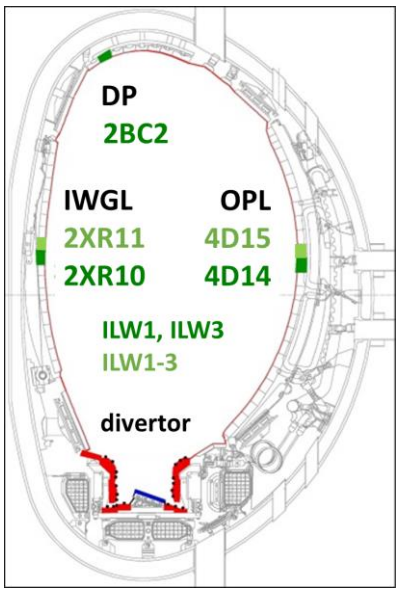


Fig. 3.1. Cross-section of JET-ILW tokamak.

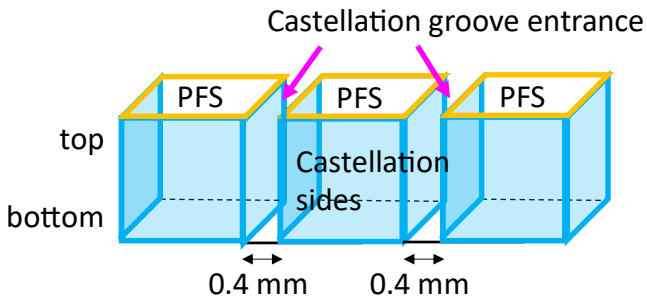


Fig. 3.2. A schematic diagram of castellated structure of JET-ILW Be limiter tiles. Plasma-facing surface (PFS) and surfaces inside the castellation grooves are indicated with yellow color and blue color, respectively.

μm-thick Be coating on the surface.

The Be limiter tiles were castellated to protect the tiles from the heat expansion caused by heat load from the plasma. Fig. 3.2 is the schematic diagram of JET-ILW Be limiter tiles. The gap distance is 0.4 mm [1]. In Fig. 3.2, PFSs are indicated in yellow color and surfaces inside the castellation gaps are shown in blue color. The surfaces in the castellation grooves are denoted as castellation sides, hereafter.

For post-mortem analyses, Be limiter tiles were cut along the castellation grooves. The selected specimens were shipped to National Institute for Quantum Sciences and Technology (QST) in Japan for analyses. Fig. 3.3 shows photos of Be limiter tiles and the locations of specimens shipped to QST. The identification numbers of ILW1, ILW3 and ILW1-3 specimens are written in black, blue and red colors, respectively. As the figure shows, two specimens were from IWGL – one from the center erosion zone (36 from ILW1, 491 from ILW3 and 640 from ILW1-3) and one from the edge deposition zone (13 from ILW1, 531 from ILW3) of IWGL – and three specimens were cut from OPL – one each from center erosion zone (127 from ILW1, 560 from ILW3 and 718 from ILW1-3), off-center erosion zone (123 from ILW1, 556 from ILW3 and 714 from ILW1-3) and edge deposition zone (160 from ILW1, 593 from ILW3) of OPL – and two positions from DP (78 and 87 from ILW1, 447 and 456 from ILW3).

Fig. 3.4 (a) is a photo of a specimen 718 from the OPL. The nominal size of a specimen is 12×12×12 $mm^3$. In Fig. 3.4 (a), PFS and castellation sides were marked with yellow color and blue color, respectively. Fig. 3.4 (b) is the optical microscope image of a castellation side.

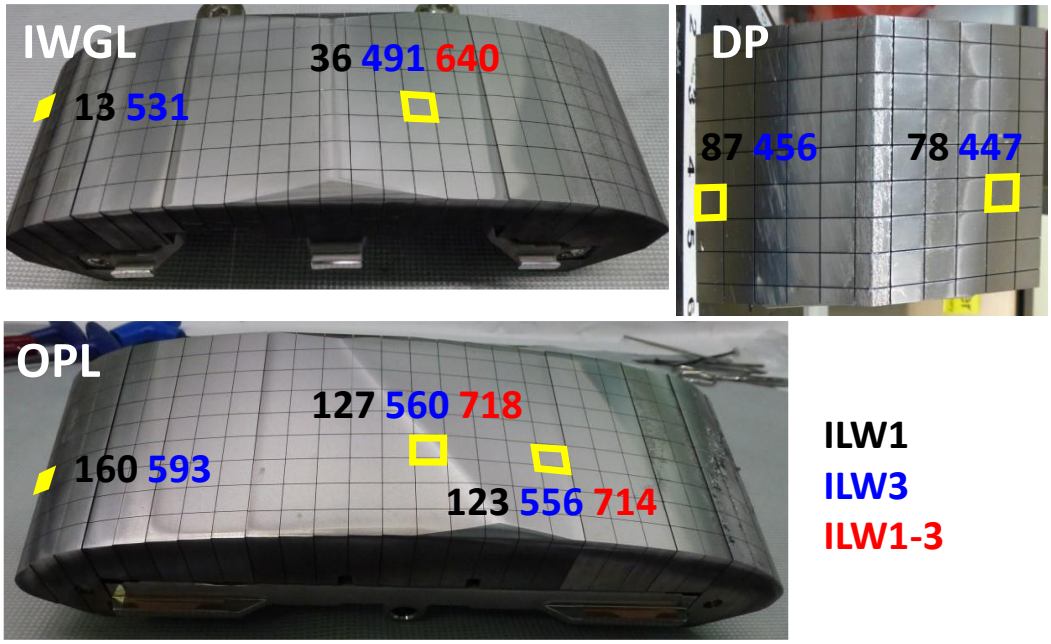


Fig. 3.3. Photos of Be limiter tiles: inner wall guard limiter (IWGL), outer poloidal limiter (OPL) and upper dump plate (DP). The identification numbers of specimens used in ILW1, ILW3 and all three campaigns (ILW1-3) are indicated with black, blue and red colors, respectively.

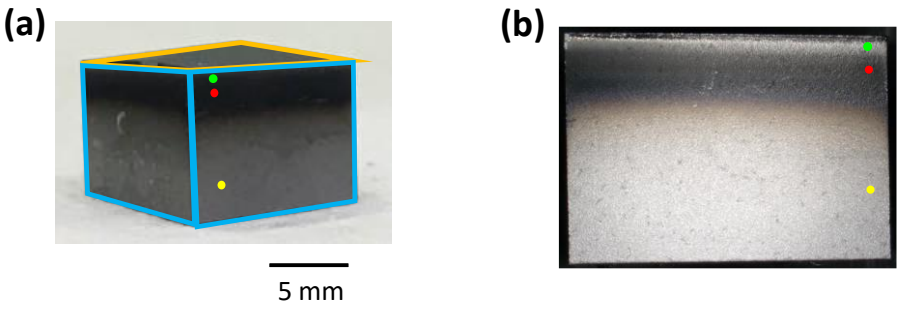


Fig. 3.4. (a) A photo of a specimen OPL 718 used in ILW1-3 and (b) the optical microscope image of ILW1 OPL 127 specimen (b). The three dots in (a) and (b) are the position analyzed with XPS.

### 3.1.2. Tungsten divertor tiles

Magnified cross-section of JET-ILW divertor is shown in right-hand side of Fig. 1.10. In the magnified image of divertor, large black numbers are indicating tile number. The small numbers are S-coordinate which is the distance along the divertor surface from the edge of Tile 0 in mm scale.

The materials used in the divertor was different according to tile position. Inner divertor tiles (Tile 0, 1, 3, 4) and outer divertor tiles (Tile 6, 7, 8) were W coated carbon-fiber-composite (W-CFC). Tile

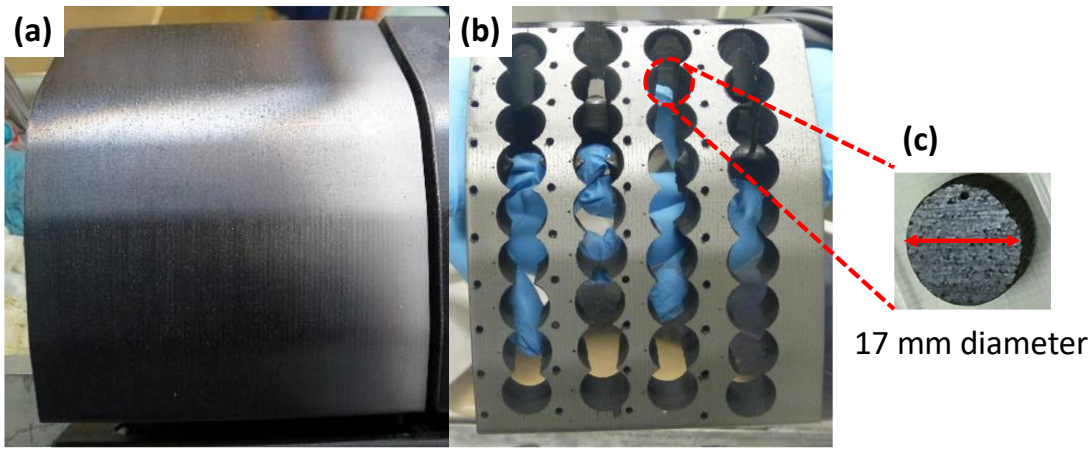


Fig. 3.5. Photos of divertor Tile 1 before (a) and after (b) cutting by coring. (c) A sample from the tile with diameter of 17 mm.

5 was stack of bulk W lamellae.

W-CFC tiles used in ILW1 or ILW3 were analyzed in this study. The location of the tiles is described in Fig. 1.10 with the magnified image of divertor region. Some W-CFC tiles had marker layers for erosion analyses. Tile 1, 3, 4, 6 and 7 were standard W coated tiles and 2–3 μm-thick Mo layer was existed between CFC substrate and W layer with 20–25 μm thickness. Tile 3 and 8 were the tiles with W marker where the tile was constructed as CFC substrate / 3 μm Mo / 12 μm W / 4 μm Mo / 4 μm W. The divertor tiles were cut by coring to get smaller samples and Fig. 3.5 shows a photo of divertor Tile 1 before (a) and after (b) cutting by coring. Fig. 3.5 (c) is a photo of a sample and a diameter of the sample from the W-CFC tiles was 17 mm.

Fig. 3.6 is a schematic diagram of bulk W lamellae tile. A thin W lamella was stacked in 24 layers in toroidal direction (1 to 24) and 4 layers in poloidal direction (A to D) and identification of the stacks are written in white letters. Fig. 3.6 (b) is a magnified image of a single lamella. In Fig. 3.6 (b), the PFSs and surfaces between lamellae gaps of Tile 5 is indicated with yellow color and blue color, respectively.

Samples from Tile 5 bulk W lamellae were prepared by cutting along red lines in Fig. 3.6 (b). Three samples were investigated after ILW1 and ILW3. In Fig. 3.6 (a), identification number of ILW1 and ILW3 samples is written in black and red colors, respectively. The tiles with green color were standard bulk W tiles. Tiles indicated in pink color were marker coated tiles with 6 μm Mo interlayer between W substrate and 6 μm W layer. Tile 5 was tilted in JET vacuum vessel and the part of PFSs of lamella was shadowed by the neighbor lamellae. The PFSs of lamellae in row 24 were exposed to plasma

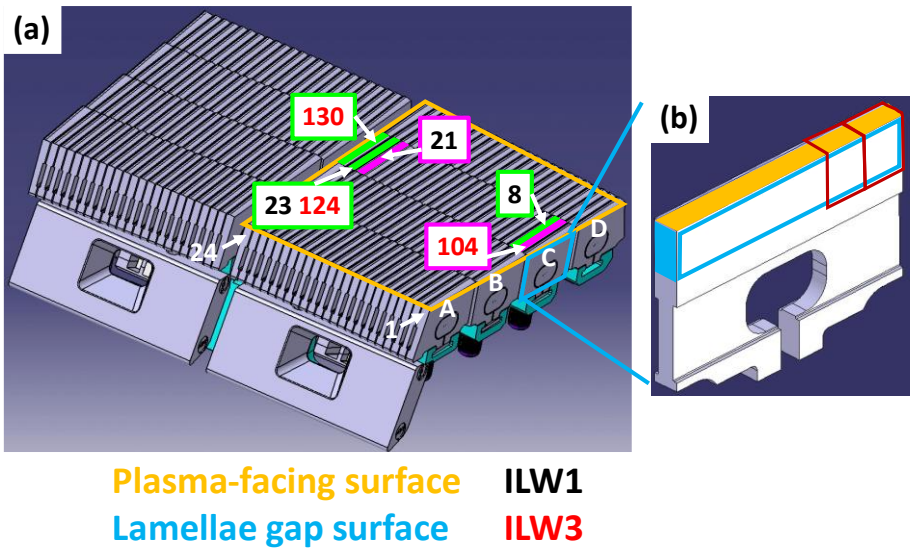


Fig. 3.6. (a) Schematic diagram of bulk W lamellae Tile 5 and (b) magnified image of a lamella. White numbers are identification of stacks. In Fig. 3.6 (b), PFS and lamellae gap surfaces is indicated with yellow and blue, respectively. The identification number of samples cut from the tiles used in ILW1 are written in black and that of ILW3 samples are written in red. Green and pink colors are identification of the tile positions. Green-colored tiles were standard W tile and pink-colored tiles were marker coated tile with 6 μm Mo interlayer between W substrate and 6 μm W layer.

while PFSs of row 1 lamellae were shadowed to plasma by the neighbouring tiles. Therefore, PFSs of samples 8 and 104 were shadowed from plasma and those of samples 21, 23, 124 and 130 were exposed to the plasma.

## 3.2. Analysis methods

### 3.2.1. Imaging plate (IP) technique

Imaging plate (IP) is a sheet covered with phosphor layer which is sensitive to radiation. There are several different types of IPs which are sensitive to neutrons, X-rays or low energy β-rays. In this study, IP sheets for T β-rays detection (β-IP, BAS IP TR, GE Healthcare Japan) and X-ray detection (X-IP, BAS IP MS, GE Healthcare Japan) were used.

Fig. 3.7 is structure of the β-ray sensitive IP. As a phosphor layer, barium bromide fluoride doped with $Eu^{2+}$ ($BaFBr:Eu^{2+}$) is used. $Eu^{2+}$ works as a color center and 5 μm-thick phosphor layer was

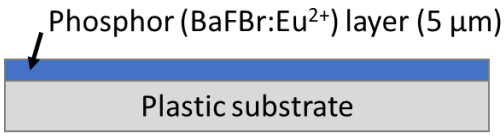


Fig. 3.7. Structure of imaging plate sensitive to β-rays.

coated on plastic substrate. The phosphor layer of X-IP is covered with protective layer for the resistance against water.

Fig. 3.8 (a) is a band diagram of IP phosphor layer. For the simplicity, process of practical use of β-IP is explained in the following. When IP is irradiated with β-ray particle as described in Fig. 3.8 (b), irradiation of IP with β-ray particle results in production of electron-hole pair. The electron excited to conduction band is trapped at F or Br vacancy, and form color centers. On the other hand, the hole oxidizes $Eu^{2+}$ to $Eu^{3+}$. The concentration of the color center and $Eu^{3+}$ is proportional to fluence of β-rays. To read-out the image, IP is scanned with He-Ne laser scanner, as described in Fig. 3.8 (c). By the exposure to laser light, electrons in metastable state are excited again to conduction band and relaxed to valence band. This process, $Eu^{3+}$ ions become excited $Eu^{2+}$ by gaining the electrons and photo-stimulated luminescence (PSL) with 3.2 eV energy is generated during relaxation of excited

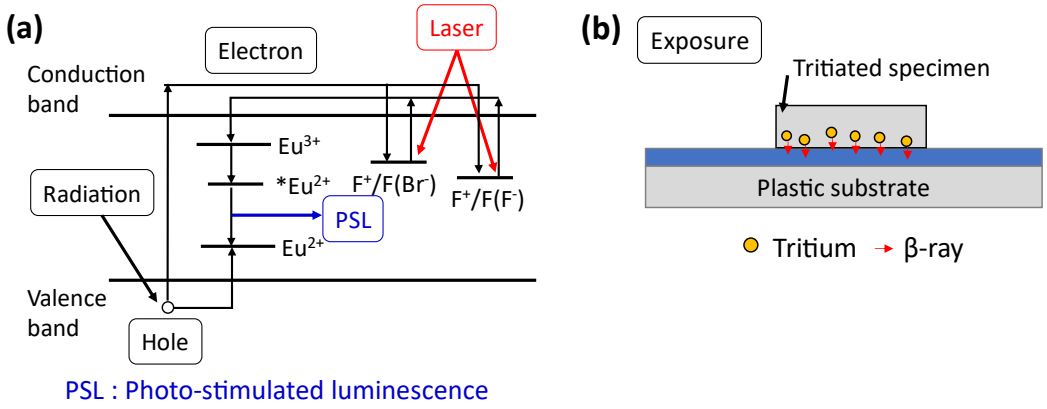


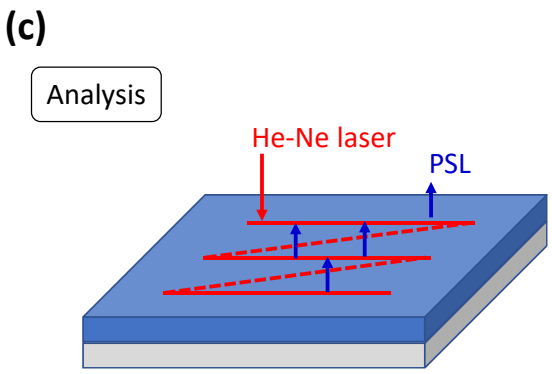


Fig. 3.8. (a) Band diagram of IP phosphor layer (BaFBr:$Eu^{2+}$) and (b) schematic diagram of exposure process of T β-rays to imaging plate. (c) is read-out process of fluorescence from IP.

$Eu^{2+}$ ions.

The energy of T β-rays (≤ 18.6 keV) is low. According to practical range of T β-rays in $mg/cm^2$ which calculated with Eq. (2.1), the escape depth of T β-rays in Be and W is evaluated as below when assuming the density of Be as 1.85 $g/cm^3$ and that of W as 19.3 $g/cm^3$.

$$\text{Be:} \quad \frac{0.586\ \text{mg/cm}^2}{1.85\ \text{g/cm}^3} = 3.17\times10^{-4}\ \text{cm} = 3.17\ \mu\text{m}\ . \tag{3.1}$$

$$\text{W:} \quad \frac{0.586\ \text{mg/cm}^2}{19.3\ \text{g/cm}^3} = 3.04\times10^{-5}\ \text{cm} = 0.304\ \mu\text{m}\ . \tag{3.2}$$

Thus, IP technique gives information about T retained in the range of several μm or less, within the escape depths of T β-rays.

To get 2-dimensional distribution of T on specimens, IP is irradiated by T β-rays or X-rays generated from β particles. Fig. 3.9 is a photo of β-IP with a Be limiter specimen. The specimens were in contact with β-IP sheets from 1 to 26 hours or X-IP sheets from 69 to 126 hours, according to expected T concentration. As shown in Fig. 3.9, a standard sample which is a set of plastic sheets labelled with known amounts of T was also put on the IP together with the specimens. W-Th rod was also used as a reference because half-life of Th is long ($1.4 \times 10^{10}$ y). The laser scanner used in this study was FLA-7000, Fujifilm, Japan.

Fig. 3.10 (a) is the IP image of a T standard sample (ART-123A, American Radiolabeled Chemicals, Inc.) obtained with β-IP. The region with high PSL intensity is indicated with red and the color changes from red to orange, yellow, green and blue as the PSL intensity decreased. The radioactivity of the plastic piece with highest T concentration was 7390 nCi/mg on the calibration date, 2014 July 12th.

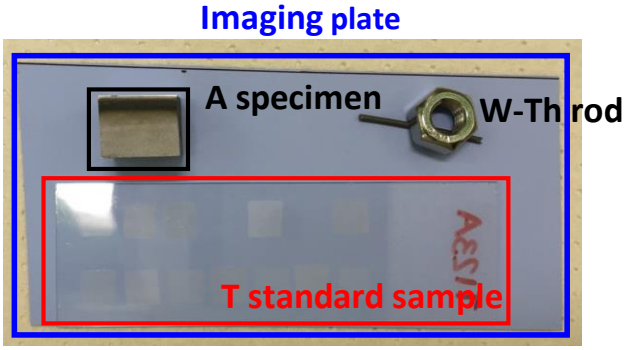


Fig. 3.9. A photo of exposure process of T β-rays to β-ray sensitive imaging plate.

The approximate weight of a single piece is 0.358 mg ± 10 %. Therefore, the radioactivity of the piece was

$$7490 \text{ nCi/mg} \times 0.358 \text{ mg} = 2680 \text{ nCi} . \quad (3.3)$$

1 Ci is equivalent to $3.7\times10^{10}$ Bq, and hence

$$2680 \text{ nCi} \times 3.7\times10^{10} \text{ Bq/Ci} = 99000 \text{ Bq} . \quad (3.4)$$

The density and surface area of the plastic piece is 1 g/cm$^3$ and 0.35 cm$^2$, respectively. The thickness is 10 μm. Therefore, the concentration of T in the piece was

$$\frac{99000 \text{ Bq}}{0.35 \text{ cm}^2 \times 10\times10^{-4} \text{ cm}} = 2.8\times10^{8} \text{ Bq/cm}^3 \quad (3.5)$$

on the calibration date. The radioactivity of the standard sample in the day of measurement was calculated by Eq. (1.5).

The PSL intensity is plotted against the calculated radioactivity in Fig. 3.10 (b). As shown in Fig. 3.10 (b), the PSL intensity was proportional to the radioactivity of T. Thus, quantitative analyses of T concentration are possible by applying IP technique. T retention of the day of tile retrieval from JET

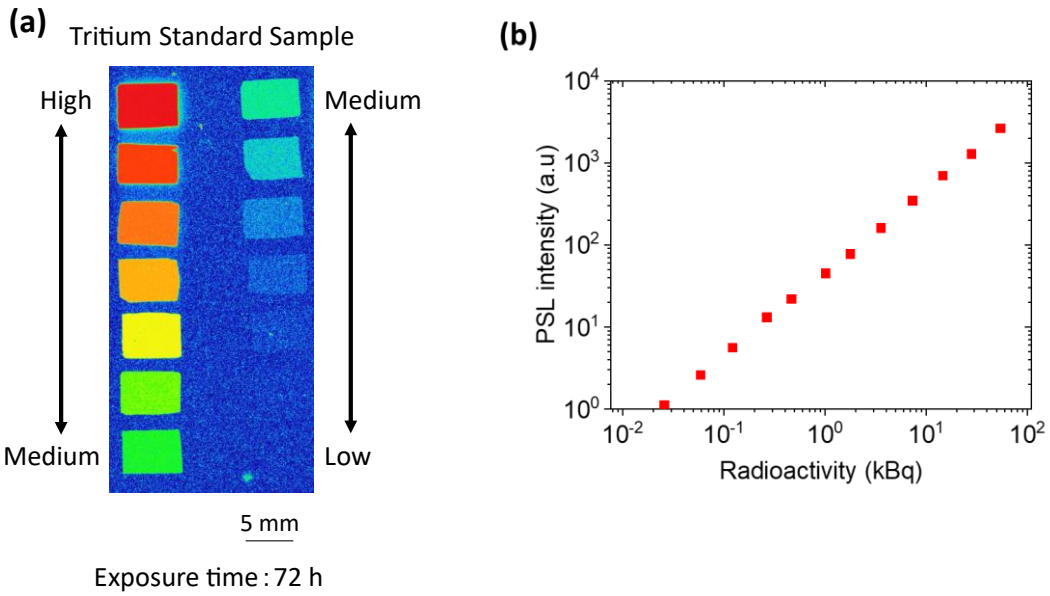


Fig. 3.10. (a) IP image of T standard sample (ART-123A, American Radiolabeled Chemicals, Inc) labelled with known amounts of T acquired with β-IP. (b) Correlation between T radioactivity and PSL intensity.

vacuum vessel was calculated by considering half-life of T by radioactive decay.

### 3.2.2. Beta-ray induced X-ray spectrometry (BIXS)

In β-ray induced X-ray spectrometry (BIXS) [2, 3], energy spectrum of X-rays induced by the β-rays from T is measured. Bremsstrahlung and characteristic X-rays are generated by T β-rays. The generation mechanisms of bremsstrahlung and characteristic X-rays are explained in section 2.1.

Due to longer escape depths of X-rays than β-rays, X-ray analysis by BIXS can give information about T retained beyond the escape depth of β-rays. Fig. 3.11 shows simplified generation processes of β-ray induced X-rays in a (a) shallowly-contaminated sample and (b) bulk-contaminated sample. Attenuation of generated X-rays by the specimen and surrounding gas can be calculated with Eq. (2.18) according to Beer-Lambert law. The X-rays induced by T β-rays have kinetic energy lower than T β-rays (≤ 18.6 keV). Therefore, the attenuation by photoelectric effect is dominant in T-containing materials according to Fig. 2.6.

When T is retained in W sample, β-particles can induce W(Lα) X-rays at 8.40 keV and W(Mα) X-rays at 1.78 keV energy. The database provided by National Institute of Standards and Technology (NIST) [4] gives the list of mass attenuation coefficient of elements. From the values in the list, the mass attenuation coefficients for 8.40 keV and 1.78 keV X-rays in W are evaluated to be 155 $cm^2/g$ and 1160 $cm^2/g$ respectively, by assuming linear dependence of the coefficient on energy in the energy region of interest. The intensity ratio of 8.40 keV W(Lα) X-rays before and after traverse 10 nm-thick

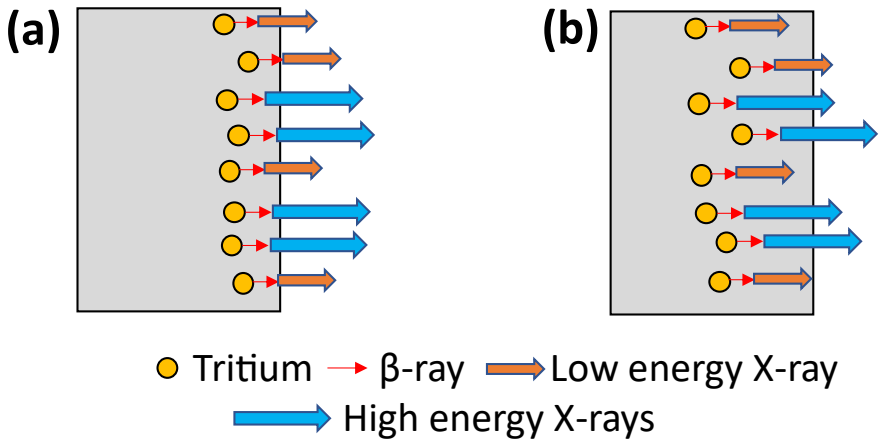


Fig. 3.11. Generation processes of β-ray induced X-rays for (a) shallowly-contaminated sample and (b) bulk-contaminated sample.

W with 19.3 g/cm$^3$ density is

$$I_{W(L\alpha)}(10\ \text{nm})/\ I_{W(L\alpha)}(0) = e^{(-155\ \text{cm}^2/\text{g} \times 19.3\ \text{g/cm}^3 \times 10\times10^{-7}\ \text{cm})} = 0.99\ . \quad (3.6)$$

The intensity ratio of 1.78 keV W(Mα) X-rays under same conditions is

$$I_{W(M\alpha)}(10\ \text{nm})/\ I_{W(M\alpha)}(0) = e^{(-1160\ \text{cm}^2/\text{g} \times 19.3\ \text{g/cm}^3 \times 10\times10^{-7}\ \text{cm})} = 0.98\ . \quad (3.7)$$

The results showed insignificant difference in attenuation between high energy W(Lα) X-rays and low energy W(Mα) X-rays. When the thickness of the W slab increases to 1 μm, the calculation changed like the followings:

$$I_{W(L\alpha)}(1\ \mu\text{m})/\ I_{W(L\alpha)}(0) = e^{(-155\ \text{cm}^2/\text{g} \times 19.3\ \text{g/cm}^3 \times 1\times10^{-4}\text{cm})} = 0.74\ , \text{and} \quad (3.8)$$

$$I_{W(M\alpha)}(1\ \mu\text{m})/\ I_{W(M\alpha)}(0) = e^{(-1160\ \text{cm}^2/\text{g} \times 19.3\ \text{g/cm}^3 \times 1\times10^{-4}\text{cm})} = 0.11\ . \quad (3.9)$$

Fig. 3.12 shows relative intensity of W(Mα) X-rays and W(Lα) X-rays escaped from pure W as a function of W thickness. This figure denoted that the difference in extent of attenuation between W(Mα) X-rays and W(Lα) X-rays increases as the travel distance increases.

In BIXS system, X-rays induced by β-rays were detected by silicon drift detector (SDD) as depicted in Fig. 3.13 (a). Fig. 3.13 (b) is a photo of measurement set up. The SDD (X-123SDD, AMPTEK Inc.,

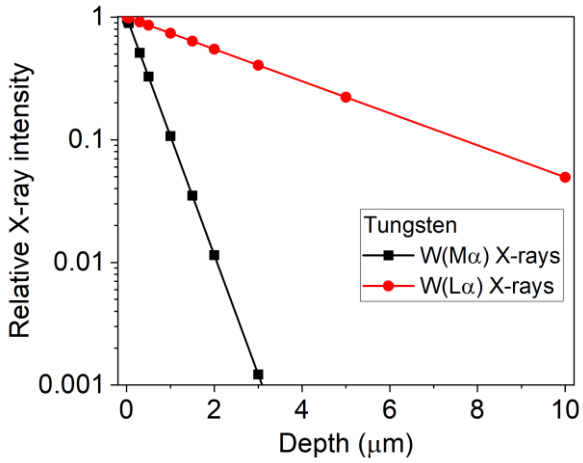


Fig. 3.12. Relative intensity of W(Mα) X-ray and W(Lα) X-rays escaped from pure W as a function of depth of X-ray generation.

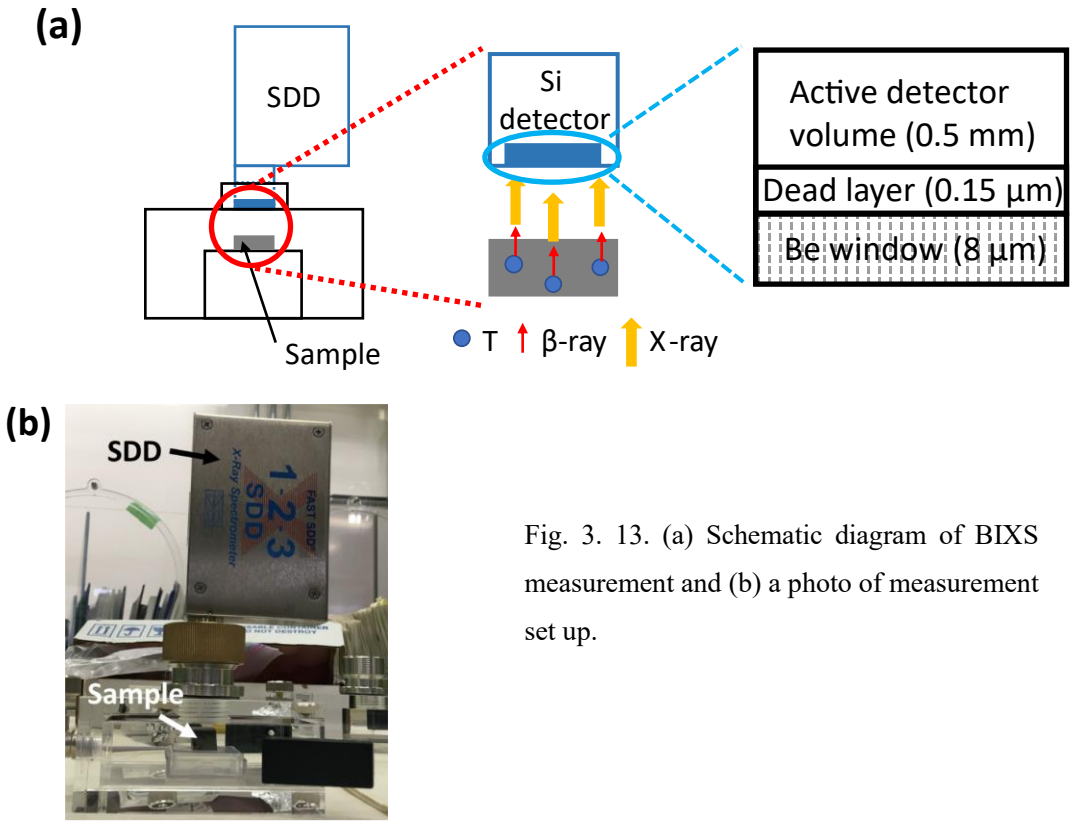


Fig. 3. 13. (a) Schematic diagram of BIXS measurement and (b) a photo of measurement set up.

USA) used in this study is cooled by a Peltier element and portable. The structure of the SDD was referred to the information provided by the manufacturer [5]. The SDD has 8 μm-thick Be window and X-rays with energy lower than 0.6 keV are totally attenuated by the window. The thickness of active detector volume is 0.5 mm [5]. A semiconductor detector has dead layer where the incident radiation should pass to reach the depletion region [6] and the dead layer thickness of the SDD used in this study is 0.15 μm [5]. The measurements were carried out under argon (Ar) gas atmosphere. The distance between the specimens and the detector window was set to be 5 mm.

### 3.2.3. Monte Carlo simulation and Geant4

Monte Carlo methods are computational algorithms which calculate numerical results by repeating large number of random samplings. They are used to solve mathematical and physical problems. In order to analyze BIXS spectra, Geant4 [7 – 10], a tool of Monte Carlo simulation, was applied. Geant4 simulates the passage of particles through matter using Monte Carlo methods [7].

The software has been applied to radiation physics, space science and nuclear medicine and it

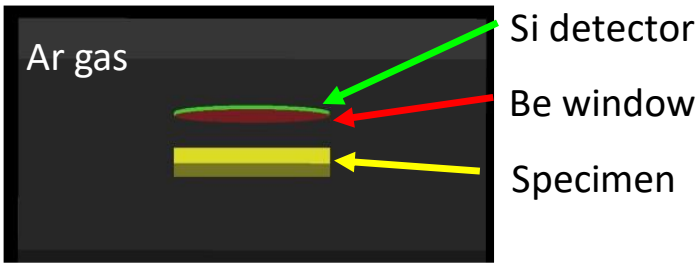


Fig. 3.14. Geometry of BIXS measurements constructed in Geant4 system.

contains a variety of physical programs. The Geant4 software system contains the following components: event generator, detector simulation, reconstruction and analysis [7].

The experimental condition of BIXS measurements were virtually constructed in Geant4 system. Fig. 3.14 is the geometry of the simulations. The structure of the SDD was based on information [5] provided by the manufacturer, AMPTEK Inc. X-rays generated by the interactions between T β-rays and materials composing the virtual system, i.e., specimen, Ar gas, Be window, Si dead layer, are detected by the Si active layer built in the simulation geometry.

The Electromagnetic (EM) physics of Geant4 was developed to simulate electromagnetic interactions of charged particles [8]. There are sub-packages for low energy electromagnetic physics models, e.g., Penelope models, Livermore models, Elastic models, Geant4-DNA etc. [8]. The Röllig et al. conducted Geant4 simulation of X-rays spectrum induced by T β-rays with several different electromagnetic physics packages to obtain BIXS spectra and examined the difference in spectral shape and detection efficiency [9]. The X-ray spectra calculated under PENELOPE physics [10] showed the best agreement with experimentally-obtained spectra [9]. Therefore, the calculation of electromagnetic interactions by particles were done under PENELOPE physics package in Geant4 in this study.

The influence of SDD internal structure to BIXS spectrum was investigated [11]. A plate of W (10 × 10 × 2 $mm^3$) irradiated with 20 MeV W ions up to 0.5 displacement per atom was used as a sample. The defects induced by irradiation act as traps against hydrogen isotopes up to a depth of 2 μm. The W ion-irradiated sample was exposed to D-5%T mixture gas at 773 K for 3 h. According to nuclear reaction analysis (NRA) of D in a sample, exposed to $D_2$ gas under similar conditions, the hydrogen isotope was distributed almost uniformly up to the depth of 2 μm [12]. Therefore, W sample in which T was uniformly distributed from surface to 2 μm depth was constructed in Geant4 system to acquire

BIXS spectrum. The X-ray spectra obtained from BIXS measurements and Geant4 showed good agreement beyond 2 keV energy range. However, the attenuation of X-rays with energy less than 2 keV was overestimated in Geant4 [11].

### 3.2.4. X-ray photoelectron spectroscopy (XPS)

X-ray photoelectron spectrometry (XPS) is a technique for quantitative analysis of chemical composition of a material surface and binding states of elements. Fig. 3.15 describes the photoelectron emission process from an atom. When photon is bombarded to a material, electrons are emitted by the photoelectric effect, as described in subsection 2.2.2. XPS determines the binding energy $E_b$ of electrons emitted by the bombardment of X-rays from the following equation;

$$E_{pe} = h\nu - E_b - \varphi_s \,, \tag{3.10}$$

where $E_{pe}$ is the kinetic energy of photoelectron and $\varphi_s$ is the work function of a sample [13]. An element has its unique electron binding energies and therefore the concentration of surface composing elements can be evaluated [13]. Also, chemical states of elements can be determined because variations in the binding energy caused by differences in chemical potential and polarizability of compounds [13].

In homogeneous sample, the number of emitted photoelectrons in unit time is

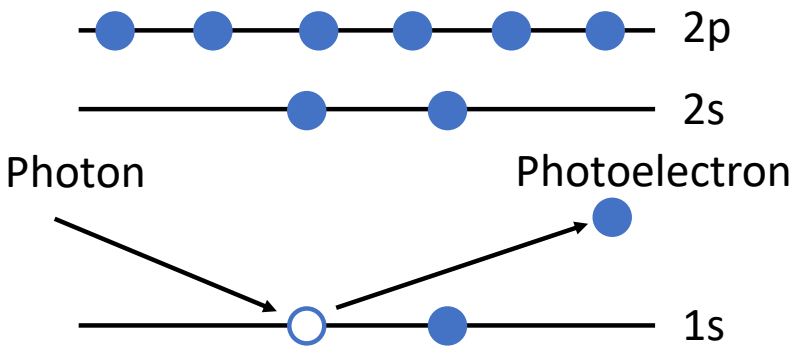


Fig. 3.15. The XPS emission process of a model atom.

$$I_{pe} = nf\sigma_{pe}\theta_{eff}ylD\varepsilon \,, \tag{3.11}$$

where $n$ is the number of atoms of the element per $cm^3$, $f$ is flux of X-rays in photons/$cm^2$s, $\sigma_{pe}$ is the photoelectric cross-section for the atomic orbital of interest in $cm^2$, $\theta_{eff}$ is angular efficiency factor, $y$ is the photoelectric process efficiency for formation of photoelectrons of the normal photoelectron energy, $l$ is mean free path of the photoelectrons, $D$ is the area of analyzed region and $\varepsilon$ is detection efficiency [13]. From Eq. (3.11),

$$n = I_{pe}/f\sigma_{pe}\theta_{eff}ylD\varepsilon \tag{3.12}$$

can be obtained and the denominator of Eq. (3.12) is defined as the atomic sensitivity factor, $S$ [13]. Therefore, a correlation of number of photoelectrons from two elements is

$$\frac{n_1}{n_2} = \frac{I_1/S_1}{I_2/S_2} \,. \tag{3.13}$$

The atomic sensitivity factors of each element used in this study were 0.074 for Be, 0.711 for O, 0.296 for C, 0.477 for N, 2.959 for W, 3.653 for Ni, 0.193 for Al and 4.798 for Cu [13].

The deposition layers formed on castellation sides of Be limiter tiles were analyzed with XPS device (PHI 5000 VersaProbe II, Ulvac-Phi Inc., Japan). Monochromatized Al(Kα) radiation with 1486.6 eV energy was used for photoelectron generation. The diameter of analyzed area was 100 μm. The depth profiles of elements which composing the deposition layers were obtained by sputtering the specimen surfaces in the area of 2 mm×2 mm with 3 keV $Ar^+$ ion beam at the incident angle of 33°.

References


[1] M. Rubel et al., Fuel inventory and deposition in castellated structures in JET-ILW, Nucl. Fusion 57 (2017) 066027, https://doi.org/10.1088/1741-4326/aa6864

[2] M. Matsuyama et al., Tritium assay in materials by the bremsstrahlung counting method, Fusion Eng. Des. 39-40 (1998) 929-936, https://doi.org/10.1016/S0920-3796(98)00232-4

[3] M. Matsuyama et. al., In situ observation of tritium interactions with Pd and Zr by β-ray Induced X-Ray Spectrometry, Fusion Eng. Des. 49-50 (2000) 885-891, https://doi.org/10.1016/S0920-3796(00)00326-4

[4] J. H. Hubbell and S. M. Seltzer, NIST Standard Reference Database 126, https://www.nist.gov/pml/x-ray-mass-attenuation-coefficients

[5] https://www.amptek.com/internal-products/obsolete-products/sdd-x-ray-detectors-for-xrf/x-123sdd-complete-x-ray-spectrometer-with-silicon-drift-detector-sdd

[6] Glenn F. Knoll, Radiation detection and measurement, (New York: John Wiley & Sons, Inc., (1971) 387.

[7] S. Agostinelli et al., GEANT4—A Simulation Toolkit, Nucl. Instrum. Meth. Phys. Res. A, 506 (2003) 250-303, https://doi.org/10.1016/S0168-9002(03)01368-8

[8] https://geant4.web.cern.ch/collaboration/working_groups/electromagnetic

[9] M. Röllig et al., Galet—Benchmark of a Geant4 based application for the simulation and design of Beta Induced X-Ray Spectrometry systems, Fusion Eng. Des., 143 (2019) 91-98, https://doi.org/10.1016/j.fusengdes.2019.03.086.

[10] J. Baró et al., PENELOPE: An algorithm for Monte Carlo simulation of the penetration and energy loss of electrons and positrons in matter, Nucl. Instrum. Meth. Phys. Res. B 100 (1995) 31-46, https://doi.org/10.1016/0168-583X(95)00349-5

[11] S. E. Lee et al., Influence of internal structure of semiconductor detector on X-ray induced by tritium beta rays, Fusion. Sci. Tech. 76 (2020) 327-332, https://doi.org/10.1080/15361055.2020.1711855

[12] Y. Hatano et al., Trapping of Hydrogen Isotopes in Radiation Defects Formed in Tungsten by Neutron and Ion Irradiations, J. Nucl. Mater. 438 (2013) S114, https://doi.org/10.1016/j.jnucmat.2013.01.018

[13] John F. Moulder, Handbook of X-ray Photoelectron Spectroscopy, Physics Electronics, Inc. (1995) 10

# Chapter 4. Tritium distribution in main chamber limiter

## 4.1. Plasma-facing surfaces

The plasma-facing surfaces (PFSs) of specimens from Be limiter tiles were analyzed by IP technique. Fig. 4.1 shows the IP results of specimens from (a) IWGL, (b) OPL and (c) DP. In Fig. 4.1, the red-colored area of IP images are the regions with high PSL intensity, and low PSL intensity regions are shown in blue color. The identification number of specimens exposed to plasma during ILW1, ILW3 and ILW1-3 are indicated in black, blue and red colors, respectively. The PSL intensity acquired from each specimen was normalized by the PSL intensity of the T standard piece with highest T concentration and plotted in Fig. 4.2.

In Figs. 4.1 (a) and 4.2 (a), PSL intensity was similar in IWGL specimens after each campaign regardless of specimen position. In the case of OPL in Figs. 4.1 (b) and 4.2 (b), PSL intensity of ILW3 specimens was higher than that of ILW1 specimen. Also, the specimens cut from erosion zone showed

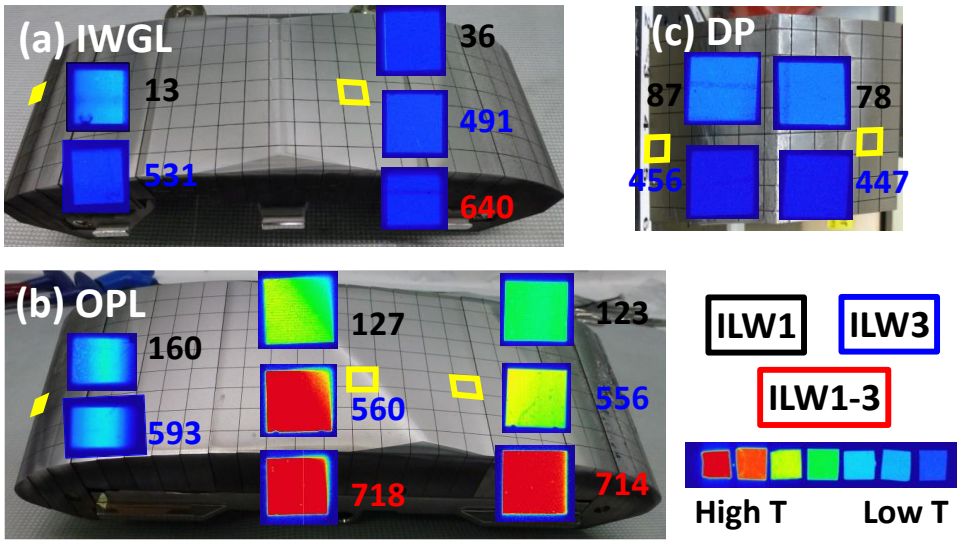


Fig. 4.1. IP results of specimens PFS from (a) IWGL, (b) OPL and (c) DP. The red-colored area of the IP is the region with high PSL intensity while low PSL intensity region is shown in blue. The identification numbers of specimens exposed to the plasma during ILW1, ILW3 and ILW1-3 are written in black, blue and red, respectively.

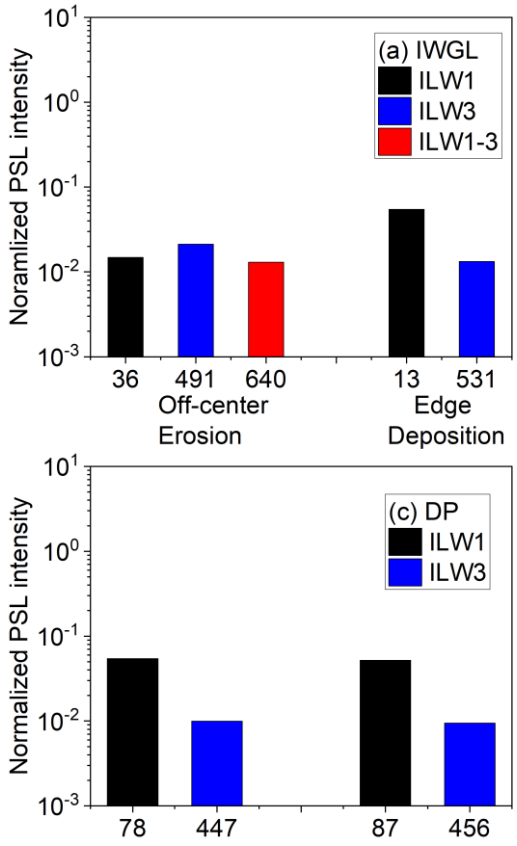


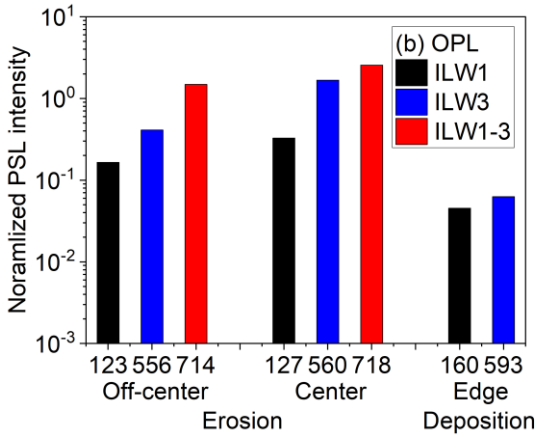


Fig. 4.2. PSL intensity of specimens from (a) IWGL, (b) OPL and (c) DP after each experimental campaign.

higher PSL intensity than specimens from deposition zone. This tendency was opposite to D retention profile on PFS of OPL [1, 2]; D concentration was higher in the deposition zone than the erosion zone. It suggests different retention mechanisms between T and D during JET-ILW experiment. In Figs. 4.1 (c) and 4.2 (c) showing PSL intensity from DP specimens, the difference between two positions were insignificant and the PSL intensity was lower in ILW3 specimens than ILW1 specimens. PSL intensity of OPL PFS was higher than that of IWGL and DP by and order of magnitude while D retention in all three tiles were similar in an order of $10^{18}$ atoms/cm$^2$ [1 – 3].

The X-ray spectrum was obtained by BIXS technique and Fig. 4.3 shows the spectra of specimens from (a) OPL center, (b) OPL off-center and (c) OPL edge. The spectra of IWGL and DP specimens were not shown because the X-ray intensity was too weak to get spectrum with sufficient signal to noise ratio. In Fig. 4.3, the X-ray intensity of specimens from OPL center was higher than that of specimens from off-center or edge. These tendencies agreed to PSL intensity for those observed in Figs. 4.1 and 4.2.

The spectral shape was different whether erosion or deposition mainly occurred on the PFS. In the case of eroded PFS as shown in Fig. 4.3 (a) and (b), low energy bremsstrahlung and Ar(Kα) X-ray

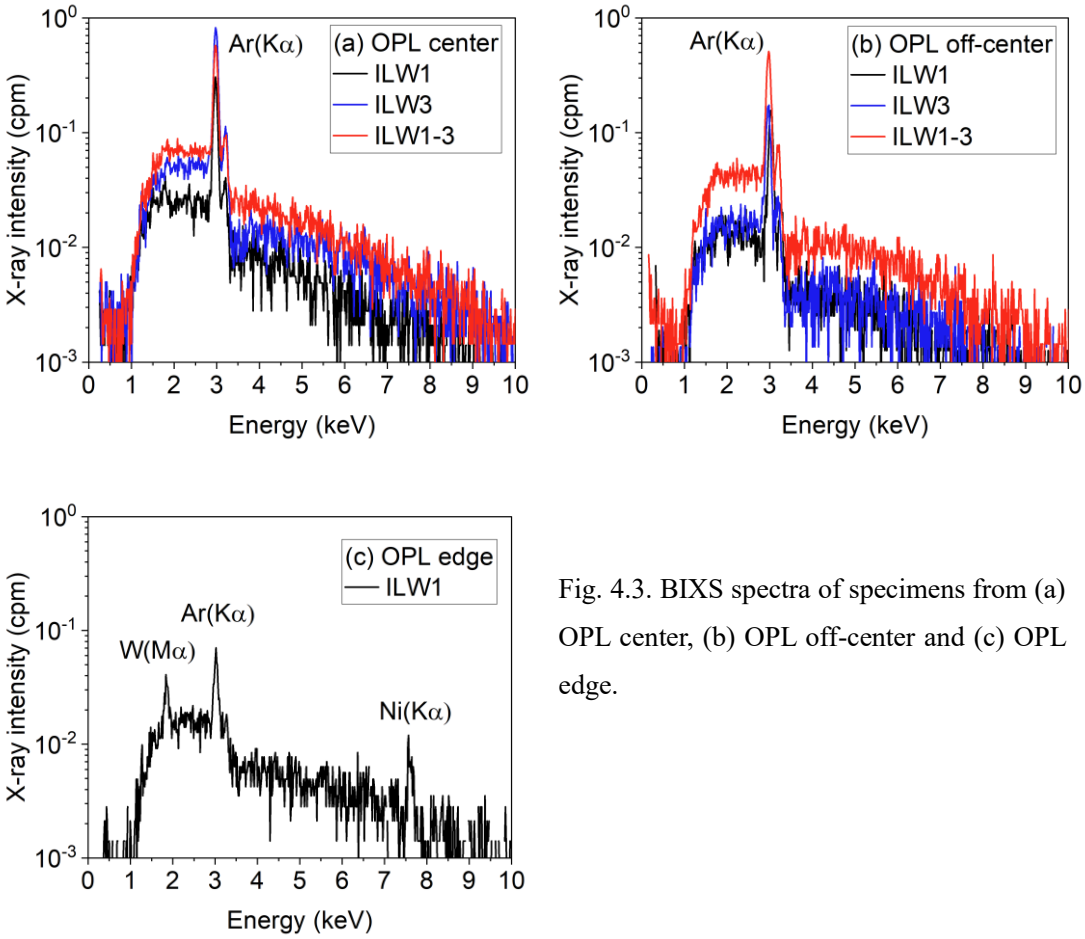


Fig. 4.3. BIXS spectra of specimens from (a) OPL center, (b) OPL off-center and (c) OPL edge.

induced by interaction between Ar gas in the measurement atmosphere and β-rays were intense compared with high energy X-rays. On the other hand, the shape of X-ray spectrum was different in the specimen from the edge as in Fig. 4.3 (c). The area covered with deposition layer showed characteristic X-rays of metal impurities, e.g., W(Mα) X-rays and Ni(Kα) X-rays in addition to Ar(Kα) X-rays. It indicated existence of W and Ni in the T-containing deposition layer. In addition, the intensity of low energy bremsstrahlung and Ar(Kα) X-rays was relatively weak.

As mentioned in subsection 3.2.2, the shape of X-ray spectrum gives information about T retention depth because of difference in X-ray attenuation coefficient according to energy of X-rays. Therefore, the X-ray spectra were analyzed by Geant4 to determine T retention profile. Several X-ray spectra were obtained by Geant4 by assuming different T depth profile as described and plotted in Fig. 4.4. Fig. 4.4 (a) describes the T depth profiles constructed in Geant4 system. In the simulation geometry, it was assumed that T was uniformly distributed up to 1 μm (black), 3 μm (red), 6 μm (green), 8 μm (blue) or 10 μm (light blue). The obtained spectra were given in Fig. 4.4 (b). The difference in shape of bremsstrahlung spectra was insignificant. However, contribution of Ar(Kα) X-rays intensity to total

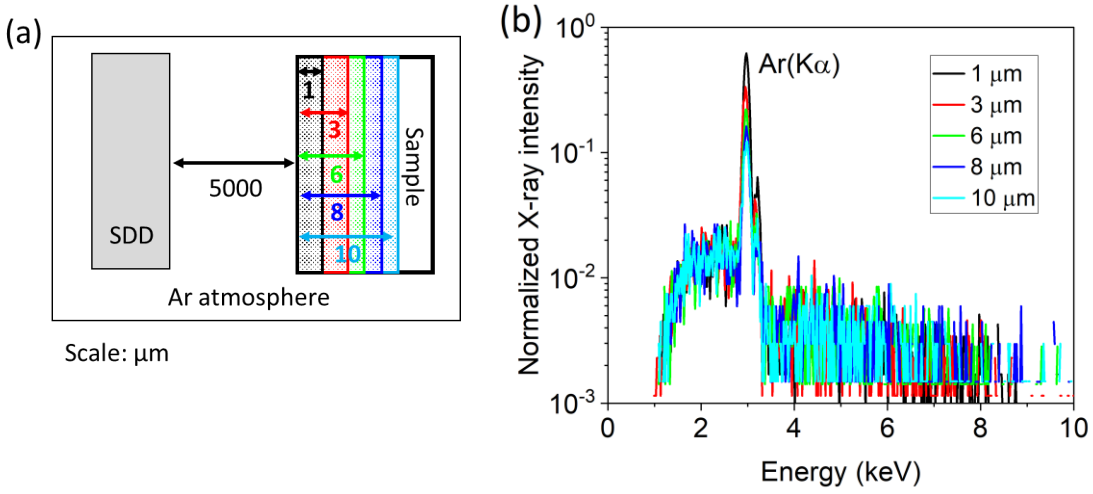


Fig. 4.4. (a) Schematic drawing of T retention profile constructed in Geant4 geometry and (b) X-ray spectra obtained from Geant4. In the simulation, uniform T retention up to depths of 1 μm (black), 3 μm (red), 6 μm (green), 8 μm (blue) and 10 μm (light blue) was assumed.

X-ray intensity increased as the T penetration depth decreased.

The X-ray spectra obtained by Geant4 under several different condition was compared to experimentally obtained BIXS spectrum. Fig. 4.5 is comparison between measured BIXS spectrum of ILW3 OPL center specimen (black) and Geant4 spectrum (red). In the simulation, T was uniformly distributed from surface to 6 μm depth described with green color in Fig. 4.4. The Geant4 spectrum showed the best agreement at this penetration depth to the experimental spectrum. The range of 1.01

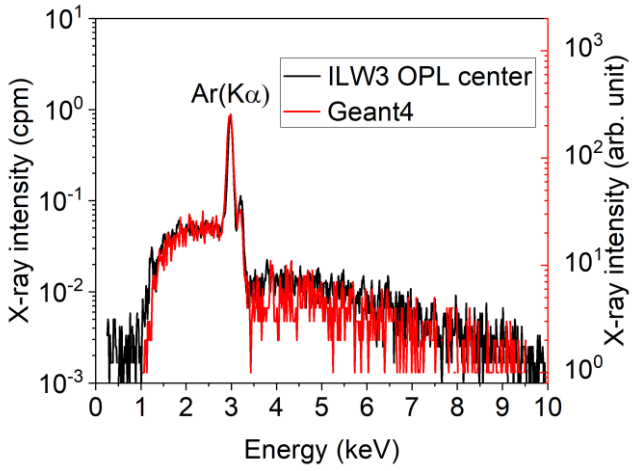


Fig. 4.5. Comparison of measured BIXS X-ray spectrum obtained from ILW3 OPL center specimen (black) and Geant4 simulation (red). T was assumed to be uniformly distributed from the surface up to 6 μm.

MeV T ions in Be is ~ 10 μm at normal incidence according to SRIM code [4]. The range of high energy tritons calculated from SRIM code is comparable to retention depth of T acquired from Geant4. It suggested that the dominant T retention mechanism in the eroded area of OPL is implantation of 1.01 MeV T ions. In the same manner, the retention depths in ILW1 and ILW1-3 OPL center and off-center specimens were also evaluated to be ~ 6 μm. It can be concluded that T retention mechanism for eroded areas of OPL specimens is the same regardless of ILW campaign: implantation of high energy T ions.

## 4.2. Surfaces in the castellation grooves

Typical image of castellation side is shown in Fig. 3.4 (b). The color change from grey to black was observed from the groove entrance to up to 3 mm depth. The color change of the surfaces by deposit formation was found in all four sides of the specimens. The black region was studied by ion beam analysis (IBA) [5] and it determined formation of D containing deposition layer on the castellation sides.

As shown in Fig. 3.4 (b), there were three gradients in color change of the castellation sides.

(1) top region (from entrance to 0.5 mm distance pointed in green) with silver to light grey.

(2) middle region (0.5 mm – 3 mm depth pointed in red) with black or dark grey.

(3) bottom region (> 3 mm pointed in yellow) with light metallic grey.

In order to determine the difference of surface composition between these locations, the castellation

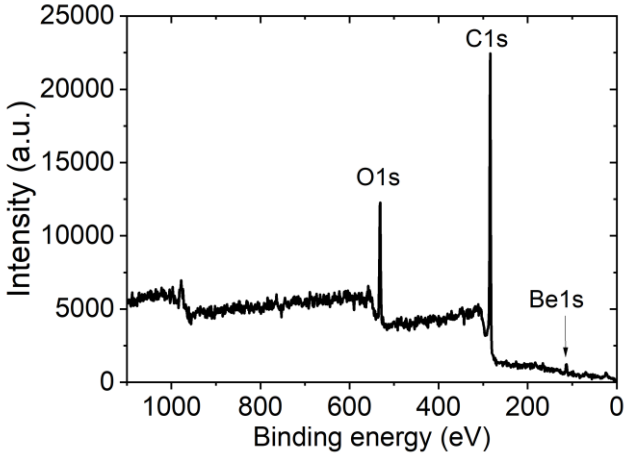


Fig. 4.6. XPS survey spectrum obtained at the entrance (0 – 0.5 mm distance from the entrance of castellation groove) of ILW1 127 specimen.

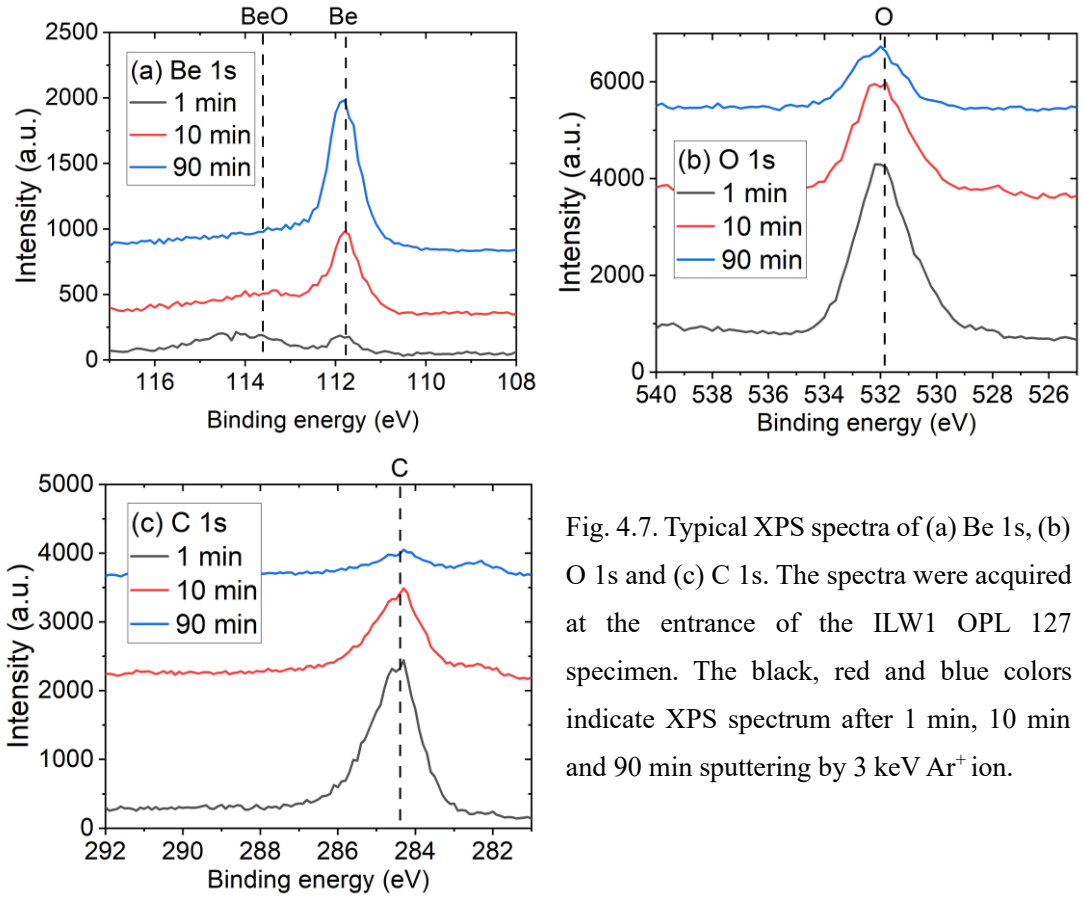


Fig. 4.7. Typical XPS spectra of (a) Be 1s, (b) O 1s and (c) C 1s. The spectra were acquired at the entrance of the ILW1 OPL 127 specimen. The black, red and blue colors indicate XPS spectrum after 1 min, 10 min and 90 min sputtering by 3 keV $Ar^+$ ion.

sides were analyzed with XPS.

The XPS survey spectrum obtained at the entrance of ILW1 127 castellation side is given in Fig. 4.6. The analyzed location is indicated with green dots in Fig. 3.4. On the very surface of the castellation side, signals of O and C were intense because of surface oxidation and contamination.

Fig. 4.7 is the typical high resolution XPS spectra of (a) Be 1s, (b) O 1s and (c) C 1s obtained at the groove entrance of ILW1 127 specimen. The black, red and blue color spectra indicate XPS spectrum after 1 min, 10 min and 90 min sputtering with 3 keV $Ar^+$ ion, respectively. In Fig. 4.7 (a), BeO peak was observed in short sputtering time. The BeO peak disappeared and the intensity of metallic Be peak increased as the sputtering time increased. It is a consequence of removal of the oxidized layer and exposure of Be substrate. For the same reason, the intensity of O peak in Fig. 4.7 (b) decreased as the sputtering progressed. The C1s spectra in Fig. 4.7 (c) showed that C impurities existed as legacy of JET-C were remained and deposited on the castellation sides.

For the quantitative analyses, the concentration of each element was calculated in the following order. The procedures for the spectra after 1 min sputtering are given as example.

1. The peak area of each element was evaluated by integrating signal intensity in a selected energy

region: 110 – 116 eV for Be, 529 – 534 eV for O and 283 – 286 eV for C.

2. Then, the peak area thus evaluated was divided by the atomic sensitivity factor to compensate the sensitivity difference between the elements.

3. The concentration of each element was acquired from the ratio of compensated peak intensity.

Fig. 4.8 shows depth profile of constituent elements of depositions formed at the top of castellation side of (a) ILW1 OPL 127 and (b) ILW3 OPL 560. The analyzed positions are shown in green dots of Fig. 3.4. The deposition layers were dominantly composed of Be, O and C and small amount of N with metal impurities such as W, Ni, Al and Cu.

W was JET-ILW divertor materials which is eroded by the PWIs and found in the main chamber. Ni was applied as a marker layer for erosion study and observed in the XPS spectra. Al was induced during maintenance period as a contaminant and Cu came from the neutral beam duct. During ILW operation, N seeded plasma was used for experiments. In two days at the end of ILW3, 35 pulses of discharge were performed with $^{15}N_2$ seeding. In the case of ILW1, just three pulses with $^{15}N_2$ marker gas were held in the last two weeks. Therefore, concentration of N was high in the ILW3 specimen. The components of deposition layers were different from side to side even in a single specimen. No clear correlation between deposition components and orientation of the surface inside the tokamak was observed.

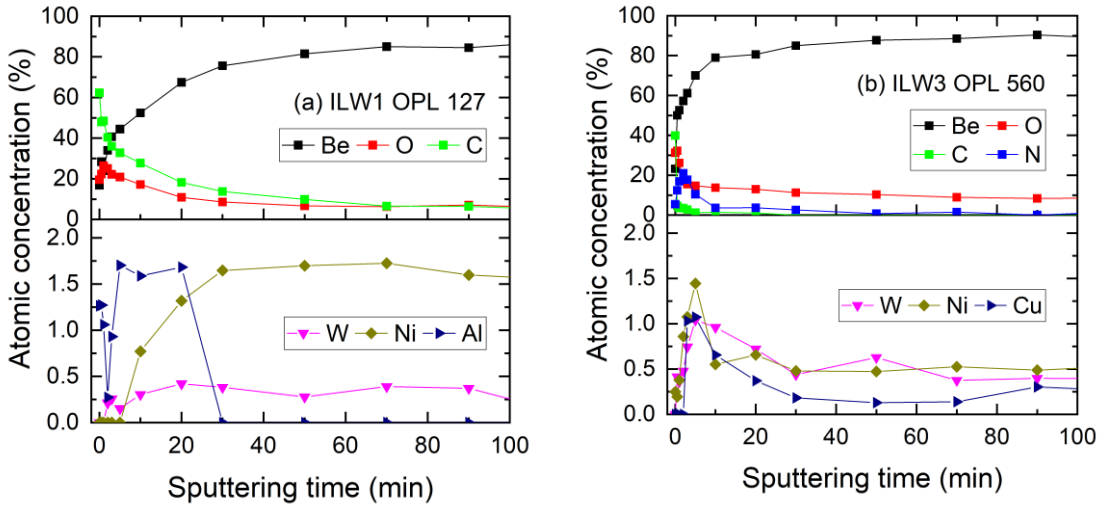


Fig. 4.8. Depth profiles of elements in deposition layers formed at the entrances of castellation sides of (a) ILW1 OPL 127 and (b) ILW3 OPL 560.

The depth profiles of constituent elements of deposits formed on the middle parts of OPL specimens were plotted in Fig. 4.9. The profiles were acquired from ILW1 OPL 127 (a), ILW3 OPL 560 (b) and ILW1-3 OPL 718 (c), and the analysis was performed at the positions indicated by the red dots in Fig. 3.4. The deposition layers were mainly composed of Be, O and C, and the concentration of metals was less than 1 %. The concentration ratio of Be to O, [Be]/[O], in the deposits was almost unity and it implied that BeO layers were formed on the middle parts of the castellation sides. However, thickness of the deposit layer was different from specimen to specimen. The thickness of BeO layer was thinner in ILW1 specimen than the others and it was due to shorter operation time and smaller amount of input energy of ILW1 than ILW3.

The sputtering depth on the castellation side was difficult to be measured due to initial surface roughness. Therefore, sputtering yield of BeO by 3 keV $Ar^+$ ions at the incident angle of 33 ° was calculated by Professor A. Ito of National Institute for Fusion Science [6]. He performed binary collusion approximation (BCA) simulation with BDoG code [7] under assumption that the BeO layer had wurtzite crystal structure and surface plane was (0001). Binding energy of Be and O was set to be

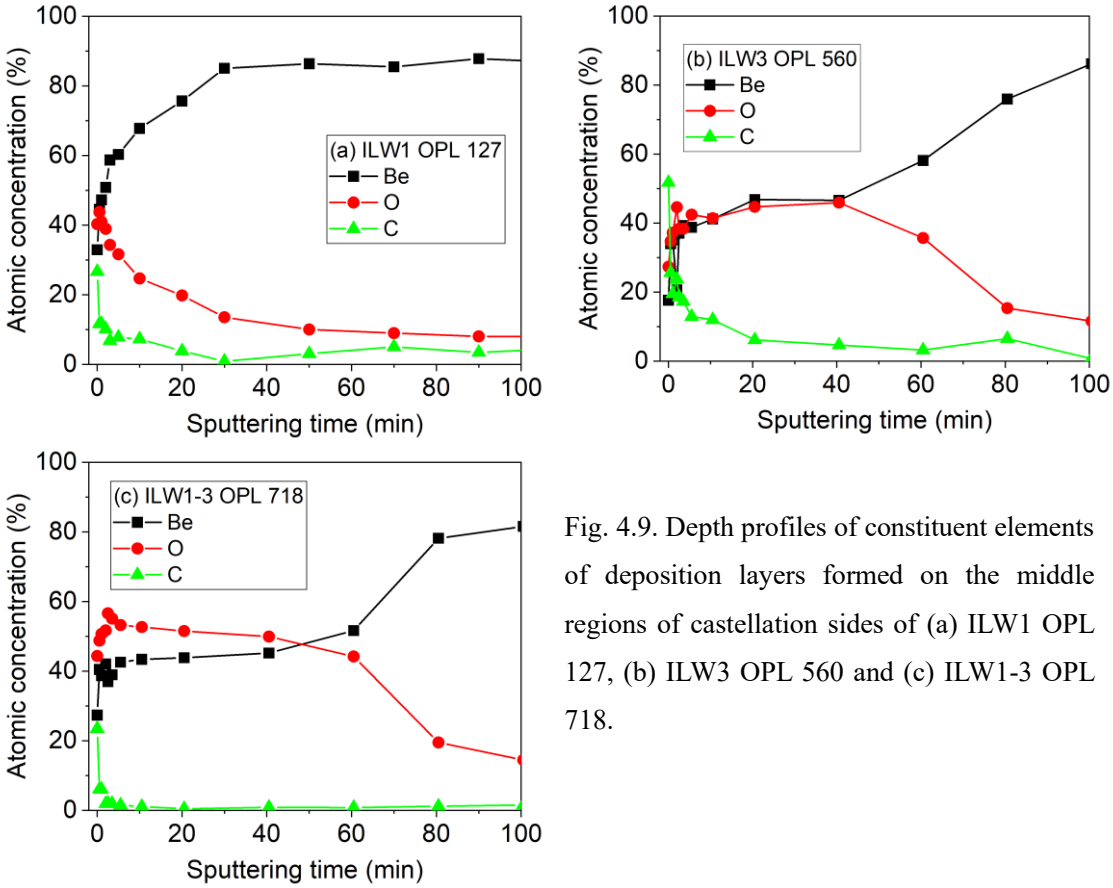


Fig. 4.9. Depth profiles of constituent elements of deposition layers formed on the middle regions of castellation sides of (a) ILW1 OPL 127, (b) ILW3 OPL 560 and (c) ILW1-3 OPL 718.

6.280 eV/atom. Density functional theory (DFT) was used to estimate cohesive energy of BeO. The sputtering yield obtained from BCA simulation was 5 atoms/ion.

The current density of 3 keV $Ar^+$ ion was 83.6 nA/mm$^2$. Therefore, the flux of irradiated $Ar^+$ ions per unit time and area was

$$83.6\ \text{nA/mm}^2 / 1.6\times10^{-19}\ \text{C} = 5.2\times10^{11}\ \text{ions/s}\cdot\text{mm}^2 . \quad (4.1)$$

The amount of sputtered atoms per unit are and unit time was

$$5.2\times10^{11}\ \text{ions/s}\cdot\text{mm}^2 \times 5\ \text{atoms/ion} = 2.6\times10^{12}\ \text{atoms/s}\cdot\text{mm}^2 = 1.6\times10^{14}\ \text{atoms/min}\cdot\text{mm}^2 . \quad (4.2)$$

After 80 minutes sputtering,

$$1.6\times10^{14}\ \text{atoms/min}\cdot\text{mm}^2 \times 80\ \text{min} = 1.2\times10^{16}\ \text{atoms/mm}^2 \quad (4.3)$$

were sputtered. When assuming that deposition layer is BeO with density of 3.02 g/cm$^3$ and molar mass of 25 g/mol, the amount of sputtered BeO is calculated to be

$$1.2\times10^{16}\ \text{atoms/mm}^2 / 2 = 6\times10^{15}\ \text{BeO/mm}^2 . \quad (4.4)$$

This amount of BeO corresponds to the layer thickness of

$$6\times10^{15}\ \text{BeO/mm}^2 / 7.3\times10^{19}\ \text{BeO/mm}^3 = 8.6\times10^{-5}\ \text{mm} . \quad (4.5)$$

Namely, the thickness of deposition layers was evaluated to be ~ 86 nm at the sputtering time of 80 min. The depth profiles are still given as a function of sputtering time in the following figures because the sputtering rate varies with the composition of deposition layers and the depth was small compared to the surface roughness.

The depth profiles of elements composing deposition layer formed at the bottom region of castellation sides were shown in Fig. 4.10 for (a) ILW1 OPL 127 and (b) ILW3 OPL 560 specimens. The measurements were conducted in the location indicated in yellow dots of Fig. 3.4. The constituent elements were similar to those of the middle region, i.e., Be, O and C. However, the deposition layers at the bottom regions were thinner than those formed on the middle region (Fig. 4.9). The difference in deposition layer thickness was insignificant between ILW1 and ILW3 specimens. However, C concentration was higher in ILW1 specimen than ILW3 specimen.

The color change generated by deposition was insignificant in DP specimens and it was almost

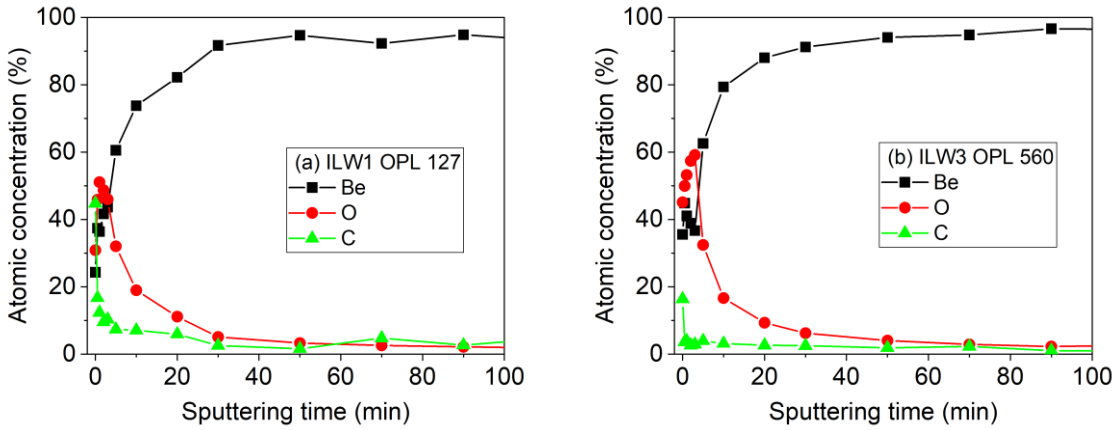


Fig. 4.10. Depth profiles of constituent elements of deposition layer formed at the bottom regions of castellation sides of (a) ILW1 OPL 127 and (b) ILW3 OPL 560.

invisible in ILW3 specimen. Fig. 4.11 is depth profile of constituent elements at the bottom region of (a) ILW1 DP 78 and (b) ILW3 DP 447. The deposition was comprised of Be, O, C and compositions of DP specimens were similar to those of OPL specimens. The concentration of C in the deposition formed on the ILW1 specimen was higher than that on ILW3 specimen, as observed in OPL specimen.

The T distributions on four sides of each specimen were examined by IP technique. During the IP measurement of the castellation sides, the PFS was masked because β-rays emitted from T in the PFS was scattered by air and interfered the signals from the castellation sides.

IP images of IWGL 36 and OPL 127 specimens are given in Fig. 4.12 as typical examples. T enriched regions corresponded to the regions where deposition layers were formed. The PSL intensity in the top regions of a single specimen was different from plane to plane. In OPL 127 specimen, the

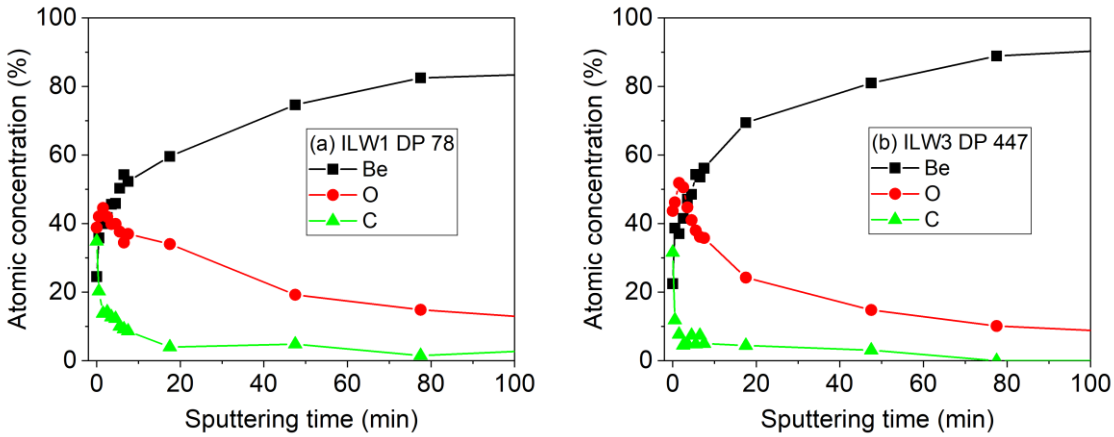


Fig. 4.11. Depth profiles of constituent elements at the bottom regions of castellation sides of (a) ILW1 DP 78 and (b) ILW3 DP 447.

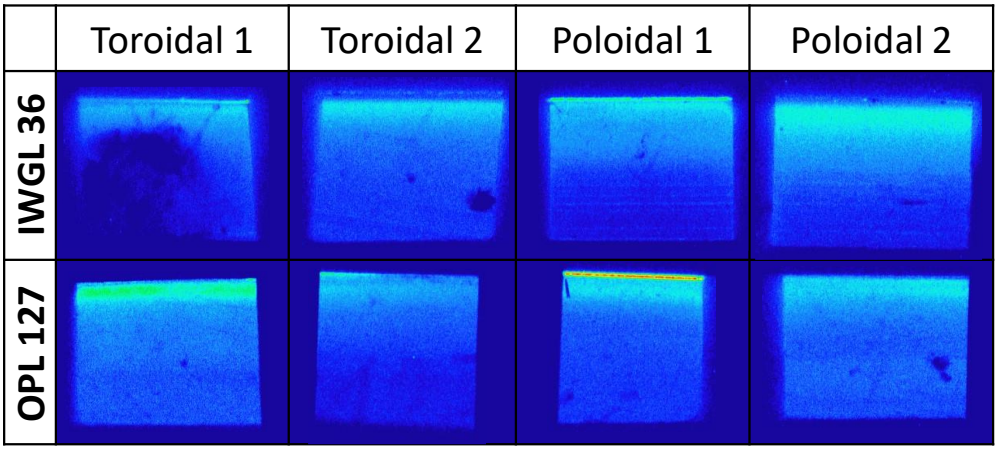


Fig. 4.12. All four castellation sides IP images of IWGL 36 and OPL 127 specimens.

PSL intensity at the top region of poloidal 1 surface was higher than other castellation sides by an order of magnitude. However, there was no clear correlation between T enrichment and deposition composition or surface orientation (toroidal or poloidal) inside the tokamak. On the other hand, such high PSL intensity at the top region was not observed in the case of IWGL 36 specimen. The PSL intensity in the middle and bottom regions was comparable for all castellation sides.

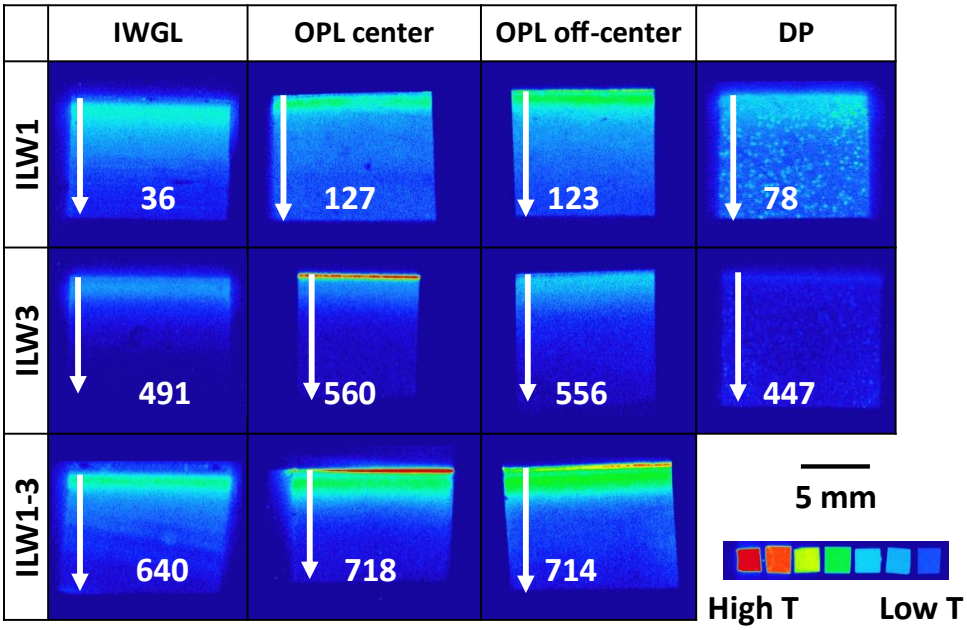


Fig. 4.13. Typical IP images of castellation sides after each campaign. Regions with high and low T concentrations are shown in red and blue colors, respectively. The white numbers are identification numbers of specimens.

The IP results for the castellation sides of ILW1, ILW3 and ILW1-3 specimens are given in Fig. 4.13. The white numbers in Fig. 4.13 are identification numbers of the specimens. As mentioned above, T was depleted at the top regions of IWGL specimens, and the PSL intensity was high at the middle region followed by a gradual decrease in PSL intensity with increasing depth. In OPL specimens, T was enriched at the top of some sides of OPL specimens, as indicated by red color for specimens 560, 718 and 714 in Fig. 4.13. The castellation sides without T enrichment showed similar T distribution with IWGL.

In addition to high PSL intensity in the middle region, irregular pattern of relatively high PSL intensity was detected at the bottom region of ILW1 DP specimen. The PSL intensity of ILW3 DP specimen was weaker than that of ILW1 DP specimen but PSL distribution was similar between ILW1 DP and ILW3 DP.

Fig. 4.14 shows IP image of ILW3 OPL 560 specimen after sputtering with $Ar^+$ ion. In the sputtered region indicated with the red dashed circle, the PSL intensity was lower than the non-sputtered region by a factor of 4. The decrease in PSL intensity by sputtering implied that T was accumulated in the deposition layer.

The PSL intensity profiles from the groove entrance to the bottom of castellation side, along white arrows in Fig. 4.13 were evaluated from the ratio between PSL intensity of the Be specimens and that of the standard sample with the highest T concentration. The evaluated T distribution profiles are shown in Fig. 4.15.

All castellation sides of IWGL and OPL had one of two types of distribution profiles regardless of tile location: (i) a broad T retention peak in middle region followed by reduction of PSL intensity with increasing distance from the entrance or (ii) high T retention peak in the top region (< 0.5 mm) and

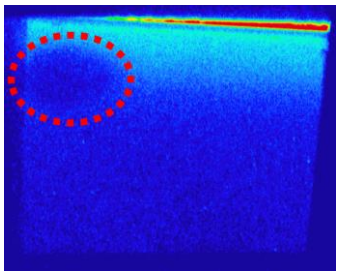

Fig. 4.14. IP image of ILW3 OPL 560 specimen after sputtering of deposition layer. The sputtered region is indicated in red dashed circle.

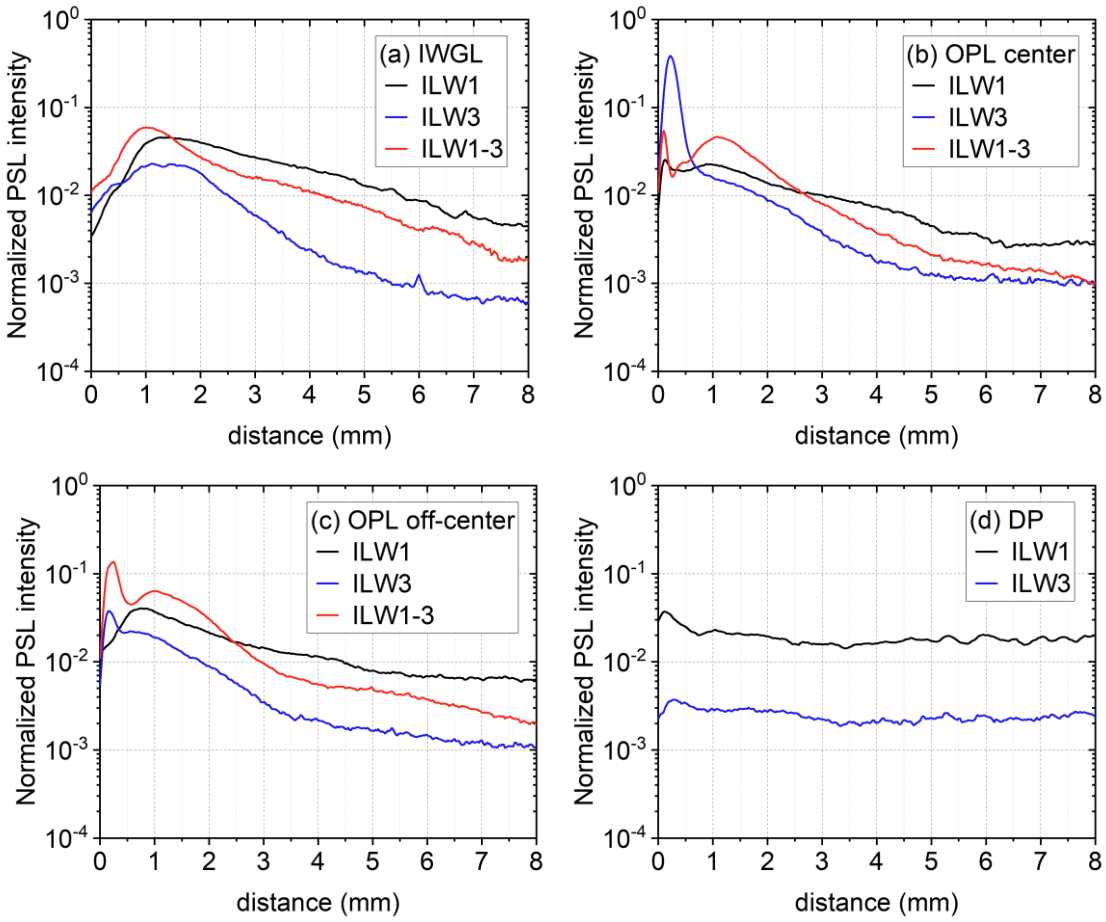


Fig. 4.15. Normalized PSL intensity profiles of (a) IWGL specimen, (b) OPL center specimen, (c) OPL off-center specimen and (d) DP specimen after each campaign.

additional broad peak in the middle region at ~ 1.5 mm distance.

The characteristics of PSL profiles of IWGL and OPL specimens can be summarized as follows.

(1) Top region (from entrance to 0.5 mm distance): PSL intensity was different by an order of magnitude from surface to surface.

(2) Middle region (0.5 mm – 3 mm depth): PSL intensity was comparable regardless of specimen location.

(3) Bottom (> 3 mm): PSL intensity was higher in ILW1 specimens than ILW3 and ILW1-3 specimens.

The T concentration was comparable in the middle region regardless of tile location and ILW campaign. Also, the profile of T concentration was similar to that of D reported previously [5]. These observations suggested similar retention mechanisms of T and D in the castellation sides: T was co-deposited on the castellation sides together with D, Be, O and C, after thermalization in the plasma.

At the bottom, PSL intensity was high in the specimens used in ILW1 regardless of location in the tokamak. This is a consequence of high C impurities inside JET-ILW tokamak during ILW1 campaign, after the end of JET-C operation [8]. Indeed, the high C concentration was observed at the bottom regions in Figs. 4.10 and 4.11. It is plausible that T was transferred to the bottom regions as hydrocarbons.

The T distributions on DP specimens were different from those on IWGL and OPL specimens. The T concentration on DP specimens was uniform from the top to bottom. In addition, irregular patterns with high PSL intensity regions were observed on the castellation sides. The unique T retention profile on DP specimens is influence of cycling of high heat flux to the DPs and consequent repetition of thermal desorption of T and co-deposition.

## 4.3. T inventory in the JET-ILW main chamber

T retention on PFS and castellation sides of Be limiter tiles were calculated according to PSL intensity from IP results and T retention depth. For PFS, Geant4 simulation result in Fig. 4.5 determined that T was distributed up to 6 μm depth. In the case of the castellation sides, 85 nm which was calculated as the thickness of deposition layer by BCA simulation was set to be T retention depth at the middle region.

As discussed in subsection 3.2.1, PSL intensity is proportional to T radioactivity. The radioactivity of the piece in standard sample with highest radioactivity was $2.8\times10^8$ Bq/cm$^3$ in the calibration day, 2014 July 12th. As an example, the procedure of evaluation of T retention on the PFS of ILW3 OPL 556 specimen is given in the following.

1. The IP measurement of ILW3 OPL 556 specimen was carried out in 2019 November 26th. The date difference between calibration day and measurement day is 1963 days. Therefore, the T concentration in the T standard piece was

$$N(1963\text{ days}) = 2.8\times10^8\text{ Bq/cm}^3 \times\left(\frac{1}{2}\right)^{\frac{1963\text{ days}}{4490\text{ days}}} = 2\times10^8\text{ Bq/cm}^3\,, \tag{4.6}$$

in the measurement day according to Eq. (1.5).

2. The PSL intensity of the standard piece and the specimen surface was 2792.7 PSL/mm$^2$ and 1145.95 PSL/mm$^2$, respectively. As discussed in section 2.1, the escape depth of β-rays is inversely proportional to density of the T containing materials. Therefore, density of the standard (1.0 g/cm$^3$)

and Be (1.85 g/cm$^3$) were considered. The T concentration of the specimen was calculated as

$$\frac{1145.95\ \text{PSL/mm}^2 \times\ 1.85\ \text{g/cm}^3}{2792.7\ \text{PSL/mm}^2 \times 1\ \text{g/cm}^3} \times 2\times10^8\ \text{Bq/cm}^3\ = 1.5\times10^8\ \text{Bq/cm}^3\,. \tag{4.7}$$

3. The calculated value is the T concentration in the measurement day. For more accurate evaluation, the T concentration in the day of tile extraction from the tokamak was calculated by considering radioactive decay. The ILW3 campaign was carried out from 2015 and 2016 and it was assumed that the ILW3 campaign was finished in 2016 September 1st. The measurement was conducted after 1180 days of the tile extraction. As a result, T concentration of the specimen in the day of tile retrieval was

$$\frac{1.5\times10^8\ \text{Bq/cm}^3}{0.5^{\frac{1180\ \text{days}}{4490\ \text{days}}}} = 1.8\times10^8\ \text{Bq/cm}^3\,. \tag{4.8}$$

4. T retention was calculated by considering 6 μm T retention depth.

$$1.8\times10^8\ \text{Bq/cm}^3\times\ 6\times10^{-4}\ \text{cm} = 1.1\times10^5\ \text{Bq/cm}^2\,. \tag{4.9}$$

The T retention in PFSs of other specimens was also calculated in the same manner.

For the castellation sides, T retention depth was 85 nm or less. Therefore, attenuation of β-rays in the deposition layers was ignored while that in the plastic piece was considered. According to Eq. (2.1), the range of 18.6 keV T β-rays is 0.000586 cm$^{-1}$ in plastic with density of 1 g/cm$^3$. The absorption coefficient is

$$\mu = -\ln(1/2)/0.1R_m\,, \tag{4.10}$$

where $R_m$ is the range of β-rays [9]. Fig. 4.16 shows intensity of T β-rays as a function of thickness of the plastic film which is uniformly labelled with T. The figure indicated that intensity of β-rays escaped from the film reached maximum at the thickness of 4 μm because the escape probability of β-rays is negligible at the deeper region. Fig. 4.16 indicates that β-rays intensity from the standard sample is higher by a factor of 11 than that from a matter with the same T concentration with the thickness of 85 nm and negligible attenuation of β-rays. The T retention in the middle region was calculated using this factor. Then, the retention in the other regions was evaluated from the ratio of PSL intensity between these regions and the middle region.

Fig. 4.17 shows that PFSs had different T retention according to the tile location. The T retention was highest in OPL and it increased as ILW campaign progressed because the largest amount of T was produced in ILW3. In the case of IWGL and DP, T retention was similar after each campaign. PFSs of

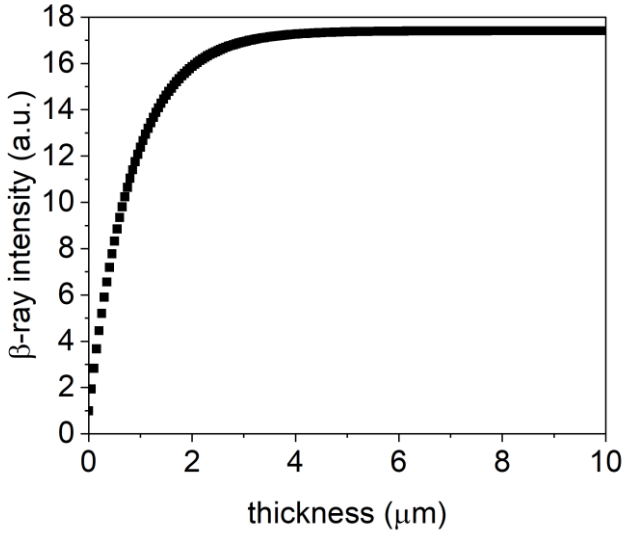


Fig. 4.16. Intensity of β-rays in 1.0 g/cm$^3$ plastic according to the thickness of the plastic. Tritium is uniformly distributed in the plastic sample.

OPL contained larger amount of T than IWGL and DP by an order of magnitude while D retention in all three tiles were similar in an order of $10^{18}$ atoms/cm$^2$ [1 – 3].

The retention of T was higher in OPL than IWGL or DP. The temperature of DP exceeded melting point of Be (1287 °C) and PFS of DP was partly melted [10]. Guillemaut at al. [11] measured heat loads to the main chamber by using thermocouples installed in the main chamber walls. According to Fig. 8 given in [11], the plasma heat load to the IWGL was higher than OPL by a factor of 2. The temperature of IWGL PFS was measured with IR thermography and maximum temperature was 500 °C [12]. As the heat load to OPL is lower than that to IWGL [11], the temperature of OPL PFS should be lower than that of IWGL. The maximum release rate of D from JET-ILW Be limiter tile was observed in the temperature range from 450 – 600 °C [13]. Therefore, the amount of desorbed T was smallest in OPL due to low tile temperature.

The erosion of the limiter tiles was also analyzed after retrieving tiles from the JET-ILW [2, 14 – 17]. The net erosion was observed at the center of the mid-plane IWGL and OPL [2, 14, 15]. IWGL is contacted to plasma during limiter configuration [18, 19]. Post-mortem analyses with profilometry presented that center of mid-plane OPL and IWGL was eroded 10 μm and 60 μm, respectively [15]. When uniform erosion-deposition pattern is assumed, the net Be erosion in OPL is ~ 5 g and that in IWGL is ~ 8 g [15]. The amount of materials eroded from IWGL was also larger than that from OPL in JET-C 2008-2009 campaign [22, 23]. Due to the influence of high tile temperature and severe

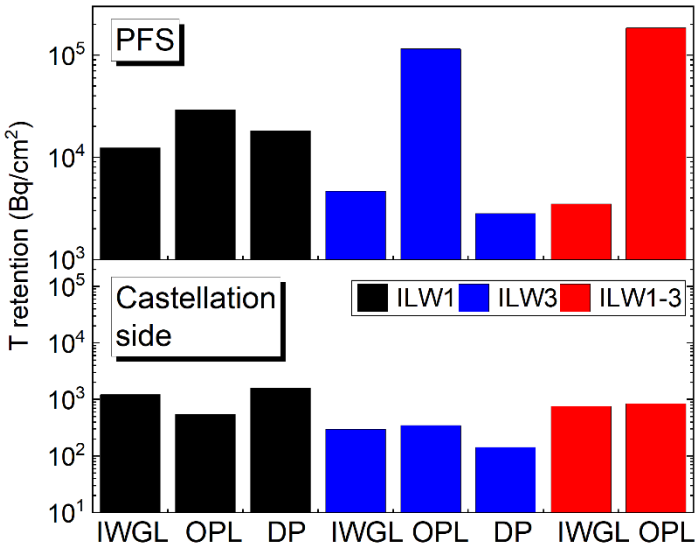


Fig. 4.17. T retention in PFSs and castellation sides of Be limiter tiles used in JET-ILW.

erosion in IWGL than OPL, more T was removed from the IWGL and T retention was highest in OPL.

T was accumulated to PFSs of Be limiters by implantation via prompt loss and part of T was removed from the tile by thermal desorption due to heat load from the plasma and/or by erosion of the tile surface. Therefore, T retention in the PFSs is determined by the balance between implanted T and T removed by thermal desorption and/or erosion.

In Fig. 4.17, the castellation sides presented different T accumulation pattern to PFSs. The T retention in the castellation sides was similar in all three tiles after each campaign. The castellation sides of ILW3 specimens contained the smallest amount of T. The result up to here denoted that the dominant T retention mechanism in the castellation sides is co-deposition of thermalized T with eroded wall materials and impurities, and the concentration of T in the deposition layers increased with increasing the C concentration in the deposited layers [24, 25]. As a consequence of gradual decreasing of C impurities in JET plasma from campaign to campaign [8], the T retention in the castellation sides of ILW3 specimens in Figs. 4.13, 4.15 and 4.17 was smaller than that in ILW1 and ILW1-3 specimens.

The total T inventory in Be limiter tiles was calculated by multiplying surface area by T retention, and the result is shown in Fig. 4.18. The PFS area of IWGL, OPL and DP was 4.75 m$^2$, 10.08 m$^2$ and 6.05 m$^2$, respectively [5]. Total 43000 number of castellation blocks were in IWGL, 50013 in OPL and 40448 in DP [5]. The nominal area of a single castellation side is 12 mm × 12 mm. A single castellation specimen has 4 sides. Therefore, the areas of castellation sides were

IWGL: 12×12 $mm^2$ /side × 4 sides/block × 43000 blocks = 25 $m^2$ , (4.11)

OPL: 12×12 $mm^2$ /side × 4 sides/block × 50013 blocks = 29 $m^2$ , and (4.12)

DP: 12×12 $mm^2$ /side × 4 sides/block × 40448 blocks = 23 $m^2$ . (4.13)

In the case of ILW1-3, the T inventory of DP tiles was not considered because the specimens were not available. ILW1 tiles contained the smallest amount of T, and T inventory increased with the progress of campaigns because the amount of produced T was largest in ILW3. The PFS of OPL was the main T reservoir in limiter tiles in all campaigns. The ratio of T in castellation sides to total T in the main chamber limiter was less than 20 % even in ILW1 in which the contribution of castellation side was the largest. This tendency of T accumulation is different to that of D; the amount of D retained in the castellation sides accounted for 50 % of total D in the main chamber [5, 26]. The difference in distribution of T and D was caused by implantation of 1.01 MeV T into PFS.

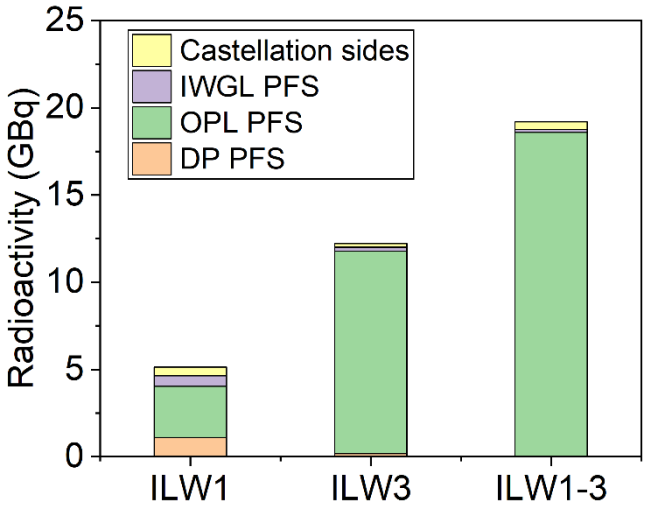


Fig. 4.18. T inventory for Be limiter tiles in JET-ILW main chamber.

## 4.4. Summary

The T retention in JET-ILW Be limiter tiles was evaluated and the underlying mechanisms were discussed in this chapter. The dominant T retention mechanisms for PFSs and castellation sides were different from each other.

The high energy T ions which are products of DD fusion reactions directly implanted to the PFSs. The PFSs of OPL contained larger amount of T than that of IWGL and DP due to less erosion of tile and less thermal desorption of T. The T inventory was higher in ILW3 tiles than ILW1 tiles because more T was produced in the ILW3 campaign.

On the other hand, thermalized T was co-deposited on the castellation sides with Be, O and C. Accumulation of T on the castellation sides was not influenced by the location of tiles but sensitively dependent on the impurity content. Indeed, C concentration of the deposition layers formed on the castellation sides was a decisive factor of T enrichment in the deposition layers. As a result, T retention in the Be limiter tiles was similar after each campaign regardless of limiter location while the tiles used in ILW3 campaign contained the smallest amount of T because C impurities inside the JET-ILW tokamak reduced as the ILW campaign continued.

References


[1] K. Heinola et al., Fuel retention in JET ITER-Like Wall from post-mortem analysis, J. Nucl. Mater 463 (2015) 961-965, https://doi.org/10.1016/j.jnucmat.2014.12.098

[2] A. Widdowson et al., Fuel inventory and material migration of JET main chamber plasma facing components compared over three operational periods, Phys. Scr. T171 (2020) 014051, https://doi.org/10.1088/1402-4896/ab5350

[3] A. Widdowson et al., Overview of fuel inventory in JET with the ITER-like wall, Nucl. Fusion 57 (2017) 086045, https://doi.org/10.1088/1741-4326/aa7475

[4] J. F. Ziegler, http://www.srim.org/

[5] M. Rubel et al., Fuel inventory and deposition in castellated structures in JET-ILW, Nucl. Fusion 57 (2017) 066027, https://doi.org/10.1088/1741-4326/aa6864

[6] A. M. Ito, private communication

[7] A. M. Ito et al., Triple hybrid simulation method for tungsten fuzzy nanostructure formation, Plasma Fusion Res. 13 (2018) 3404061, https://doi.org/10.1585/pfr.13.3403061

[8] S. Krat et al., Comparison of erosion and deposition in JET divertor during the first three ITER-like wall campaigns, Phys. Scr. T171 (2020) 014059, https://doi.org/10.1088/1402-4896/ab5c11

[9] J. P. Laurent, G. Lapasset et al., High resolution electron-microautoradiography applied to metallurgy, Intern. J. Appl. Radiation Isotopes 24 (1973) 213, https://doi.org/10.1016/0020-708X(73)90044-6

[10] I. Jepu et al., Beryllium melting and erosion on the upper dump plates in JET during three ILW campaigns, Nucl. Fusion 59 (2019) 086009, https://doi.org/10.1088/1741-4326/ab2076

[11] C. Guillemaut et al., Main chamber wall plasma loads in JET-ITER-like wall at high radiated fraction, Nucl. Mater. Energy 12 (2017) 234-240, https://doi.org/10.1016/j.nme.2017.02.010

[12] S. Brezinsek et al., Study of physical and chemical assisted physical sputtering of beryllium in the JET ITER-like wall, Nucl. Fusion, 54 (2014) 103001, https://doi.org/10.1088/0029-5515/54/10/103001

[13] A. Baron-Wiechec et al., Thermal desorption spectrometry of beryllium plasma facing tiles exposed in the JET tokamak, Fusion. Eng. Des., 133 (2018) 135-141, https://doi.org/10.1016/j.fusengdes.2018.05.075

[14] A. Widdowson et al., Material migration patterns and overview of first surface analysis of the JET ITER-like wall, Phys. Scr. T159 (2014) 014010, https://doi.org/10.1088/0031-8949/2014/T159/014010

[15] A. Baron-Wiechec et al., Global erosion and deposition patterns in JET with the ITER-like wall, J. Nucl. Mater. 463 (2015) 157-161, https://doi.org/10.1016/j.jnucmat.2015.01.038

[16] M. Mayer et al., Erosion and deposition in the JET divertor during the first ILW campaign, Phys. Scr. T167 (2016) 014051, https://doi.org/10.1088/0031-8949/T167/1/014051

[17] S. Krat et al., Comparison of JET inner wall erosion in the first three ITER-like wall campaigns, Nucl. Mater. Energy 29 (2021) 101072, https://doi.org/10.1016/j.nme.2021.101072

[18] K. Heinola et al., Experience on divertor fuel retention after two ITER-Like Wall campaigns, Phys. Scr. T170 (2017) 014063, https://doi.org/10.1088/1402-4896/aa9283

[19] J. Romazanova et al., Beryllium global erosion and deposition at JET-ILW simulated with ERO2.0, Nucl. Mater. Energy 18 (2019) 331-338, https://doi.org/10.1016/j.nme.2019.01.015

[20] S. Brezinsek, JET-EFDA contributors, Plasma-surface interaction in the Be/W environment: Conclusions drawn from the JET-ILW for ITER. J. Nucl. Mater. 463 (2015) 11-21, https://doi.org/10.1016/j.jnucmat.2014.12.007

[21] F. Romenelli and JET EFDA contributors, Overview of the JET results with the ITER-like wall, Nucl. Fusion 53 (2013) 104002, https://doi.org/10.1088/0029-5515/53/10/104002

[22] G. F. Matthews et al., Plasma operation with an all metal first-wall: Comparison of an ITER-like wall with a carbon wall in JET, J. Nucl. Mater 438 (2013) S2-S10, https://doi.org/10.1016/j.jnucmat.2013.01.282

[23] A. Widdowson et al., Comparison of JET main chamber erosion with dust collected in the divertor, J. Nucl. Mater 438 (2013) S827-S832, https://doi.org/10.1016/j.jnucmat.2013.01.179

[24] M. Mayer et al., Erosion and deposition in the JET divertor during the second ITER-like wall campaign, Phys. Scr. T170 (2017) 014058, https://doi.org/10.1088/1402-4896/aa8ff9

[25] Y. Oya et al., Comparison of hydrogen isotope retention in divertor tiles of JET with the ITER-like wall following campaigns in 2011-2012 and 2015-2016, Fusion Sci. Technol. 76 (2020) 439-445, https://doi.org/10.1080/15361055.2020.1716455

[26] A. Widdowson et al., Evaluation of tritium retention in plasma facing components during JET tritium operations, Phys. Scr. 96 (2021) 124075, https://doi.org/10.1088/1402-4896/ac3b30

# Chapter 5. Tritium distribution in divertor region

## 5.1. W-coated carbon-fiber-composite (CFC) tiles

T distributions on W-coated CFC tiles were also analyzed with IP technique, as shown in Fig. 5.1. The measurements were conducted with β-ray sensitive IP (β-IP). The regions with high and low PSL intensity are colored in red and blue, respectively. The PSL intensity normalized with that of the standard sample with the highest T concentration is shown in Fig. 5.2.

In Fig. 5.1 and 5.2, the PSL intensity of ILW3 tiles are higher than that of ILW1 tiles, except 4-10, because large amount of T was produced during ILW3 as explained in Table 2. Also, the inboard divertor tiles showed higher PSL intensity than the outboard tiles.

The erosion and deposition on the PFSs of W-CFC divertor tile were evaluated together with the D retention in [1 – 6]. The deposition layers were composed of Be, C, O, W and D. The concentration was different according to the tile location: $10^{20}$ Be-atoms/cm$^2$, $2\times10^{19}$ C-atoms/cm$^2$, $10^{19}$ D-

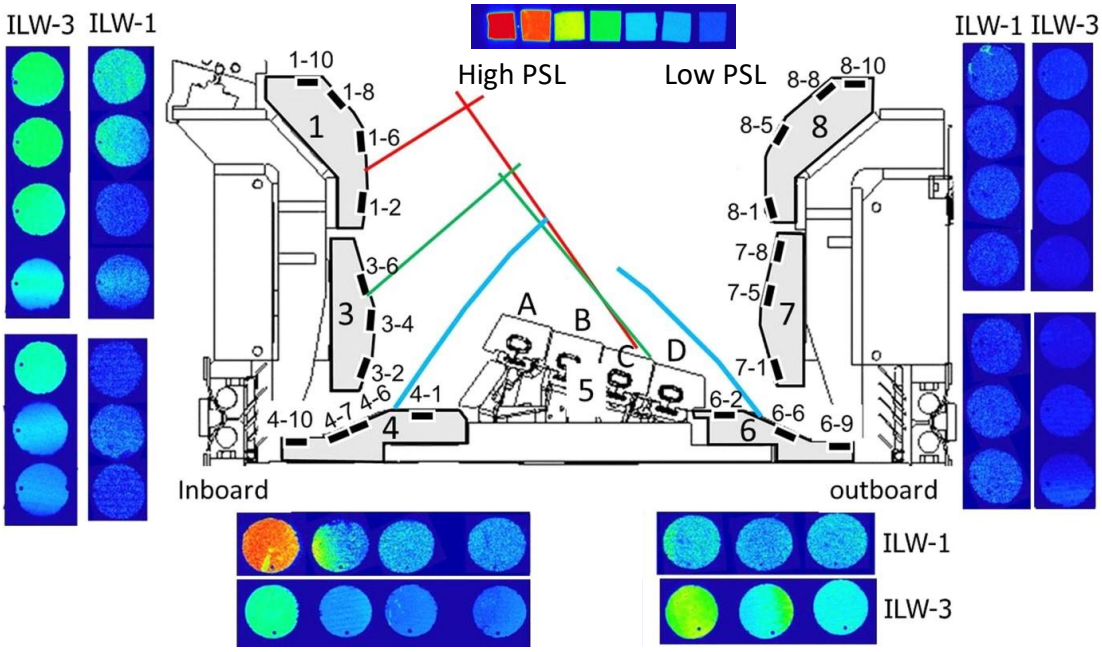


Fig. 5.1. 2-Dimensional T distribution on PFS of W-CFC tiles observed with β-ray sensitive IP. The region with high PSL is shown in red and low PSL intensity is colored in blue. The green and blue lines in the cross-section image are indicating strike points of ILW1 and ILW3, respectively.

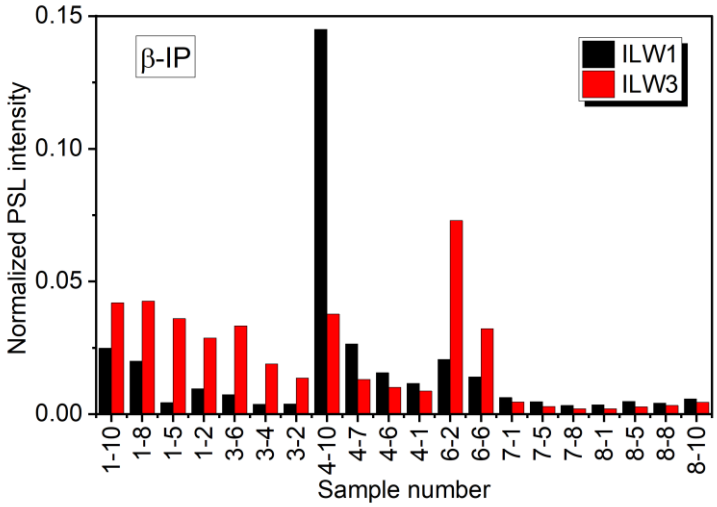


Fig. 5.2. PSL intensity of W-CFC samples acquired from β-ray sensitive IP.

atoms/cm$^2$ in Tile 1 and $3\times10^{18}$ Be-atoms/cm$^2$, $4\times10^{18}$ C-atoms/cm$^2$, $2\times10^{18}$ D-atoms/cm$^2$ in Tile 4 [4]. The thick deposition layers were formed on the inboard tiles, especially apron of Tile 1, and the region agreed to D enriched region [1 – 5]. Not only D but also T was concentrated in the PFSs of W-CFC tiles where deposition layer was formed [7 – 10]. These observations indicated that retention mechanism of T and D was similar in the divertor region and T was co-deposited on the PFSs of divertor tiles together with D and Be, C, O and W.

In the case of ILW1 tiles, PSL intensity was high in the apron of Tile 1 (1-10) and remote area of Tile 4 (4-10). The amount of accumulated T was large in sample 1-10 because 10 – 15 μm-thick deposit was formed on the apron of Tile 1 [3, 11]. PSL intensity was significantly high in 4-10 even though the deposit on the sample was ranged from 0 – 5 μm [4]. The surface composition of the sample was evaluated by XPS and C concentration of the deposition was 30 – 50 % in 4-10 while other regions showed concentration less than 10 %. [12]. The high T concentration in 4-10 was a result of high C concentration in the deposition layers.

Fig. 5.3 is the PSL intensity of W-CFC PFSs acquired from X-ray sensitive IP (X-IP). The PSL intensity was normalized by that of standard sample with highest T concentration. Compare to Fig. 5.2 obtained with β-IP, ILW3 tiles showed higher PSL intensity than ILW1 tiles. Also, the PSL intensity was more uniform in X-IP than β-IP: PSL intensity of outer divertor tiles and inner divertor tiles were similar. The escape depth of X-rays is longer than that of β-rays. Therefore, T retained beyond the detection depth of β-IP was able to be observed with X-IP. Thus, PSL intensity obtained from X-ray

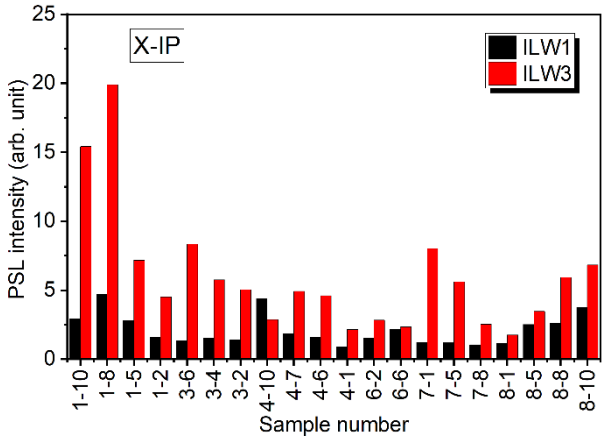


Fig. 5.3. PSL intensity of W-CFC samples acquired from X-ray sensitive IP.

sensitive IP indicates that T accumulated in the outer divertor tiles were mainly retained beyond escaped depth of T β-rays in W (~ 0.3 μm).

To examine T retention depth, X-ray spectrum of W-CFC samples was acquired with BIXS technique. Fig. 5.4 shows X-ray spectra from (a) ILW3 1-10, (b) ILW3 4-10 and (c) ILW3 8-10 as typical examples. The ILW3 sample 1-10 was cut from the apron of Tile 1 where thick deposition layer was formed [3, 11]. The ILW3 4-10 sample had thinner deposition layer, and ILW3 8-10 sample was taken from the erosion zone.

The spectrum in Fig. 5.4 (a) (ILW3 1-10 sample) showed the intense Ar(Kα) peak and strong bremsstrahlung at 2-8 keV when compared with (b) and (c) in the same figure. It should be noted that the characteristic X-rays from Be (108.5 eV) are totally attenuated by the detector window and not detectable, as mentioned in subsection 3.2.2. The Ar(Kα) X-rays are generated by β-rays from T within the escape depth of β-rays. The relatively intense Ar(Kα) peak can be explained to the larger escape depth of T β-rays in the Be deposition layer than that it W due to lower density of the former. Despite the efficiency of bremsstrahlung generation increases with increasing atomic number, the intensity of bremsstrahlung from the sample 1-10 was higher than that from the sample 8-10 from the erosion zone where T is retained in W. This difference indicates that T concentration in the Be deposition layer was far higher than that in W layer on the sample 8-10. These observations are well consistent with the IP results described earlier. The presence of Ni(Kα) X-ray showed that deposition layer contained Ni.

Fig. 5.4 (b) showed weaker bremsstrahlung than (a). This was due to smaller thickness of Be deposition layer.

Fig. 5.4. (c) showed relatively intense W(Lα) peak compared with Fig. 5.4 (a) and (c). As shown in

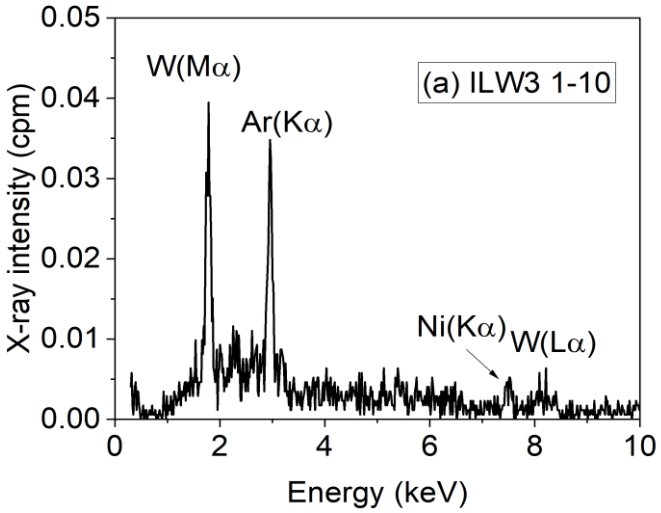


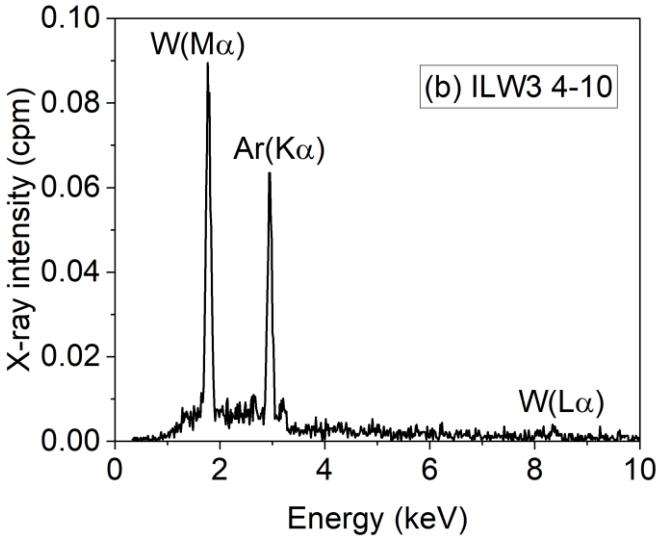


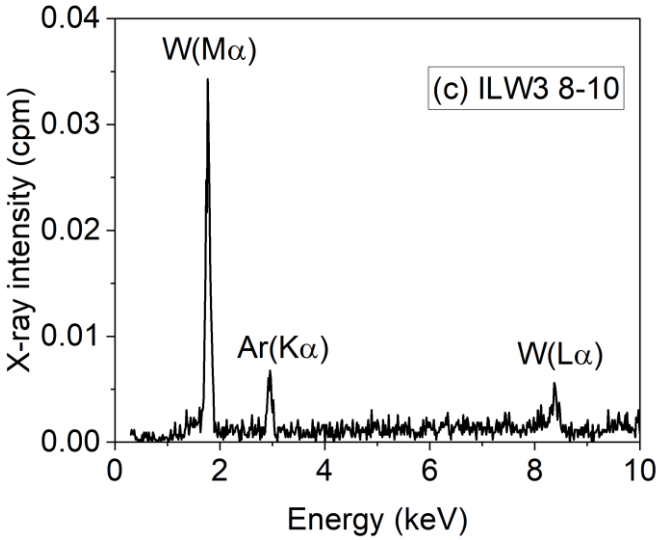


Fig. 5.4. Typical β-ray induced X-ray spectra obtained from(a) ILW3 1-10, (b) ILW3 4-10 and (c) ILW3 8-10.

Fig. 3.12, high energy W(Lα) X-rays are less attenuated by W than W(Mα) X-rays. Therefore, the intensity ratio of W(Lα) X-rays to W(Mα) X-rays increases with increasing penetration depth of W. The strong W(Lα) X-rays in the sample 8-10 compared to sample 4-10 indicated that T was located in the deeper region of the W bulk.

The integrated BIXS X-ray intensity from 0 to 15 keV of W-CFC divertor tiles is plotted in Fig. 5.5 (a). In both ILW campaigns, spectra obtained from inboard tiles had higher X-ray intensity than that

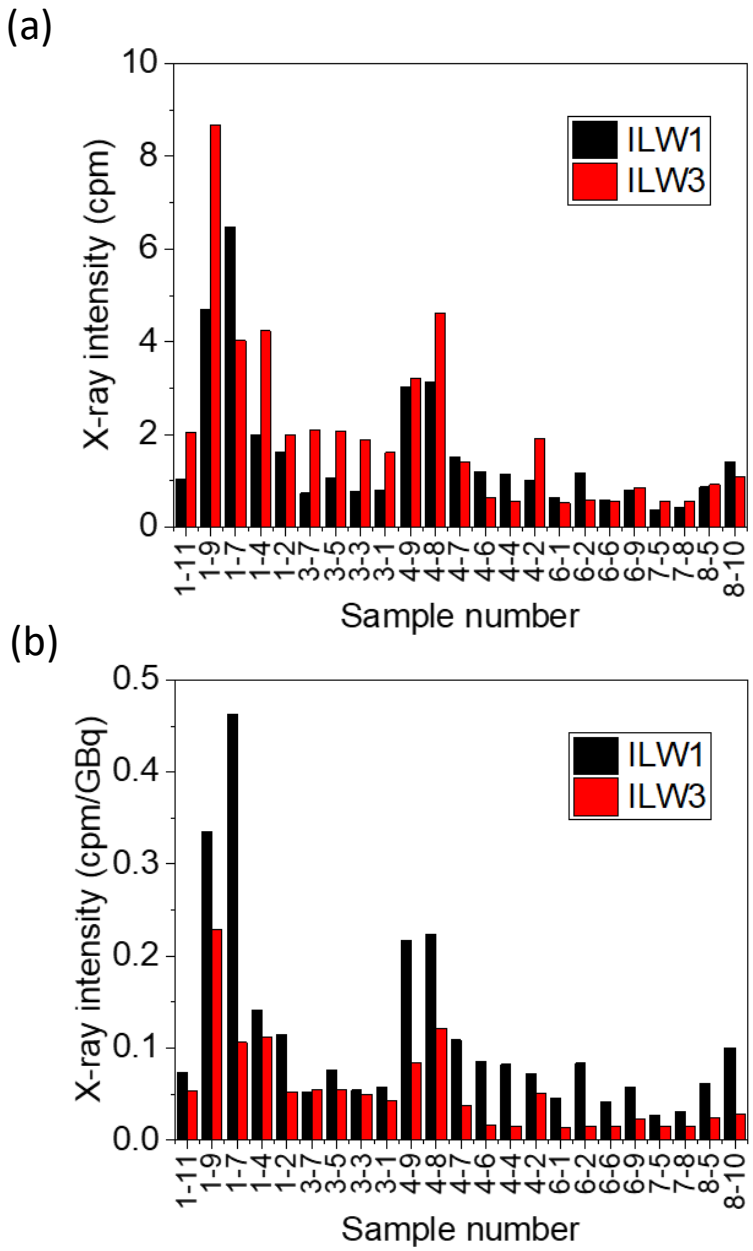


Fig. 5.5. (a) Integrated X-ray intensity of W-CFC divertor samples and (b) X-ray intensity normalized by total amount of produced T.

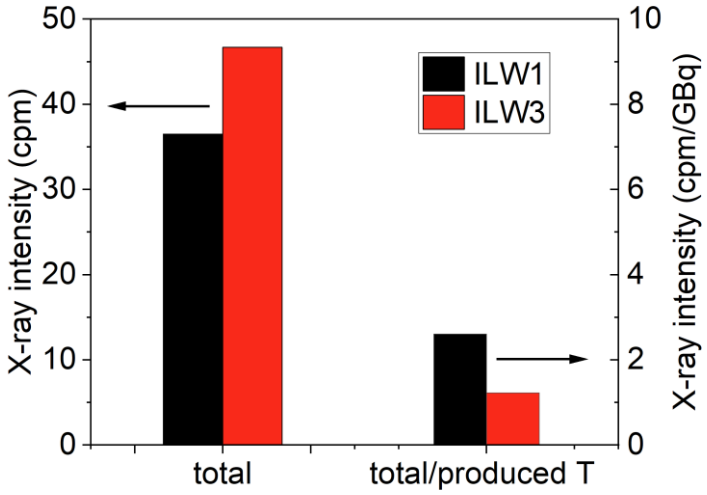


Fig. 5.6. (a) Total BIXS X-ray intensity of W-CFC divertor tiles and (b) X-ray intensity normalized by total amount of produced T.

from outboard tiles. Also, X-ray intensity of ILW3 tiles was higher than that of ILW1 tiles. These observations of BIXS agreed to the IP results given in Figs. 5.1 and 5.2.

X-ray intensity of the samples was normalized by the amount of T produced during each campaign and shown in Fig. 5.5 (b). The normalized intensity was higher in ILW1 than ILW3 and it suggested lower accumulation rate of T in ILW3. The decrease in accumulation rate of D from ILW1 to ILW3 was also observed by ion beam analysis [2].

Fig. 5.6 presented total X-ray intensity of all samples for each campaign. The samples from ILW3 demonstrated higher X-rays than ILW1 samples because larger amount of T was produced during ILW3. The total X-rays were also divided by the T amount of each campaign. The reduction of T retention rate in ILW3 was confirmed, as shown in Fig. 5.5 (b).

Intensity ratio of Ar(Kα) X-rays to W(Lα) X-rays ($I_{Ar(K\alpha)}/I_{W(L\alpha)}$) was evaluated to determine T retention depth and summarized in Fig. 5.7. As discussed above, the contribution of high energy X-rays increases in accordance with increase of T retention depth. Therefore, small $I_{Ar(K\alpha)}/I_{W(L\alpha)}$ is indicating existence of T in the deeper region of the sample. $I_{Ar(K\alpha)}/I_{W(L\alpha)}$ is higher in inner divertor tiles than outer divertor tiles. The significantly large value was acquired in the shadowed region of Tile 4, the sample 4-10. In the case of outer divertor Tile 7 and 8 where the PFSs were eroded, $I_{Ar(K\alpha)}/I_{W(L\alpha)}$ was calculated to be in the range of 2 – 3.

To quantitatively calculate T retention depth from BIXS spectra, Monte Carlo simulations were performed with Geant4. Fig. 5.8 (a) shows the several examples of different T depth profiles

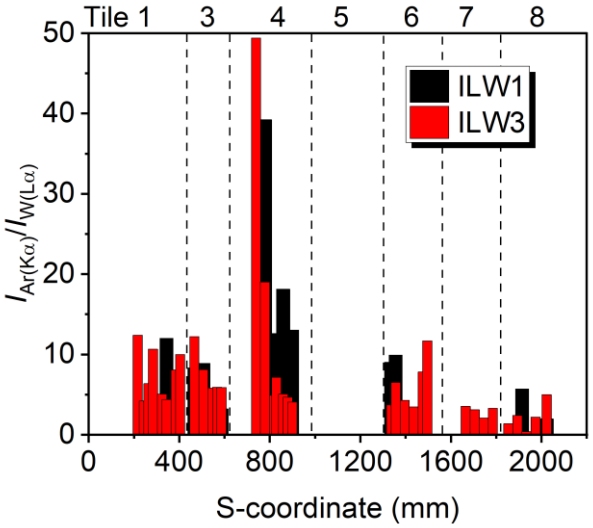


Fig. 5.7. X-ray intensity ratio of Ar(Kα) X-rays to W(Lα) X-rays.

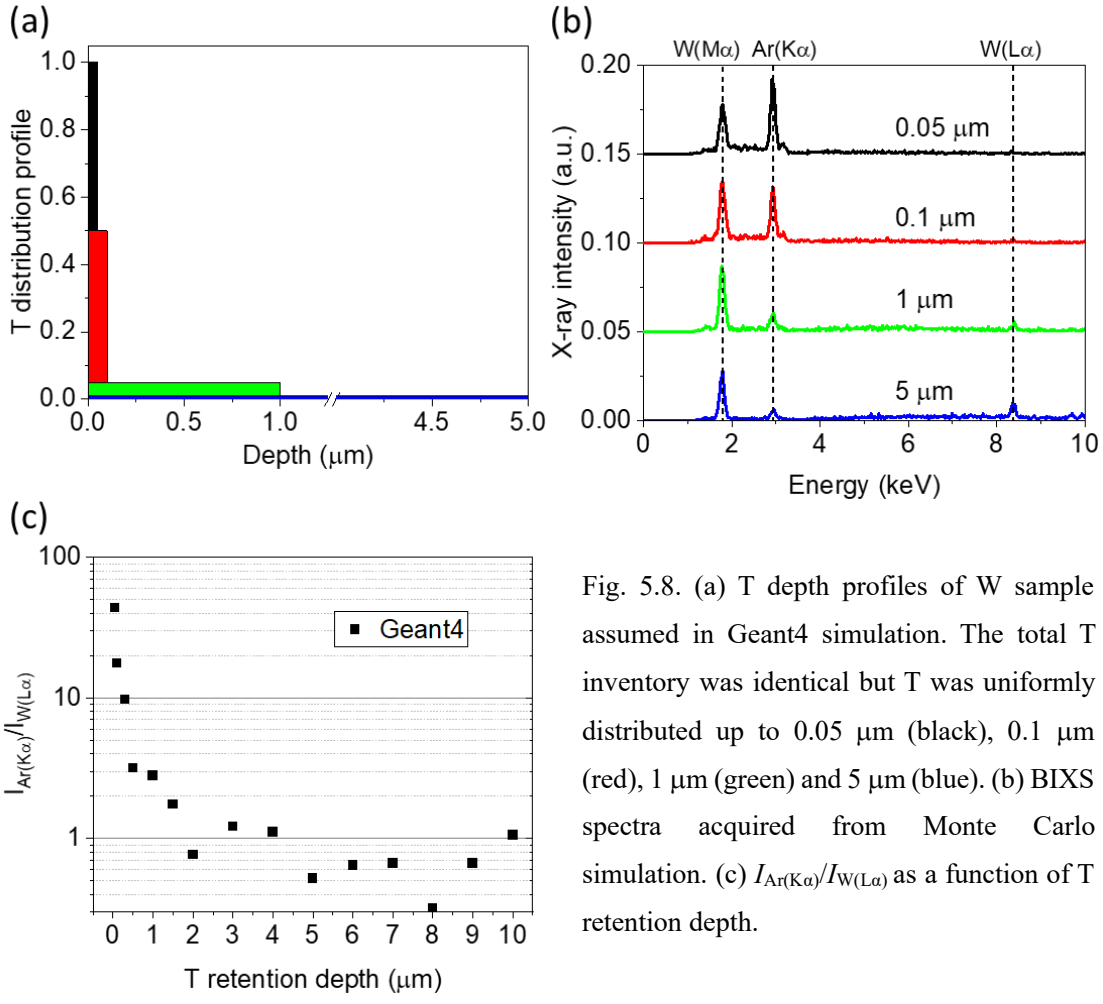


Fig. 5.8. (a) T depth profiles of W sample assumed in Geant4 simulation. The total T inventory was identical but T was uniformly distributed up to 0.05 μm (black), 0.1 μm (red), 1 μm (green) and 5 μm (blue). (b) BIXS spectra acquired from Monte Carlo simulation. (c) $I_{Ar(K\alpha)}/I_{W(L\alpha)}$ as a function of T retention depth.

constructed in Geant4 system. The total T inventory was identical, and T was uniformly distributed up to 0.05 μm (black), 0.1 μm (red), 1 μm (green) and 5 μm (blue). Fig. 5.8 (b) gives the BIXS spectra acquired from Monte Carlo simulation. This figure shows that the intensity of W(Lα) X-rays increased and that of Ar(Kα) X-rays decreased as T retention depth increased. $I_{Ar(K\alpha)}/I_{W(L\alpha)}$ values were plotted in Fig. 5.8 (c) as a function of T retention depth. $I_{Ar(K\alpha)}/I_{W(L\alpha)}$ decreased until T retention depth reached 2 ~ 3 μm. Beyond this depth, the value was almost constant. As mentioned above, $I_{Ar(K\alpha)}/I_{W(L\alpha)}$ of Tile 7 and 8 were in the range of 2 – 3 and these values corresponds to the penetration depth of ~ 1 μm in W.

The BIXS spectrum of 1-10 in Fig. 5.4 (a) was investigated with Geant4 to evaluate T depth profile. The thickness of deposition in PFS of W-CFC tiles was evaluated with surface profiling [13] and the thickness was 10-15 ± 5 μm at the apron of Tile 1 [3, 11]. Therefore, W sample with 5 μm-thick T-containing Be deposition layer was constructed in Geant4 system. X-ray spectrum obtained from

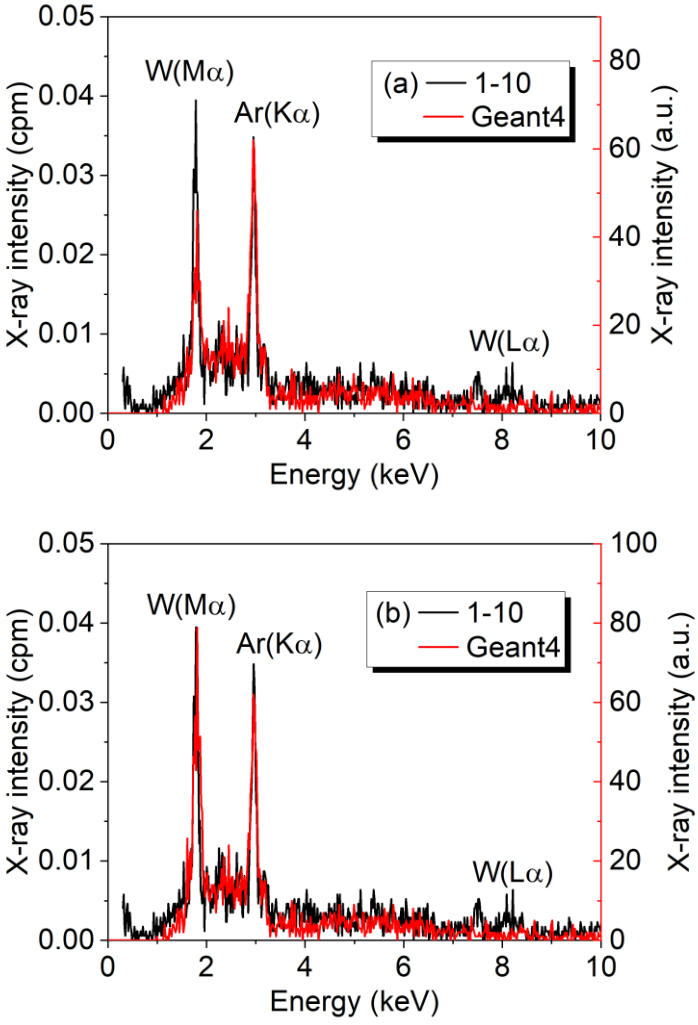


Fig. 5.9. (a) Comparison of BIXS spectrum obtained from ILW3 W-CFC 1-10 (black) and Geant4 BIXS spectrum (red). In Geant4 system, 5 μm-thick T-containing Be deposition layer was formed on the W sample. The intensity of W(Mα) peak acquired in (a) was modified according to overestimation of X-ray attenuation in Geant4 and shown in (b).

Geant4 was compared to the experimental BIXS spectrum in Fig. 5.9 (a). The simulation spectrum showed good agreement to the measured X-ray spectrum in the range above 2 keV. This agreement confirmed that T was co-deposited on the PFS of 1-10 with Be and the thickness of the deposition layer was several μm.

The intensity of W(Mα) X-rays in Fig. 5.9 (a) is weaker in Geant4 spectrum than experimental X-ray spectrum. Therefore, the W(Mα) X-ray is modified and plotted in Fig. 5.9 (b) according to previous study [14] which investigated correlation between experimental BIXS spectrum and X-ray spectrum calculated from Geant4. The attenuation of X-rays with the energy lower than 2 keV was overestimated in Geant4 [14]. Intensity of W(Mα) X-rays was attenuated to 30 % of its original intensity by the materials consisting BIXS measurement environment constructed in Geant4 system [14]. While the extent of attenuation evaluated from mass attenuation coefficient from NIST [15] was 50 % [14]. Therefore, the intensity of W(Mα) peak acquired from Geant4 was modified by considering the difference of X-ray attenuation between Geant4 and theoretical result. In Fig. 5.9 (b), two X-ray spectra showed better agreement after the adjustment.

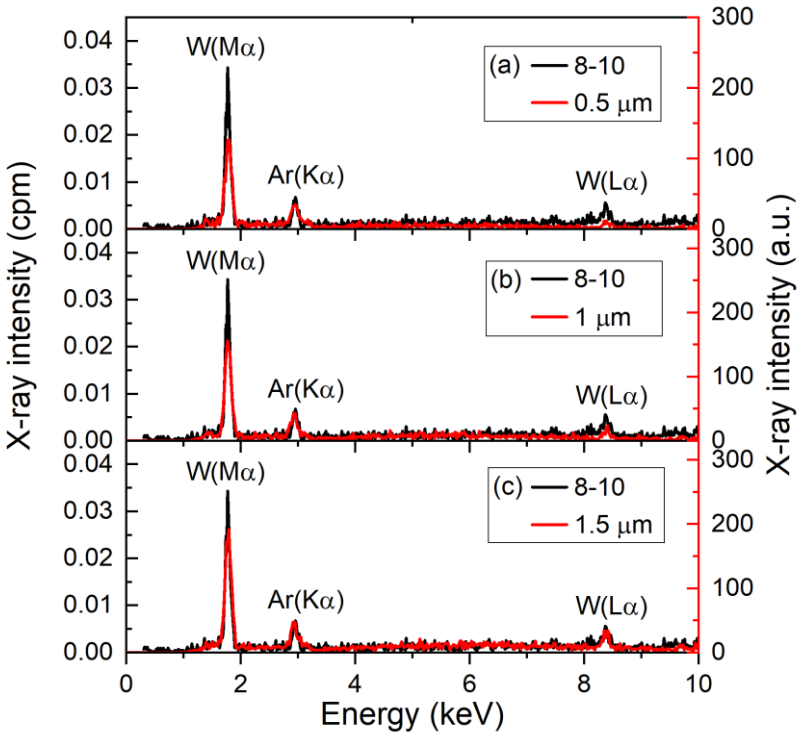


Fig. 5.10. Comparison of BIXS spectrum obtained from ILW3 W-CFC 8-10 (black) and Geant4 BIXS spectrum (red). In simulation system, T was uniformly distributed from surface up to (a) 0.5 μm, (b) 1 μm and (c) 1.5 μm.

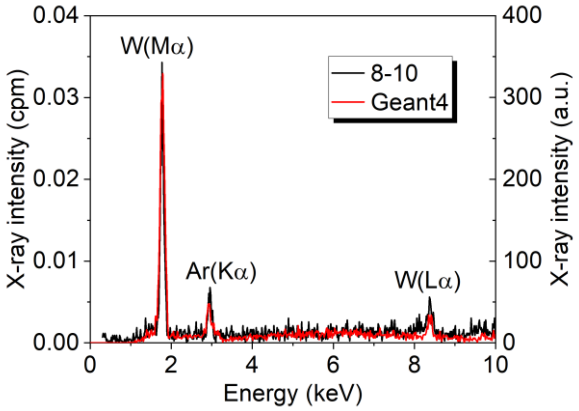


Fig. 5.11. The spectrum calculated from Geant4 plotted in Fig. 5.10 (c) was modified by considering overestimation of X-ray attenuation in Geant4, and compared with BIXS spectrum obtained from ILW3 W-CFC 8-10.

The BIXS spectrum from ILW3 8-10 sample in Fig. 5.4 (c) was also analyzed with Monte Carlo simulation and the results are shown in Fig. 5.10. The pure W block was constructed in Geant4 system because Tile 8 was net eroded. T was uniformly distributed from surface to (a) 0.5 μm, (b) 1 μm and (c) 1.5 μm depth. The simulation spectra acquired under assumption of 1.5 μm T retention depth was agreed to the BIXS spectrum of sample 8-10. The spectrum plotted in Fig. 5.10 (c) was also modified with the same manner explained in Fig. 5.9 and shown in Fig. 5.11. The better agreement between experimental spectrum and simulation spectrum was demonstrated in Fig. 5.11.

## 5.2. Bulk tungsten lamellae tiles

Figs. 5.12 and 5.13 are photos and IP images of samples cut from bulk W lamellae divertor Tile 5 used in ILW1 and ILW3, respectively. T enriched regions are shown in red and the regions with comparatively low T concentration are shown in blue in the IP image. The black dot indicated with a red circle in Fig. 5.12 is an artificial C dot put on the samples as position marker.

Fig. 5.14 shows the PSL intensity acquired from the PFSs of samples. The PSL intensity of each sample was normalized with the PSL intensity of standard sample piece which is labelled with largest amount of T. The PFSs of Tile 5 showed lower PSL intensity than W-CFC tiles (Fig. 5.1). The bulk W of Tile 5 contains less lattice defects than W coating which behave as traps of fuel [16]. Therefore, T

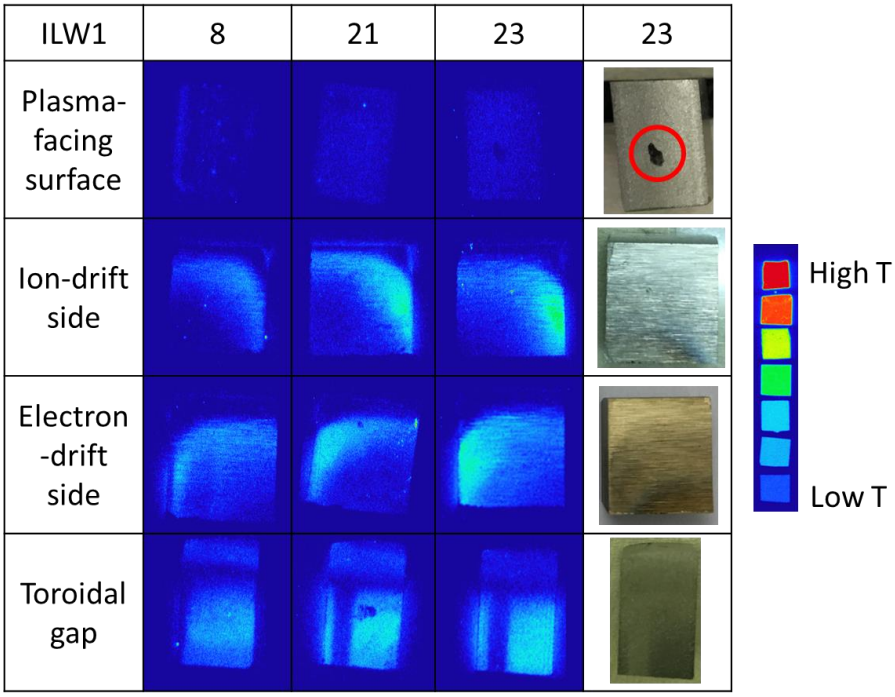


Fig. 5.12. Photos and IP images of samples cut from bulk W divertor Tile 5 used in ILW1.

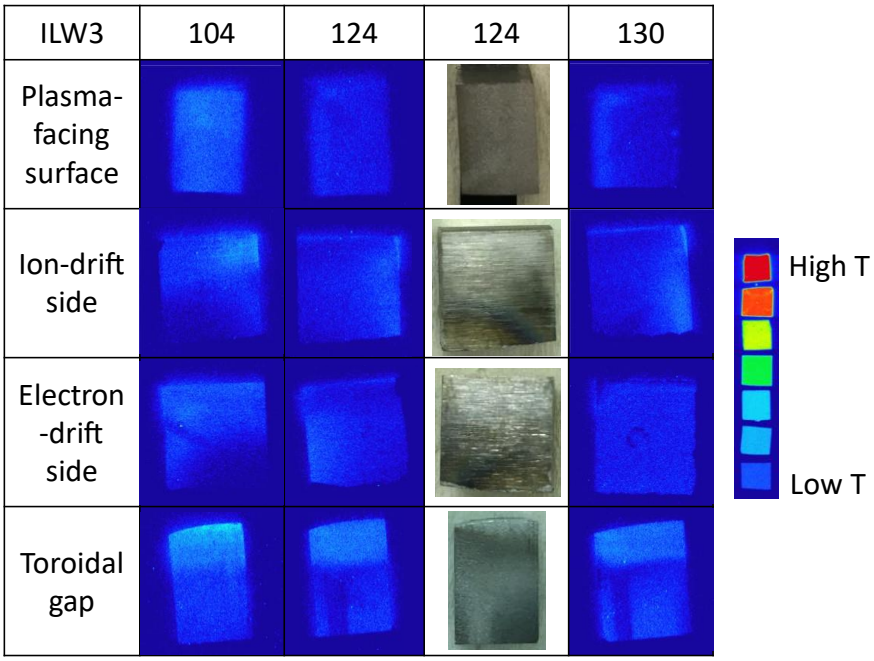


Fig. 5.13. Photos and IP images of samples cut from bulk W divertor Tile 5 used in ILW3.

concentration of bulk Tile 5 was lower than W-CFC tiles.

Figs. 5.12, 5.13 and 5.14 indicate that T concentration of PFS of ILW3 samples was higher than that of ILW1 samples. The significantly lower T concentrations of ILW1 samples than ILW3 samples were a consequence of plasma strike points which were dominantly distributed on PFS of Tile 5 during ILW1. In [17], the temperature of JET-ILW lamella was mapped with Finite Element Method. The temperature of the PFS increased up to 2000 °C [17] when the strike point was located at Tile 5. Releasing rate of D from the JET-ILW divertor was measured with TDS and D desorption rate was different according to the position of the divertor tile samples [12, 18, 19]. However, the releasing rate reached the maximum at temperature higher than 500 °C in most cases. The PFS of Tile 5 was more frequently heated to high temperature during ILW1 than ILW3 because the strike point was dominantly located on Tile 5 during ILW1. Higher PFS temperature of ILW1 tiles resulted in more active release of D from the tile surface.

As shown in sample photos given in Figs. 5.12 and 5.13, black deposition layer was observed on the gap surfaces. In ILW1 samples, T was enriched in the deposition layers mainly formed at the bottom of the gap surfaces. The elemental mapping performed for the toroidal gap surface of ILW1 specimen 21 with electron probe micro-analyzer (EPMA) showed that the area enriched with T corresponded to the region covered by the deposition layer composed of Be, O and small amount of C [20]. On the other hand, the PSL intensity in the regions near the PFSs were comparable to the

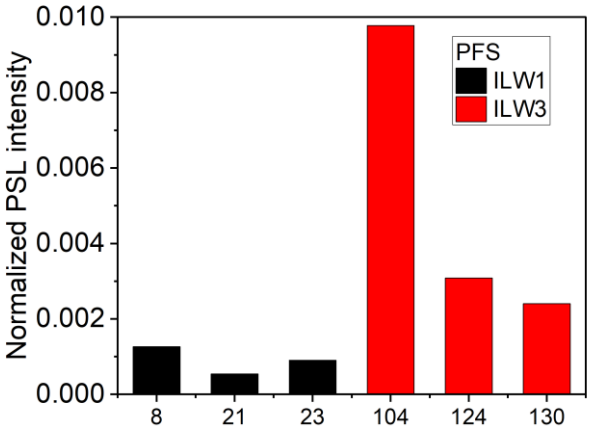


Fig. 5.14. PSL intensity of samples acquired from PFS of W lamellae tiles. The PSL intensity of the samples were normalized by the PSL intensity of standard sample which is labelled with largest amount of T.

background level in the case of ILW1 samples. The temperature of regions near the PFSs was higher than that in the bottom region [17]. Therefore, T accumulated near the PFS was desorbed from the tiles during operation. The T distribution was more uniform on the ILW3 sample surfaces than ILW1 samples probably due to smaller influence of strike point.

The PSL intensity of the gap surfaces is plotted In Fig. 5.15. The PSL intensity of the samples was normalized with the same manner described as the case of Fig. 5.14. T concentration of ILW3 lamellae was lower than that of ILW1 lamellae. The concentration of C impurities in the plasma reduced from campaign to campaign. The high C concentration in ILW1 induced enrichment of T in the deposition layers while the influence of C almost diminished in ILW3.

The deposition layer formed on the gap surfaces of W lamellae samples was analyzed with XPS and the deposit was sputtered by $Ar^+$ ions for depth profiling [21]. Fig. 5.16 is the IP images after sputtering of (a) electron-drift side of sample 8, (b) toroidal gap of sample 21 and (c) electron drift side of sample 23. The PSL intensity clearly decreased by sputtering due to removal of the deposition layer. Figs. 5.16 (a) and (c) showed decrease of PSL signal to the background level by sputtering in

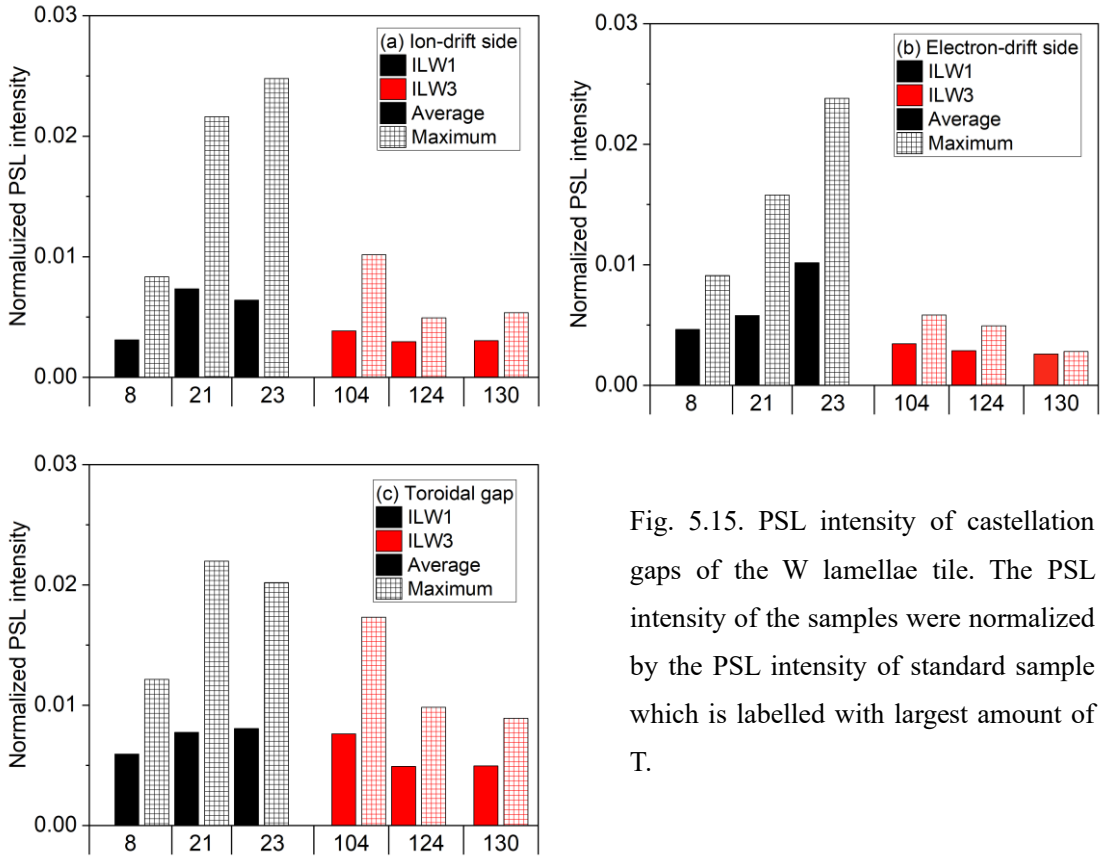


Fig. 5.15. PSL intensity of castellation gaps of the W lamellae tile. The PSL intensity of the samples were normalized by the PSL intensity of standard sample which is labelled with largest amount of T.

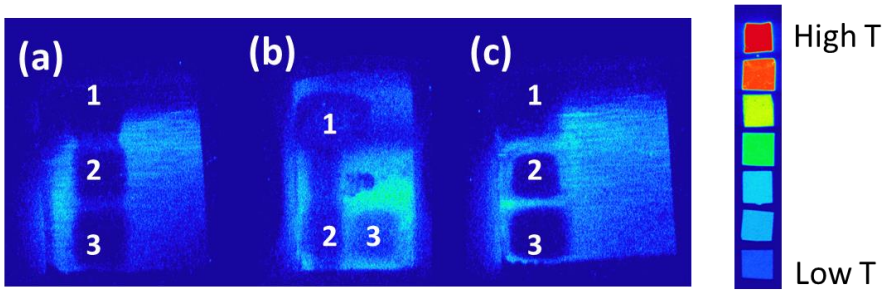


Fig. 5.16. IP image of W lamella samples after $Ar^+$ ion sputtering for depth profiling with XPS [21]. The sputtering was performed for (a) electron-drift side of sample 8, (b) toroidal gap of sample 21 and electron drift side of sample 23.

the cases of sample 8 and 23. These observations indicated that T was removed almost completely by sputtering together with deposition layer formed on the tile surface. The PSL intensity of the sputtered region of sample 21 was clearly higher than the background level. The PSL intensity ratios of before to after sputtering are shown in Fig. 5.17. The PSL intensity after sputtering was less than 5 % of that before sputtering in the cases of sample 8 and 23. However, in the case of sample 21, the PSL intensity after sputtering was 20 – 50 % of that before sputtering. This difference suggests that the deposition layer formed on the toroidal gap of sample 21 was thicker than that on electric-drift side of samples 8 and 23. According to Tokitani et al., the thickness of deposition layer formed on the toroidal gap of sample 21 was larger than 300 nm [20].

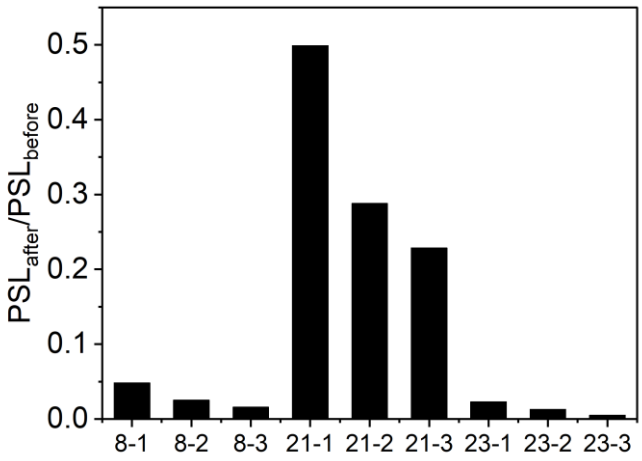


Fig. 5.17. PSL intensity ratio of after to before sputtering of W lamellae gap surfaces. The position 1, 2 and 3 accorded to location 1, 2 and 3 in Fig. 5.16.

## 5.3. Summary

The retention mechanisms of T in the divertor region were investigated in Chapter 5. T was co-deposited on the PFS of inner W-CFC divertor tiles with Be, O and C. The T concentration was highest in the Tile 1 where the thickest deposition layers were formed. The C concentration of co-deposition layers influenced T concentration. The sample taken from Tile 4 at the position close to the divertor remote area showed very high T concentration in the deposition layer as a consequence of high C concentration. Also, the T accumulation rate decreased in ILW3 due to reduction of C impurities inside the tokamak. On the other hand, the implantation of the high energy T ions was the main T retention mechanism in the case of the outer W-CFC divertor tiles having eroded surfaces.

The implantation of high energy tritons was ascertained in the PFSs of bulk W lamellae tiles. T concentration in the PFSs of W lamellae tiles was small especially for the tiles used in ILW1. It was ascribed to the plasma strike points which were dominantly distributed on the PFSs of bulk W tiles during ILW1 and induced thermal desorption of T. The T-containing deposition layer was formed on the gap surfaces of W lamellae tiles. The deposition layers were consisted of Be, O and small amount of C. The concentration of T in the gap surfaces of the lamellae tiles was also increased with increasing C content.

References


[1] M. Mayer et al., Erosion and deposition in the JET divertor during the second ITER-like wall campaign, Phys. Scr. T170 (2017) 014058, https://doi.org/10.1088/1402-4896/aa8ff9S

[2] S. Krat et al., Comparison of erosion and deposition in JET divertor during the first three ITER-like wall campaigns, Phys. Scr. T171 (2020) 014059, https://doi.org/10.1088/1402-4896/ab5c11

[3] K. Heinola et al., Experience on divertor fuel retention after two ITER-Like Wall campaigns, Phys. Scr. T170 (2017) 014063, https://doi.org/10.1088/1402-4896/aa9283

[4] M. Mayer et al., Erosion and deposition in the JET divertor during the first ILW campaign, Phys. Scr. T167 (2016) 014051, https://doi.org/10.1088/0031-8949/T167/1/014051

[5] C. Ruset et al., Deuterium and beryllium depth profiles into the W-coated JET divertor tiles after ITER-like wall campaigns, Nucl. Mater. Energy 30 (2022) 101151, https://doi.org/10.1016/j.nme.2022.101151

[6] A. Lahtinen et al., Deuterium retention on the tungsten-coated divertor tiles of JET ITER-like wall in 2015-2016 campaign, Fusion Eng. Des. 146 (2019) 1979-1982, https://doi.org/10.1016/j.fusengdes.2019.03.081

[7] Y. Hatano et al., Tritium distributions on W-coated divertor tiles used in the third JET ITER-like wall campaign, Nucl. Mater. Energy 18 (2019) 258-261, https://doi.org/10.1016/j.nme.2019.01.001

[8] Y. Hatano et al., 2D tritium distribution on tungsten tiles used in JET ITER-like wall project, J. Nucl. Mater. 463 (2015) 966-969, https://doi.org/10.1016/j.jnucmat.2014.12.041

[9] Y. Hatano et al., Tritium distributions on tungsten and carbon tiles used in the JET divertor, Phys. Scr. T167 (2016) 014009, https://doi.org/10.1088/0031-8949/T167/1/014009

[10] S. E. Lee et al., Global distribution of tritium in JET with the ITER-like wall, Nuclear Materials and Energy 26 (2021) 100930, https://doi.org/10.1016/j.nme.2021.100930

[11] A. Widdowson et al., Material migration patterns and overview of first surface analysis of the JET ITER-like wall, Phys. Scr. T159 (2014) 014010, https://doi.org/10.1088/0031-8949/2014/T159/014010

[12] Y. Oya et al., Comparison of hydrogen isotope retention in divertor tiles of JET with the ITER-like wall following campaigns in 2011-2012 and 2015-2016, Fusion Sci. Technol. 76 (2020) 439-445, https://doi.org/10.1080/15361055.2020.1716455

[13] K. Heinola et al., Tile profiling analysis of samples from the JET ITER-like wall and carbon wall, Phys. Scr. T159 (2014) 014013, https://doi.org/10.1088/0031-8949/2014/T159/014013

[14] S. E. Lee et al., Influence of internal structure of semiconductor detector on X-ray induced by tritium beta rays, Fusion. Sci. Tech. 76 (2020) 327-332,

https://doi.org/10.1080/15361055.2020.1711855

[15] J. H. Hubbell and S. M. Seltzer, NIST Standard Reference Database 126, https://www.nist.gov/pml/x-ray-mass-attenuation-coefficients

[16] J. P. Coad et al., Erosion/deposition issues at JET, J. Nucl. Mater. 290-293 (2001) 224-230, https://doi.org/10.1016/S0022-3115(00)00479-7

[17] R. A. Pitts et al., Physics conclusions in support of ITER W divertor monoblock shaping, Nucl. Mater. Energy 12 (2017) 60-74, https://doi.org/10.1016/j.nme.2017.03.005

[18] J. Likonen et al., Investigation of deuterium trapping and release in the JET ITER-like wall divertor using TDS and TMAP, Nucl. Mater. Energy 19 (2019) 166-178, https://doi.org/10.1016/j.nme.2019.02.031

[19] J. Likonen et al., Investigation of deuterium trapping and release in the JET divertor during the third ILW campaign using TDS, Nucl. Mater. Energy 19 (2019) 200-206, https://doi.org/10.1016/j.nme.2019.03.01218

[20] M. Tokitani et al., Surface morphology of the bulk tungsten divertor tiles from JET ITER-like wall, Phys. Scr. T171 (2020) 014010, https://doi.org/10.1088/1402-4896/ab3d09

[21] Y. Oya, private communication

# Chapter 6. Tritium behaviour in fusion device with Be/W walls

## 6.1. Summary of tritium distributions in JET with ITER-like wall after deuterium discharges

Under DD reaction, T is produced and it migrates inside the tokamak. The initial kinetic energy of T produced by DD reaction is 1.01 MeV and far larger than that of D in the plasma. The high energy T ions were 1) directly implanted to PFCs via prompt loss or 2) confined by the magnetic fields and thermalized. The thermalized T ions were transferred along the magnetic field together with D ions and co-deposited on the surfaces of PFCs with Be sputtered by PWIs and O, C and other impurities in the plasma. Based on the observations in the previous chapter, Fig. 6.1 summarizes the distribution of T inside the JET-ILW tokamak formed as results of implantation of high energy T ions and co-deposition of thermalized T.

The main chamber limiter tiles showed different T retention mechanisms between PFSs and surfaces inside the castellation gaps. The implantation of high energy T ions was the dominant T retention

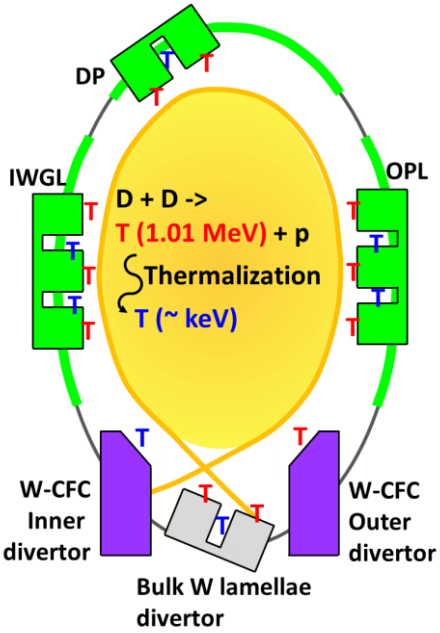


Fig. 6.1. Distribution of T in the JET-ILW tokamak formed as results of implantation of high energy T ions (red) and co-deposition with D, Be and other impurities after thermalization in the plasma (blue).

mechanism in PFSs. The retention depth was ~ 6 μm. The T content was largest in OPL and T concentration of IWGL and DP was lower than that of OPL by an order of magnitude. The co-deposition of thermalized T with wall materials on the PFS of Be limiter tiles was also determined by BIXS X-ray spectrum, especially on the both edges of Be limiter tiles. However, the amount of implanted T was far larger than that of co-deposited T in PFSs of Be limiter tiles.

The thermalized T was co-deposited on the castellation sides of limiter tiles with D, Be, O, C and other metal impurities. The small amount of metal impurities such as W, Ni, Al and Cu were detected in the deposition layers formed near the groove entrances (up to depths < 0.5 mm) but the deposition layers were dominantly composed of Be oxides containing D. The castellation sides of IWGL and OPL showed similar T profiles regardless of the limiter positions after each campaign. The T retention was large near the entrance of grooves (up to depth of ~ 1.5 mm) and decreased with increasing depth in the deeper regions. The castellation sides of DP showed more uniform T profiles. The T retention in the deeper regions (depths > 1.5 mm) was higher after ILW1 than ILW3 because of higher C content in the deposition layers.

Tritium thermalized in the plasma can also be transported to the divertor region along magnetic field and accumulated on the PFSs of W-CFC inner divertor tiles by co-deposition with eroded materials and impurities. T concentration was highest in the inner divertor Tile 1 of which deposition thickness was 10 – 15 μm [1, 2]. On the other hand, T was implanted to net-eroded W-CFC outer divertor tiles and the implantation depth of T was ~ 1.5 μm. The W-CFC inner divertor tiles showed higher T retention than the outer divertor tiles because the thick deposition layers were formed on the W-CFC inner divertor tiles.

T was implanted to PFSs of bulk W lamellae Tile 5. The T concentration of PFS of Tile 5 was lower than that of W-CFC tiles probably because the number of defects trapping hydrogen isotopes was smaller in bulk W than W-coating. Unlike PFSs of W lamellae tiles, T-containing deposition layers were found on the gap surfaces.

The concentration of implanted T was sensitively depended on the tile location in the main chamber and determined by the balance between the rates of T implantation and removal by thermal desorption and/or tile erosion. The amount of T remained after desorption and erosion was largest in PFS of OPL because of (i) slow desorption of T and (ii) less erosion of PFSs. Also, PFSs of W lamellae tiles retrieved after ILW1 contained smaller amount of T than that used in ILW3 because the strike points were dominantly located on Tile 5 during ILW1 and it induced thermal desorption of T from the surface.

On the other hand, the T content in the deposition layer was irrelevant to the location where deposition layer was formed but it increased with increasing C concentration. The T concentration and deposition rate were smaller in the ILW3 tiles than ILW1 tiles owing to reduction in C impurities from campaign to campaign.

## 6.2. Methods to reduce tritium inventory

The discharge time of JET-ILW was an order of several seconds, e.g. 20 s, per pulse [3], while that of ITER will be longer by an order of magnitude, e.g. 400 or 3600 s, per pulse [4]. The longer plasma discharge will generate thicker deposition layers. The Be first wall of ITER will be castellated like JET-ILW limiter tiles as well. On the other hand, ITER will use a monoblock divertor with fully castellated structure. As a result, the contribution of co-deposited T to total T inventory will be critical in the ITER. The suggestions to minimize fuel inventory in vacuum vessels of ITER and future fusion reactors are given as follows based on results obtained in this study.

Fig. 6.2 [5] is the design of the ITER divertor vertical target. The ITER divertor was designed to endure under 10 – 20 MW/m$^2$ heat flux [6]. The divertor target is composed of W monoblocks and CuCrZr cooling tubes are passing through the monoblocks to remove heat from the tiles. In the divertor, 320,000 W monoblocks are installed [7]. The nominal dimension of the monoblock is 28 × 28 × 12 mm$^3$ and the distance between PFS and cooling pipe is 6 mm [6]. The outer diameter of the cooling pipe is 17 mm [6]. The gap distance between monoblocks is ~ 0.5 mm [8]. According to given design of the ITER divertor target, PFS area of a single W monoblock is 12 × 28 mm$^2$. The area of a surface

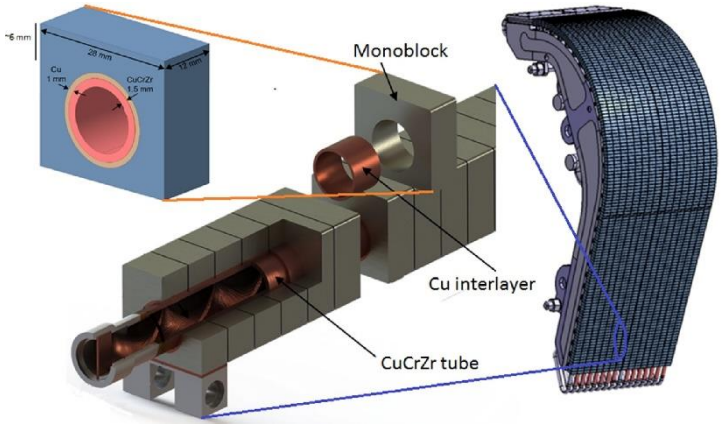


Fig. 6.2. Structure of ITER divertor vertical target with dimensions of W-monoblock [5].

in poloidal gap and toroidal gap is $12 \times 28$ mm$^2$, $28 \times 28 - \pi \times (17/2)^2$ mm$^2$, respectively. Therefore, the ratio of surfaces inside the gaps to the total area of the single W monoblock from ITER divertor is

$$\frac{\left[12 \times 28 + \left(28 \times 28 - \pi \times \frac{17^2}{2}\right)\right] \times 2}{12 \times 28 + \left[12 \times 28 + \left(28 \times 28 - \pi \times \frac{17^2}{2}\right)\right] \times 2} = 0.84 . \quad (6.1)$$

The total area of the surfaces inside the gaps is wider than that of PFS in the ITER divertor. Therefore, accumulation of T by co-deposition on the surfaces inside the tile gaps has to be seriously considered.

To reduce the amount of T-containing deposition layer formed on the gap surfaces, the gap width between monoblocks should be as narrow as possible. Rubel et al. [9] performed modelling to calculate Be deposition rate on the gap surfaces as a function of the width of the JET-ILW limiter castellation gaps. The amount of deposition produced on the gap surfaces increased proportional to the gap width [9]. Consequently, narrow gap width is preferable to reduce deposition rate on the surfaces inside the gaps.

Temperature distribution of the ITER W-monoblock at the end of thermal pulse was calculated and the temperature near the PFS was higher than 2000 °C [6]. As mentioned above, D release rate reached maximum in temperature higher than 500 °C [10 – 12]. The high tile temperature of ITER W-monoblock implies that T accumulated in the ITER divertor tiles can be desorbed from the tiles. In this study, the desorption of T from the tile surfaces during operation of JET was empirically validated in ILW1 W lamellae Tile 5 where the strike points were located. The desorption was observed not only in PFSs but in gap surfaces near PFSs. Therefore, T retained in the surfaces of ITER W-monoblock gaps will also be removed at positions where strike points will be located. In order to provoke desorption of T in a wide area of divertor targets, the strike points should be intentionally swept on PFS as wide as possible.

The QUEST tokamak in Kyusyu University started its first operation with full metal plasma-facing walls composed of W and stainless steel [13]. Fig. 6.3 is a picture of QUEST hot wall and deposition layers formed on the wall surface [13]. Even though QUEST started its first operation with metal walls and without C as a PFM, C was main constituent of the deposition layers [13] and it influenced on D retention in the reactors [14]. The observations indicate that C is ubiquitous impurity in vacuum devices and the influence of C on T retention is possible even in the full metal machines. The T concentration in the co-deposition layers formed during ILW3 was lower than that formed in ILW1, as mentioned in the previous chapters. This is because the C content in the plasma was highest during ILW1 due to C remained as a legacy of previous JET-C operation and it decreased as the campaign

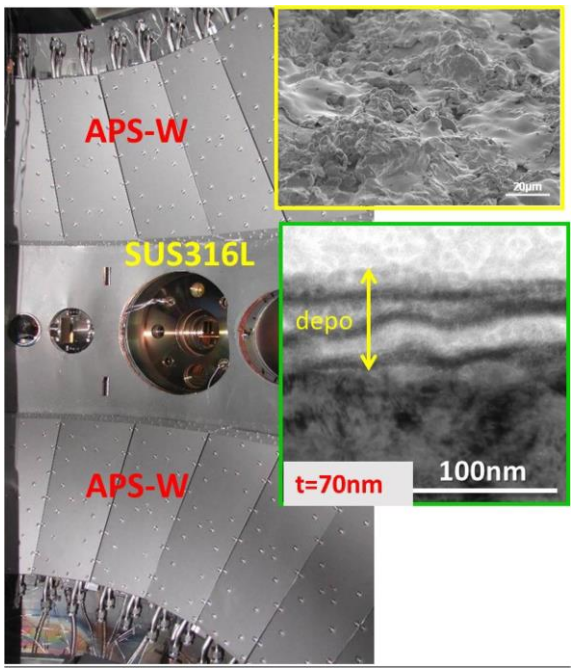


Fig. 6.3. A picture of QUEST hot wall and deposition layers formed on the wall. The picture is from [13].

progressed. From this perspective, C content in the plasma in future fusion reactors should be controlled strictly to alleviate formation of co-deposition layers with high T concentration.

References


[1] K. Heinola et al., Experience on divertor fuel retention after two ITER-Like Wall campaigns, Phys. Scr. T170 (2017) 014063, https://doi.org/10.1088/1402-4896/aa9283

[2] A. Widdowson et al., Material migration patterns and overview of first surface analysis of the JET ITER-like wall, Phys. Scr. T159 (2014) 014010, https://doi.org/10.1088/0031-8949/2014/T159/014010

[3] A. Widdowson et al., Evaluation of tritium retention in plasma facing components during JET tritium operations, Phys. Scr. 96 (2021) 124075, https://doi.org/10.1088/1402-4896/ac3b30

[4] D. Wunderlich et al., NNBI for ITER: status of long pulses in deuterium at the test facilities BATMAN Upgrade and ELISE, Nucl. Fusion 61 (2021) 096023, https://doi.org/10.1088/1741-4326/ac1758

[5] X. Bonnin et al., ITER divertor plasma response to time-dependent impurity injection, Nucl. Mater. Energy 12 (2017) 1100-1105, https://doi.org/10.1016/j.nme.2017.03.010

[6] T. Hirai et al., Use of tungsten material for the ITER divertor, Nucl. Mater. Energy 9 (2016) 612-622, https://doi.org/10.1016/j.nme.2016.07.003

[7] R. A. Pitts et al., Status and physics basis of the ITER divertor, Phys. Scr. T 138 (2009) 014001, https://doi.org/10.1088/0031-8949/2009/T138/014001

[8] J. P. Gunn et al., Surface heat loads on the ITER divertor vertical targets, Nucl. Fusion 57 (2017) 046025, https://doi.org/10.1088/1741-4326/aa5e2a

[9] M. Rubel et al., Fuel inventory and deposition in castellated structures in JET-ILW, Nucl. Fusion 57 (2017) 066027, https://doi.org/10.1088/1741-4326/aa6864

[10] J. Likonen et al., Investigation of deuterium trapping and release in the JET ITER-like wall divertor using TDS and TMAP, Nucl. Mater. Energy 19 (2019) 166-178, https://doi.org/10.1016/j.nme.2019.02.031

[11] J. Likonen et al., Investigation of deuterium trapping and release in the JET divertor during the third ILW campaign using TDS, Nucl. Mater. Energy 19 (2019) 200-206, https://doi.org/10.1016/j.nme.2019.03.012

[12] Y. Oya et al., Comparison of hydrogen isotope retention in divertor tiles of JET with the ITER-like wall following campaigns in 2011-2012 and 2015-2016, Fusion Sci. Technol. 76 (2020) 439-445, https://doi.org/10.1080/15361055.2020.1716455

[13] K. Hanada et al., Overview of recent progress on steady state operation of all-metal plasma facing wall device QUEST, Nucl. Mater. Energy 27 (2021) 101013, https://doi.org/10.1016/j.nme.2021.101013

[14] Y. Oya, et al., Effect of carbon impurity reduction on hydrogen isotope retention in QUEST

high temperature wall, Fusion Eng. Des., 146 (2019) 1480-1484, https://doi.org/10.1016/j.fusengdes.2019.02.110

# Chapter 7. Conclusions

The world largest existing fusion device JET was operated with ITER-like wall (ILW) to investigate plasma-wall interactions in the Be/W plasma-facing wall environment. The non-destructive tritium detection methods were developed by combining imaging plate (IP) technique, β-ray induced X-ray spectrometry (BIXS) and Monte Carlo simulation. The developed techniques were applied to examine the tritium behaviours and distributions in tiles used in JET-ILW.

The backgrounds of ITER construction and the JET-ILW experiment were summarized in Chapter 1 together with published results of deuterium retention analyses in JET-ILW. The importance of tritium assessment in JET-ILW was described.

Tritium emits low energy β-rays with very short escape depth in solids. On the other hands, X-rays with far larger escape depths are generated by electron excitations by β-rays in matters. The interactions of β-rays and generated X-rays with matters were explained in detail in Chapter 2.

The tiles used in JET-ILW and retrieved for tritium retention analyses were described in Chapter 3. Also, the principles of tritium detection methods applied in this study were presented in this chapter.

The tritium inventory in Be main chamber limiter tiles and retention mechanisms were summarized in Chapter 4. High energy tritium ions produced by deuterium-deuterium fusion reactions were implanted to plasma-facing surfaces (PFSs) of Be limiter tiles. The long-term tritium retention in Be limiter PFSs was determined by the balance between tritium accumulation by implantation and removal by thermal desorption and/or tile erosion. Therefore, tritium inventory in PFSs was dependent on the tile location. Part of high energy tritium ions was confined by magnetic fields and thermalized in the plasma. The thermalized tritium was co-deposited with beryllium sputtered in the main chamber, deuterium and other impurities on the surfaces inside the castellation grooves of Be limiter tiles. The carbon content in the deposition layers was a decisive factor in the tritium concentration in the depositions and the tritium concentration was high in the deposition layers with high carbon concentration.

Chapter 5 showed tritium distributions in JET-ILW divertor tiles. The thermalized tritium was co-deposited with D, Be, O and C on the PFSs of W-CFC inner divertor tiles. Tritium retention was large in the samples cut from tile where thick deposition layers were formed. Significantly high tritium concentration was observed in the deposition layers if carbon concentration in deposition layer was 30 – 50 %. The high energy tritium ions were implanted to PFSs of W-CFC outer divertor tiles and PFSs

of bulk W lamellae tiles. The tritium retention in the PFSs of W lamellae tiles used in ILW1 was small because of the tritium desorption induced by the plasma strike points dominantly located on bulk W tiles. The tritium-containing deposition layers were also formed on the surfaces inside the W lamellae gaps.

Chapter 6 summarized the tritium distributions in JET vacuum vessel with ILW and the underlying mechanisms. The proposals to minimize tritium accumulation in ITER and future fusion reactors were also given. ITER will be operated with longer discharge time than JET-ILW. Also, ITER divertor tiles will be the assembly of W-monoblocks. Therefore, co-deposition of tritium can be significant due to thicker deposition layers and wider areas inside the gaps. To reduce tritium concentration inside the ITER and future fusion reactors, (i) the gap between the monoblocks should be narrowed, (ii) the tile surfaces should be swept by plasma by changing plasma strike points to enhance thermal desorption of tritium in a wide area and (iii) the concentration of carbon impurities have to be minimized.

# List of publications


[1] Y. Hatano, S. E. Lee, J. Likonen, S. Koivuranta, M. Hara, S. Masuzaki, N. Asakura, K. Isobe, T. Hayashi, J. Ikonen, A. Widdowson, JET contributors, Tritium distributions on W-coated divertor tiles used in the third JET ITER-like wall campaign, *Nuclear Materials and Energy* 18 (2019) 258-261, https://doi.org/10.1016/j.nme.2019.01.001

[2] S. E. Lee, Y. Hatano, M. Hara, M. Matsuyama, Influence of Internal Structure of Semiconductor Detector on Spectrum of X-Rays Induced by Tritium Beta Rays, *Fusion Science and Technology*, 76 (2020) 327-332, https://doi.org/10.1080/15361055.2020.1711855

[3] S. E. Lee, Y. Hatano, M. Hara, S. Masuzaki, M. Tokitani, M. Oyaizu, H. Kurotaki, D. Hamaguchi, H. Nakamura, N. Asakura, Y. Oya, J. Likonen A. Widdowson, S. Jachmich, K. Helariutta, M. Rubel, JET Contributors, Tritium distribution analysis on Be limiter tiles from JET-ITER like wall campaigns using imaging plate technique and β-ray induced X-ray spectrometry, *Fusion Engineering and Design* 160 (2020) 111959, https://doi.org/10.1016/j.fusengdes.2020.111959

[4] S. E. Lee, Y. Hatano, M. Tokitani, S. Masuzaki, Y. Oya, T. Otsuka, N. Ashikawa, Y. Torikai, N. Asakura, H. Nakamura, K. Isobe, H. Kurotaki, D. Hamaguchi, T. Hayashi, A. Widdowson, S. Jachmich, J. Likonen, M. Rubel, JET contributors, Global distribution of tritium in JET with the ITER-like wall, *Nuclear Materials and Energy* 26 (2021) 100930, https://doi.org/10.1016/j.nme.2021.100930

[5] S. Lee, Y. Hatano, S. Masuzaki, Y. Oya, M. Tokitani, M. Yajima, T. Otsuka, N. Ashikawa, Y. Torikai, N. Asakura, H. Nakamura, H. Kurotaki, T. Hayashi, T. Nozawa, A. M. Ito, J. Likonen, A. Widdowson, M. Rubel and JET Contributors, Tritium distributions in castellated structures of Be limiter tiles from JET-ITER like wall experiments, *Nuclear Fusion* 63 (2023) 046023, https://doi.org/10.1088/1741-4326/acb9a5